WO_3-LOADED TIO_2 NANOTUBES VIA ELECTROCHEMICAL ANODIZATION TECHNIQUE FOR EFFICIENT PHOTOCATALYTIC REMOVAL OF MERCURY

LEE WAI HONG

DISSERTATION SUBMITTED IN FULFILMENT OF THE REQUIREMENTS FOR THE DEGREE OF MASTER OF PHILOSOPHY

INSTITUTE OF GRADUATE STUDIES
UNIVERSITY OF MALAYA
KUALA LUMPUR

2016

ABSTRACT

Mercury removal from both air emissions and industrial wastewater are key targets for the environmental sustainability strategy to ensure a healthy environment for future generation. The formation of self-organized titanium dioxide (TiO_2) nanotubes without bundling is essential for high efficiency in mercury removal. Thus, this research aims to study on the development of an efficient WO_3-loaded TiO_2 nanotubes catalyst for the removal of mercury ions. WO_3-loaded TiO_2 nanotubes were synthesized through single step electrochemical anodization technique by using tungsten as the cathodic material instead of the conventionally used platinum electrode. As compared with platinum, tungsten (W) metal has lower chemical stability, forming dissolved ions (W^{6+}) in the electrolyte. The W^{6+} ions then moved towards the titanium foil and formed a coherent deposit on titanium foil. In fact, coupling TiO_2 with W^{6+} species will lead to an additional electronic state in the band-gap, which in turn affect a change in the electronic and functionality of TiO_2 itself. Comprehensive investigations on different parameters, such as composition of electrolyte, anodization time, and anodization voltage were conducted in order to control the specific architecture of nanotubes. Highly ordered WO_3-loaded TiO_2 nanotube films (0.22 to 3.29 at% of W) were successfully synthesized through anodization of titanium (Ti) foil in ethylene glycol containing ammonium fluoride (NH_4F). It was found that this resultant WO_3-loaded TiO_2 nanotubes demonstrated a maximum mercury removal rate of 91% in 120 minutes. This performance was approximately 1.4 times higher than the pure TiO_2 nanotubes. The presence of W element in TiO_2 showed an improvement of mercury removal efficiency because it acted as an effective mediator to trap the photo-induced electrons and minimize the recombination of charge carriers.

ABSTRAK

Penyingkiran merkuri daripada pelepasan udara dan air sisa industri adalah sasaran utama strategi kemampanan alam sekitar bagi menjamin alam sektar yang sihat untuk generasi seterusnya. Pembentukan TiO_2 tiubnano yang bebas daripada kelompok adalah penting untuk penyingkiran merkuri berkecekapan tinggi. Oleh itu, kajian ini bertujuan untuk mengkaji tiub nano WO_3-TiO_2 yang berkecekapan tinggi untuk penyingkiran ion merkuri. Struktur nano WO_3-TiO_2 akan disintesis melalui langkah tunggal teknik penganodan elektrokimia dengan menggunakan tungsten sebagai katod untuk menggantikan elektrod platinum yang biasa digunakan. Sekiranya dibandingkan dengan platinum, logam tungsten (W) mempunyai kestabilan kimia yang lebih rendah dan akan membentuk ion (W^{6+}) yang larut dalam elektrolit. Ion W^{6+} kemudiannya bergerak ke arah kepingan titanium dan mambentuk deposit koheren pada kepingan titanium tersebut. Gandingan TiO_2 dengan spesis W^{6+} akan membentuk keadaan elektronik tambahan di jurang jalur, dan seterusnya akan mempengaruhi suatu perubahan pada elektronik dan fungsi TiO_2. Kajian komprehensif pada parameter berlainan seperti komposisi elektrolit, masa penganodan, dan keupayaan elektrik telah dilakukan untuk mengawal susunan dan geometri tiub nano. Filem struktur nano WO_3–TiO_2 yang tersusun (0.22 to 3.29 at% W) telah berjaya disintesis melalui penganodan foil Ti dalam glikol etilena yang mengandungi NH_4F. Sehubungan dengan itu, didapati bahawa kadar penyingkiran merkuri maksimum oleh struktur nano WO_3-TiO_2 adalah sebanyak 91% dalam masa 120 minit. Peningkatan prestasi sebanyak 1.4 kali ganda telah dicatatkan berbanding dengan TiO_2 tiub nano yang asal. Kehadiran unsur W dalam TiO_2 menunjukkan peningkatan kecekapan penyingkiran merkuri kerana ia akan bertindak sebagai pengantara yang berkesan untuk memerangkap elektron dan mengurangkan pengabungan pembawa cas.

ACKNOWLEDGEMENTS

I would like to thank University of Malaya (UM) and Nanotechnology and Catalysis Research Centre (NANOCAT) for giving me the opportunity to complete my research project under a conductive research environment with sufficient facilities.

I would also like to express my sincerest gratitude towards my supervisors, Dr. Lai Chin Wei and Prof Sharifah Bee Abd Hamid for their continuous support and guidance throughout my research project. Their suggestions and assistance were instrumental to the progress of my research and this thesis would not have been completed without their guidance.

Besides that, I would also like to express my gratitude to all the academic and technical staffs of NANOCAT for their advice and assistance. Also, a special thanks to my postgraduate colleagues for their help throughout my research.

Last but not least, I would like to express my sincere gratitude to all my friends tor their support and encouragement throughout the years in this project. My greatest thank goes to my parents and family members who have always supported me in every step of my life. Thank you very much.

TABLE OF CONTENTS

LIST OF FIGURES

LIST OF TABLES

LIST OF SYMBOLS AND ABBREVIATIONS

atm	:	Standard atmosphere
at%	:	Atomic percentage
α	:	Absorption coefficient
cm	:	Centimeter
e^-	:	Electron
eV	:	Electronvolt
h	:	Planck’s constant
h^+	:	Hole
mL	:	Milliliter
mm	:	Millimeter
min	:	Minute
nm	:	Nanometer
ppb	:	Part per billion
ppt	:	Part per trillion
s	:	Second
μm	:	Micrometer
V	:	Voltage
ν	:	Frequency of vibration
wt%	:	Weight percentage
λ	:	Radiation wavelength
θ	:	Diffraction angle
℃	:	Degree Celsius
1D	:	One-dimensional
C	:	Carbon

CB	:	Conduction band
CVAAS	:	Cold-Vapor Atomic Absorption Spectrometry
DI	:	Deionized
DRS	:	Diffuse Reflectance Spectroscopy
DSSC	:	Dye sensitized solar cell
EDX	:	Energy dispersive X-ray spectroscopy
EG	:	Ethylene glycol
F	:	Fluorine
FESEM	:	Field emission scanning electron microscope
H_2	:	Hydrogen
HOMO	:	Highest occupied molecular orbital
H_2O	:	Water
H_2O_2	:	Hydrogen peroxide
H_2SO_4	:	Sulphuric acid
HF	:	Hydrofluoric acid
Hg	:	Mercury
$HgCH_3$	:	Methylmercury
$HgCl_2$	:	Mercury chloride
I	:	Iodine
KF	:	Potassium fluoride
Li	:	Lithium
LUMO	:	Lowest unoccupied molecular orbital
Na_2SO_4	:	Sodium sulphate
NH_4F	:	Ammonium fluoride
O_2	:	Oxygen
•OH	:	Hydroxyl radicals

PL	:	Photoluminescence
Pt	:	Platinum
$SnCl_2$	:	Tin chloride
Ti	:	Titanium
TiO_2	:	Titanium dioxide
UV	:	Ultraviolet
VB	:	Valence band
W	:	Tungsten
WO_3	:	Tungsten trioxide
XPS	:	X-ray photoelectron spectroscopy
XRD	:	X-ray diffraction

CHAPTER 1: INTRODUCTION

This chapter consists of the overall discussion on the mercury issues in which the research topic is concerned, the aims, motivations, as well as the outline of the research scope.

1.1 Introduction

Environmental pollution and exposure to toxic material are an increasingly serious problem all over the world. Heavy metals are not biodegradable, have long biological half-lives, and the capacity to accumulate in different organs of the body, causing unwanted side effects. There has been continual concern about the issue of pollution by heavy metal because of their toxicity for plant, animal and human beings and their lack of biodegradability. This pollution issue is largely due to rapid industrialization in the past few decades which has taken a heavy toll on the environment and the earth ecosystems.

Mercury is one of the most toxic heavy metals in the world, yet widely used in many industries due to its unique physio-chemical properties (liquid form at STP, high surface tension, high specific gravity, low electrical resistance). Thus, mercury pollution in the environment has grown throughout the years along with the growth of industries such as metallurgy, manufacturing, medicine, and mining in which mercury plays a vital role. The threat of mercury pollution has been well-known throughout the world since decades ago due to several catastrophic incidents, with several severe cases such as the Minamata catastrophe which caused extremely high prevalence rate of neurological and mental disorders in the Minamata region. Therefore, executing research for new methods of efficient mercury remediation has been the passion for scientists, which can provide better and more sustainable solutions for this environmental problem.

To date, photocatalytic metal oxide semiconductors have been established as a potential solution for environmental mercury pollution. In order to bring these materials to the point of commercial readiness, substantial research on the development of semiconductor for mercury remediation using solar energy has to be developed. Although a number of semiconductor have been reported to be active photocatalysts for photoreduction of mercury ions, most of them only function under ultraviolet (UV) light ($\lambda < 400$ nm) owing to the wide band gap energy. Since nearly half of the solar energy incident on the earth's surface falls in the visible region ($400 < \lambda < 800$ nm), the efficient use of visible light is essential for photocatalytic mercury removal. Unfortunately, photocatalytic reduction of mercury ions using visible light is difficult to achieve due to the band level of the metal oxide semiconductors are rather difficult to be tuned to the visible region. To date, no known semiconductor that simultaneously meets all the criteria for photocatalytic mercury removal has been discovered.

Among the many photocatalytic materials, titanium dioxide (TiO_2) has emerged as the leading candidate for many applications such as solar cells, hydrogen generation, gas sensing, and photocatalysis. This is due to the unique characteristics of TiO_2 such as non-toxicity, cost effective, long-term stability, widespread availability, corrosion stability, and high photocatalytic ability. Thus, it is no surprise that TiO_2 is a metal oxide semiconductor that showed potential as a solution for environmental mercury pollution. TiO_2 has been proven to be a potential adsorbent for many contaminants such as dyes and heavy metals. Furthermore, TiO_2 is a transition metal oxide semiconductor (with band gap of 2.99–3.20 eV) which is active under UV light irradiation. Thus, TiO_2 can also act as a photoreductor of heavy metal ions when irradiated with UV light. One dimensional TiO_2 nanotubes are considered a promising candidate because of their inner and outer wall surface area of nanotubes that greatly increases the active sites available for contaminant adsorption. Compared to a film of TiO_2 nanoparticles, nanotubes have been shown to provide directionality benefits in oriented arrays through improvements in unique electronic properties, such as separation of charges, high electron mobility, low quantum confinement effects, and high mechanical strength. Furthermore, compared to randomly-oriented particulate TiO_2, vertical charge transport in well-aligned TiO_2 nanotubes structure greatly contributes to better photocatalytic efficiency due to the grains of TiO_2 are stretched in the tube growth direction and low recombination losses at grain boundaries.

However, the main obstacle to the widespread use of TiO_2 as a photocatalyst is its poor visible light utilization due to its large band gap of about 3.2 eV and the rapid recombination of photo-induced electron/hole pairs. In recent years, researchers have reported that the visible light absorption of TiO_2 can be improved by coupling TiO_2 with another semiconductor to change the optical, electronic and functionality of TiO_2 by inducing additional electronic state in the band gap.

In this research, tungsten trioxide (WO_3) was selected as potential dopant to decorate the pure TiO_2 nanotubes using *in situ* anodization method in order to improve the photocatalytic ability of TiO_2. The main reason mainly attributed to the WO_3 has a smaller band gap of 2.3–2.8 eV, which is advantageous for visible-light-driven photocatalysis, and has strong absorption in the visible range (400-700 nm). Furthermore, the upper edge of the valence band and the lower edge of the conduction band are lower for WO_3 than for TiO_2, thus creating a potential gradient at the composite interface which allows electron transfer from the conduction band of TiO_2 down to the conduction band of WO_3. This will improve charge separation and inhibit charge carrier recombination.

1.2 Problem Statement

TiO_2-based materials have been broadly studied as the most promising photocatalyst for environmental remediation such as air purification, water purification, heavy metals degradation, and hazardous waste remediation. The reasons mainly attributed to the non-toxicity, cost effective, long-term stability, widespread availability, high stability against photo-corrosion with great capacity for oxidation and high photocatalytic property. TiO_2 is an ideal semiconductor material for photocatalysis because it is non-toxic, relatively cheap and highly photostable. When TiO_2 is excited by UV light irradiation, electrons from valence band will jump to the conduction band leaving behind positive holes (h^+). The electrons and holes diffuse to the particle surface of the TiO_2 in which they can be exploited for various redox processes analogous to those of an electrochemical cell.

However, bulk TiO_2 has its own limitations which are critical to photocatalytic techniques. Generally speaking, because of its relatively low specific surface area, photocatalytic activity of bulk TiO_2 needed to improve. Therefore, maximizing the specific surface area of TiO_2 is crucial to maximize photon absorption and improve its photocatalytic performance.

One-dimensional (1D) TiO_2 nanotube arrays fabricated by direct anodization of titanium are considered good photocatalysts because of their greater surface area to volume ratio (where high photon absorption is expected) with controllable dimensional features (e.g., pore size, length, wall thickness) and provide excellent short transportation pathway for photo-induced electrons transfer with minimum electron loss. Also, incident photons are much more effectively absorbed than on a flat thin film surface due to the light scattering phenomenon (Lai & Sreekantan, 2013). Furthermore, compared to a film of TiO_2 nanoparticles, nanotubes have been shown to provide directionality benefits in oriented arrays through improvements in electron mobility and separation of charges (Baker & Kamat, 2009). Nanotubes arrays which can be directly grown on a support material also have the advantage over TiO_2 particles or spheres which requires appropriate substrates as support for the catalysts in mercury removal systems to ease the filtration procedure (Nischk et al., 2014).

Another limitation of TiO_2 which needs to be overcome is the fast recombination of photo-generated electron-hole pairs. In bulk TiO_2, the presence of defects or trapping sites, more grain boundaries, and disordered contact areas between two particles or spheres causes the electron transporting time to be rather long, which leads to more recombination losses and scattering problems of photo-induced electrons. However, this drawback is very much related to the wide band gap of TiO_2 nanotubes and cannot be overcome by only optimizing the dimensional features of TiO_2 nanotubes itself. The photocatalytic reduction of mercury ions is largely controlled by the electron-hole recombination rate. Therefore, high photocatalytic mercury removal efficiency could only be achieved with a suitable architecture that minimizes the recombination of photogenerated electron-hole pairs by quickly separating them before the electron-hole pairs lose their energies in the form of heat or photon through recombination in bulk or on the photocatalyst surface (Lai & Sreekantan, 2011).

Considerable efforts have been exerted to reduce the recombination rate of charge carriers by coupling a narrow band-gap metal oxide semiconductor with TiO_2 nanotubes. In this study, TiO_2 nanotubes are be modified with the addition of tungsten ions to suppress the recombination of charge carriers. Since WO_3 has a slightly lower conduction band than TiO_2, the photoelectrons are prone to transfer from the conduction band of TiO_2 to that of WO_3 and result in the effective charge carrier separation when TiO_2 nanotube array is coupled with WO_3 (Jing Wang et al., 2011). As a basic function, the band-gap of WO_3 is relatively small (2.4 eV - 2.8 eV) than TiO_2 (3.0 eV - 3.2 eV), which allow the transfer of electrons from bulk TiO_2 to WO_3 and further minimize the recombination losses.

1.3 Objectives of Research

The aims of this research include:

- To study the effect of anodic oxidation parameters (electrolyte composition, applied potential, time) on the anodic-growth kinetics of WO_3-loaded TiO_2 nanotubes via single step electrochemical anodization technique.
- To investigate the efficiency of mercury removal using WO_3-loaded TiO_2 nanotubes film as compared to pure TiO_2 nanotubes under UV irradiation.

1.4 Outline of Research Work

Overall, there are three main sections in this research project which include the synthesis of WO_3-loaded TiO_2 nanotubes, materials characterization, and mercury removal performance test. These three well-organized work scopes will be investigated carefully in order to achieve the aims mentioned in Section 1.3.

1.4.1 Synthesis of WO_3-loaded TiO_2 Nanotubes

In this stage, WO_3-loaded TiO_2 nanotubes were primarily synthesized through single step electrochemical anodization technique. Basically, the Ti foil was anodized with W foil as the cathode for the preparation of the nanotubes. High purity Ti sheets were degreased by sonification in acetone. Then, Ti sheets were rinsed with deionized water and dried with nitrogen stream. Prior to anodization, etching agent of NH_4F was added into ethylene glycol electrolyte. The mixture of solution was stirred by magnetic agitation for 1 hour to dissolve the NH_4F into the ethylene glycol homogenously. Electrochemical anodization was performed in a two-electrode configuration bath with

Ti sheet as the anode and W sheet as the cathode, which was connected to a programmable DC power supply. The electrochemical anodization was carried out with different applied potential, exposure time, and fluoride content under real time observation of current density time transient behaviour. Upon finishing electrochemical anodization, as-anodized substrate was transferred immediately into acetone, and subjected to sonification for 1 minute in order to remove debris and precipitate layers at the entrance of nanopores. Heat treatment converted innate amorphous structure of as-anodized nanotube arrays to desired phases. The detailed procedures used to prepare the samples are discussed in Chapter 3- Research Methodology.

1.4.2 Materials Characterization

In this stage, various characterization techniques were used to characterize the physical and chemical properties, such as structural, morphological, and optical properties of the WO_3-loaded TiO_2 nanotubes synthesized via single step electrochemical anodization technique. The surface and cross-sectional morphologies of the anodized samples were viewed by Field Emission Scanning Electron Microscopy (FESEM). The elemental analysis was determined with Energy Dispersive X-Ray Spectroscopy (EDX) analysis. Besides, X- ray diffraction (XRD) and Raman Spectroscopy techniques were used to investigate the phase composition of the samples. The samples were also subjected to Photoluminescence Spectroscopy (PL) and UV-vis Diffuse Reflectance Spectroscopy (UV-vis DRS) measurements in order to determine the carrier recombination and optical properties of the WO_3-loaded TiO_2 nanotubes respectively. Other than that, high sensitivity surface analysis of X-ray Photoelectron Spectroscopy (XPS) testing was used to identify the elemental composition, chemical state, oxidation state, and electronic state from the sample surface. The principle and the measuring conditions of each measurement are discussed in Chapter 3- Research Methodology.

1.4.3 Mercury Removal Performance Test

In this stage, the well-characterized WO_3-loaded TiO_2 nanotubes were applied in mercury removal through adsorption-reduction reaction. A custom-made photoreactor with TUV 96 W UV-B Germicidal light was used for testing the mercury removal ability of the WO_3-loaded TiO_2 nanotubes. The performance of the WO_3-loaded TiO_2 nanotubes in the removal of mercury ions were analyzed by using Cold-Vapor Atomic Absorption Spectrometry (CVAAS).

1.5 Outline of thesis

This thesis is organized into five chapters consecutively. Chapter 1 includes the introduction of this research work, problem statement, research objectives, the outline of research work as well as thesis overview. In Chapter 2, the different types of TiO_2, applications of TiO_2, and synthesis methods of TiO_2 nanostructures are presented. Chapter 2 also comprises the literature review on mercury applications, impacts, and remediation. Chapter 3 illustrates the specifications of the raw materials, research methodology, and the characterizations employed in this research. The results of characterizations and the discussions are presented in Chapter 4. Lastly, Chapter 5 summarizes the conclusion of the study as well as several suggestions and recommendations for future work.

CHAPTER 2: LITERATURE REVIEW

2.1 Types of TiO_2

TiO_2, also known as titanium (IV) oxide or titania, is the naturally occurring oxide of titanium. TiO_2 is a wide-bandgap semiconductor ($E_g \approx 3$ eV) in all its crystal forms and has unique optical, ionic and electronic properties (X. Chen & Mao, 2007; Roy et al., 2011).

The three main crystal forms of TiO_2 are anatase, rutile, and brookite. Brookite type TiO_2 has an orthorhombic crystal structure and is difficult to synthesize and thus is seldom studied. Another five high-pressure phases of TiO_2 have been reported which are TiO_2II or srilankite (an orthorhombic polymorph of the lead oxide structure), cubic fluorite-type polymorph, pyrite-type polymorph, monoclinic baddeleyite-type polymorph, and cotunnite-type polymorph (Hanaor & Sorrell, 2011). Anatase and rutile phases will be discussed in detail as these are the two important polymorphs of titanium dioxide which have potential for the application of the photocatalytic effect in TiO_2.

Table 2.1: Properties of anatase and rutile (Fisher & Egerton, 2001; Beltran et al., 2006)

Property	**Anatase**	**Rutile**
Crystal structure	Tetragonal	Tetragonal
Atoms per unit cell (Z)	4	2
Density (g cm^{-3})	3.8	4.2
Calculated indirect band gap (eV)	3.23 - 3.59	3.02 - 3.24
(nm)	345.4 - 383.9	382.7 - 410.1
Experimental band gap		
(eV)	~3.2	~3.0
(nm)	~387	~413

Anatase TiO_2 corresponds to the tetragonal system (with dipyramidal habit) crystalline structure and is usually used as a photocatalyst under UV irradiation. Anatase transforms irreversibly to rutile at elevated temperatures (Hanaor & Sorrell, 2011). This transformation does not have a unique temperature and the processes that are involved in the transformation as well as the methods to inhibit or promote this transformation have not been reviewed comprehensively to date. Anatase is less dense and less stable than rutile phase (rutile is stable phase while anatase is metastable) (Tang et al., 1995). However, generally anatase is more active than rutile because charge carriers for photocatalytic reactions can originate from much deeper in the bulk for anatase than for rutile (Luttrell et al., 2014). Anatase TiO_2 also has a more negative conduction band edge potential (higher potential energy of photogenerated electrons), high specific area, inexpensive, non-toxic, and photochemically stable (Macwan et al., 2011). Also, anatase particles with a large surface area are efficient for the decomposition of pollutants in air and water (Ohno et al., 2001). At comparatively low temperatures (600-800 ℃), anatase can be stabilized in the form of thin films, powder, ceramic, and synthetic or natural crystals.

Rutile TiO_2 with tetragonal crystal structure (with prismatic habit) is mainly used as white pigment in paint because of its maximum light scattering with virtually no absorption, nontoxic, and chemically inert (Park et al., 2000). Rutile is favored over anatase in this application because rutile scatters white light more efficiently and is chemically more stable than anatase at all temperatures (Hanaor & Sorrell, 2011; Park et al., 2000). However, for photocatalytic applications, anatase is favored for its higher activity due to its surface chemistry and potentially higher conduction-band edge energy (Park et al., 2000). Despite this, rutile should not be overlooked as a potential material for applications such as solar cells because rutile is potentially cheaper to produce and has superior light-scattering characteristics, which is a beneficial property for light harvesting (Park et al., 2000). Thermodynamic studies have shown that negative pressures are required for anatase to be more stable than rutile. Thus, the transformation of anatase to rutile is irreversible (Hanaor & Sorrell, 2011). As shown in Figure 1, it is generally concluded that standard state anatase to rutile phase transformation occurs at temperatures from 600 to 700 ℃ (X. Chen & Mao, 2007; Hanaor & Sorrell, 2011; Roy et al., 2011).

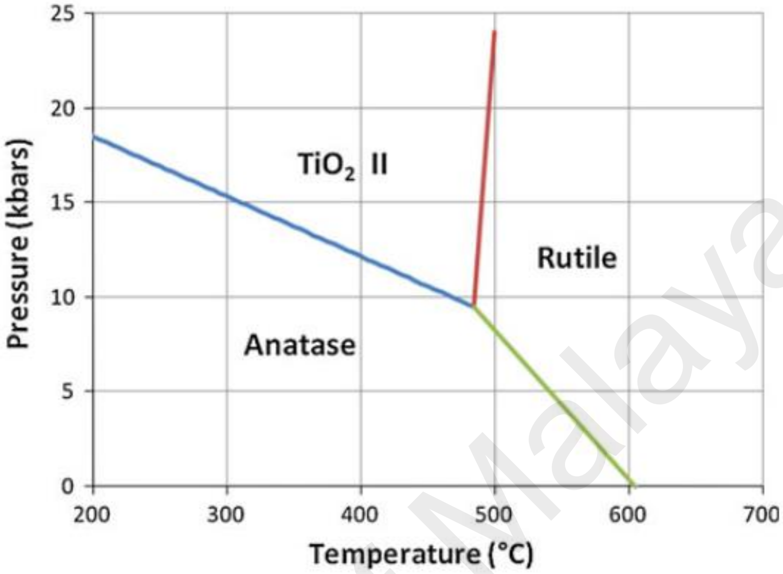

Figure 2.1: Reaction boundaries of phase transitions in TiO_2 (Hanaor & Sorrell, 2011)

2.2 Applications of TiO_2

TiO_2 has become one of the most researched transition metal oxide semiconductor materials due to its unique and beneficial physical and chemical properties. Bulk TiO_2 is a useful non-toxic, environment friendly and corrosion-resistant material frequently used in ointments, toothpaste, sun-blockers, paint, and pigments. It is also widely used in medicine as it shows exceptional biocompatibility (X. Chen & Mao, 2007; Macwan et al., 2011; Roy et al., 2011). In recent years, TiO_2 nanostructures have become the topic of interest for many researchers worldwide due to its many potential applications. The unique features and properties of TiO_2 (electronic, ionic, or biocompatibility properties) are usually exploited for the applications of TiO_2 nanostructures due to the significant enhancement of reaction or transport rates by using small scale dimensions (large surface area, short diffusion path, or size confinement effects) (X. Chen & Mao, 2007; Roy et al., 2011).

Currently, the existing and potential applications of TiO_2 nanomaterials include paint, toothpaste, UV protection, photocatalysis, photovoltaics, solar cells, hydrogen generation, sensing, and electrochromics as well as photochromics (Abidi et al., 2009; Feng et al., 2012; Montazer & Seifollahzadeh, 2011; Tian et al., 2013; Vuong et al., 2013; Wei et al., 2013). TiO_2 nanomaterials normally have electronic band gaps larger than 3.0 eV and high absorption in the UV region. TiO_2 nanomaterials are also very stable, nontoxic, and cheap. Their optical and biologically inert properties allow them to be suitable for UV protection applications. However, certain TiO_2 applications require specific crystallographic structures for optimized performance. For example, anatase form of TiO_2 shows the highest solar energy conversion efficiency and has the highest activity for catalysis (Grätzel, 2001; Macak et al., 2007).

2.2.1 Photocatalytic Applications

After Fujishima and Honda discovered the phenomenon of photocatalytic water splitting using TiO_2 electrode under ultraviolet (UV) light, numerous researchers have devoted their efforts towards the research of TiO_2 for photocatalytic applications. Since then, researchers have found TiO_2 to be an excellent photocatalyst with a long-term stability, low preparation cost and possesses enough oxidizing power for the decomposition of unwanted organic compounds (Krýsa et al., 2005). In recent years, TiO_2 was proven to be such an excellent photocatalyst that it is regarded as the most efficient and environmentally benign photocatalyst, and it has been most widely used for photodegradation of various pollutants (X. Chen & Mao, 2007; Cheng et al., 2013; Fang et al., 2013; J. Lee & Choi, 2004; Natarajan et al., 2013; Sahoo et al., 2005). This high activity is due to the band edge positions relative to typical environments such as water (Roy et al., 2011). The basic principles involved in the photocatalytic decomposition mechanism are shown in Figure 2.2.

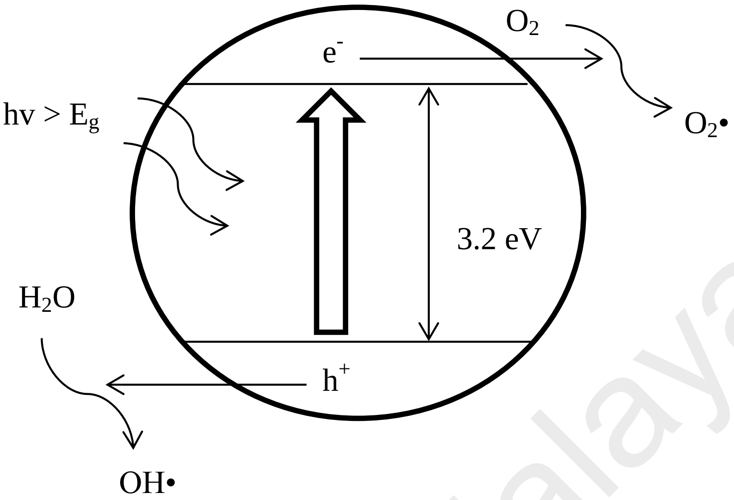

Figure 2.2: Principle of the photocatalytic decomposition on TiO_2 surface

The principle of the semiconductor photocatalytic reaction is straightforward. Photons from a light source with energy larger than the band gap of TiO_2 excite electrons from the valence band to the conduction band of TiO_2 which results in electrons and holes separation (under the field of the Schottky junction with the environment), forming charge carrier pairs. When the electrons and holes migrate to the semiconductor-environment interface, they will react with adsorbed molecules. In aqueous solutions, valence band holes from TiO_2 typically react with H_2O to form OH• radicals, while electrons in the conduction band mainly reduce dissolved molecular oxygen to form super-oxide $O_2^{\bullet}$ anions. These radicals and photogenerated holes are extremely strong oxidants which are able to oxidize all organic materials to CO_2 and H_2O. Other than that, direct h^+ transfer from the valence band to adsorbed species to initiate decomposition can also be considered.

Apart from decomposition of organics, the charge carrier pairs can react with H_2O to form H_2 and O_2 to achieve direct splitting of water. At the conduction band, the redox potentials for O_2 to O_2^- and H^+ to $^1/_2H_2$ are very close. In other words, H_2 generation and O_2 formation are typically competing. At the valence band, O_2 can be formed from water by various pathways, including radicals that can react finally to O_2. At the valence band, catalysts such as platinum are often used to promote H_2 evolution, and hole scavengers such as CH_3OH are often used to promote the overall reaction rate (Roy et al., 2011).

The photocatalytic activity of a semiconductor is largely controlled by the light absorption properties (light absorption spectrum and coefficient), reduction and oxidation rates on the surface by the electron and hole, and the electron-hole recombination rate (X. Chen & Mao, 2007). To achieve maximum decomposition efficiency, in addition to adequate band edge positions, rapid charge separation and high quantum yield, a large area of the catalyst is desired. This is because a large surface area with a constant surface density of adsorbents leads to faster surface photocatalytic reaction rates. However, because the surface is a defective site, the larger surface area will contribute to faster recombination. On the other hand, higher crystallinity leads to higher photocatalytic activity due to fewer bulk defects. In order to improve the crystallinity of TiO_2 nanomaterials, high temperature treatment is usually utilized, which in turn can induce the aggregation of small nanoparticles and decrease the surface area (X. Chen & Mao, 2007; Roy et al., 2011).

2.2.2 Solar cells

Another attractive application of TiO_2 that shows much potential is dye-sensitized solar cells (DSSC). During the 1970s, dye sensitization of TiO_2 was extensively investigated (Roy et al., 2011). Dye-sensitization of a TiO_2 electrode with suitable species relies on the fact that certain organic dyes (mainly Ru-complexes) can be anchored on TiO_2 and can inject excited electrons from their lowest unoccupied molecular orbital (LUMO) into the conduction band of TiO_2 upon light excitation because the LUMO of these dyes overlaps with the conduction band edge of TiO_2. As the HOMO/LUMO distance of these dyes typically is only 1 - 2 eV, the reaction can be triggered by visible light. The operating principle of the DSSC is given in Figure 3. The principle of DSSC involves a photon-absorber layer made of nanocrystalline mesoporous TiO_2 film that is dye coated and placed in contact with a redox electrolyte or an organic holes conductor. The dye absorbs light in the visible range and excites electrons from the HOMO to the LUMO level, thereby injecting the excited electrons into the conduction band of TiO_2. These electrons then travel through the TiO_2 to the back contact and then conducted to the outer circuit to drive the load and make electric power. Subsequently, the original state of the dye is regenerated by electron donation from the electrolyte, usually an organic solvent containing a redox system, such as the I^- / I_3^- couple (X. Chen & Mao, 2007; Roy et al., 2011).

Losses by recombination may happen in three ways: 1) After electron excitation from the HOMO to the LUMO level of the dye, de-excitation of the electron occurs in a radiative or non-radiative path; 2) after injection of the electron in the conduction band of TiO_2, it may recombine with the oxidized dye; and 3) the electron may recombine with the I_3^- ion in the electrolyte. The regeneration of the oxidized dye by iodide prevents the recapture of the conduction band electron by the oxidized dye. Subsequently, the iodide is regenerated by the reduction of triiodide at the counter electrode, with the circuit being completed via electron migration through the external load. The voltage generated under illumination corresponds to the difference between the Fermi level of TiO_2 and the redox potential of the electrolyte. Overall, the device generates electric power from light without suffering any permanent chemical transformation (Grätzel, 2001; Macak et al., 2007). A typical dye-sensitized TiO_2 nanoparticle-based solar cell is shown in Figure 2.3.

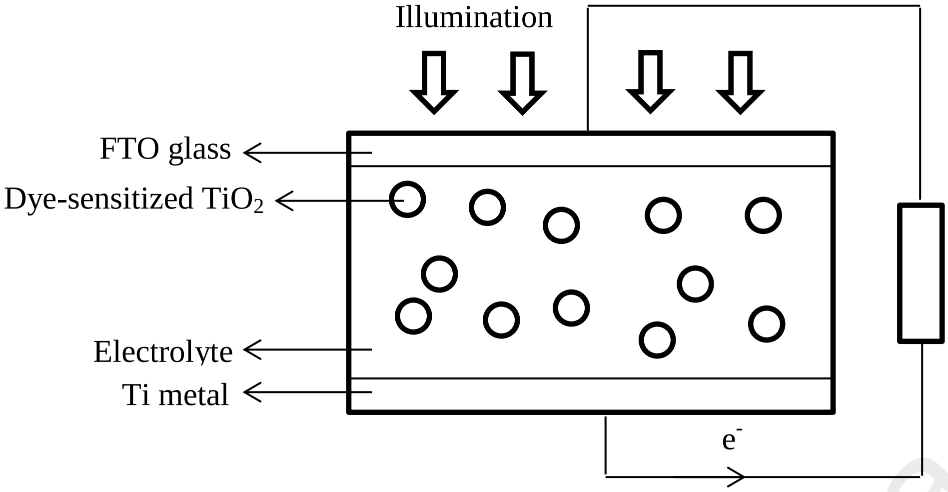

Figure 2.3: A dye-sensitized TiO_2 nanoparticle-based solar cell (Roy et al., 2011)

2.2.3 Electrochromic devices

Electrochromism is the ability of a material to undergo change in color upon oxidation or reduction. Electrochromic devices are able to vary their throughput of visible light and solar radiation when electrically charged and discharged using a low voltage. A small applied voltage will cause them to darken, while reversing the voltage causes them to lighten. The principle of electrochromism requires a molecule which functions as the electrochromophore (exhibits different colors in different oxidation states) with redox potential that lies above the conduction band edge of TiO_2 at the liquid/solid interface. This allows electrons to transfer reversibly from the conduction band to the molecule. If the redox potential is situated below the conduction band edge, the reduction process is irreversible.

A specific property of TiO_2 is its ability to serve as a host for hydrogen ion or lithium ion insertion. In recent years, TiO_2 nanomaterials have been widely used as electrochromic devices such as electrochromic displays and windows as these devices rely on a reversible uptake of small ions such as H^+ and Li^+ into interstitial positions of the TiO_2 upon applying and releasing an electric field. Ion uptake and its release are frequently accompanied with a change in the redox state of the material besides results in a change of electronic and optical properties of the material. A common example is nanocrystalline TiO_2 electrodes in Li containing electrolytes related to the reversible insertion of Li^+ into the anatase lattice of the nanoparticles, accompanied with reduction of Ti^{4+} at the lattice to Ti^{3+}, which changes the apparent bandgap of the material from the UV to the visible range which leads to a blue coloration of the material. The nanocrystalline structure of the TiO_2 film makes possible 100- to 1000-fold amplification compared to a flat surface. The combination of high conductivity of the nanocrystalline TiO_2 particles, fast electron exchange with the molecular monolayer, optical amplification by the porous structure, and fast charge compensation by ions in the contacting liquid makes the nanocrystalline electrodes highly attractive electrochromic elements.

The kinetics and magnitude of ion insertion and the electrochromic reaction (contrast) strongly depend on the ion diffusion length, solid-state diffusion/migration process of the small ion into the host lattice and therefore on geometry of the electrode surface. The switching kinetics is typically comparably slow (seconds). Thus, nanoscale materials are highly desired to achieve short diffusion paths. At reasonable applied voltages (1 - 2 V) and moderate times (seconds), a compacted layer of nanoparticles can typically be intercalated to a depth of approximately 5 - 10 nm. This length scale is ideal for penetration of TiO_2 nanotube walls (with wall thicknesses in the range of 5 - 30 nm). Furthermore, due to its vertical alignment, the TiO_2 nanotube geometry is ideal for maximizing the optical contrast. The basic principles of TiO_2 electrochromism is shown in Figure 2.4.

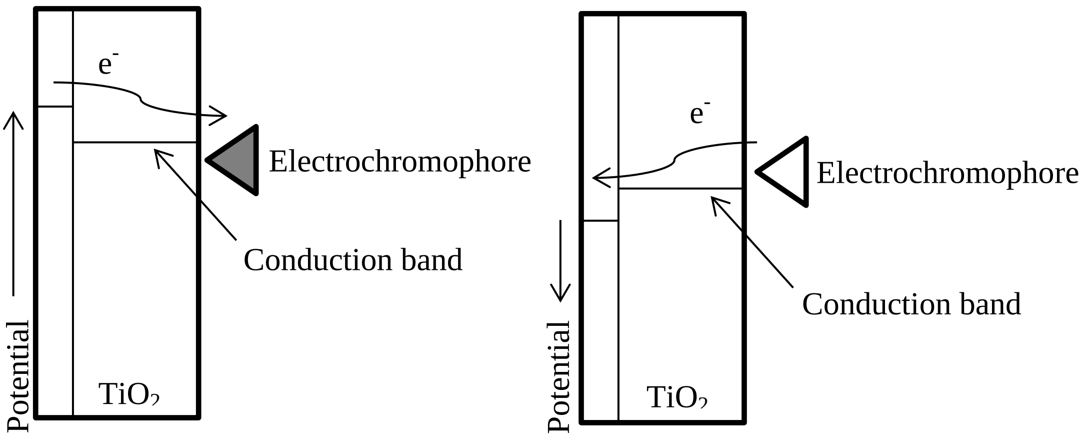

Figure 2.4: Schematic illustration of the principle of electrochromism (X. Chen & Mao, 2007)

2.2.4 Sensing applications

Another application of TiO_2 is gas sensing for various gases. In terms of gas sensing, TiO_2 layers have shown to have a high sensitivity to CO, H_2, and NO_x gases, and in particular as nanoparticulated films (Kim et al., 2006; Seo et al., 2009). TiO_2 nanotube layers have also demonstrated sensitivity for these gas sensing applications (Varghese et al., 2003). Grimes et al. have found that TiO_2 nanotubes are excellent room temperature hydrogen sensors as it has a high sensitivity of 10^4 and also the ability to self-clean photoactively after environmental contamination (Mor et al., 2004). At room temperature (24 °C), the sensors responded to 1000ppm of hydrogen with a fully reversible change in electrical resistance of about 175,000%. When extinguished through sensor contamination, the hydrogen-sensing capabilities of the sensors can be mostly recovered through ultraviolet (UV) light exposure. Other than that, the enhanced reaction rate of gold nanoparticles supported on TiO_2 nanotube layers with O_2 in aqueous solution shows a promising application as oxygen sensors (Macak et al., 2007).

.

2.2.5 Mercury Removal

In recent years, many researchers have used TiO_2 as a photocatalyst or adsorbent for heavy metal removal application and one of the popular heavy metal is mercury. TiO_2 can be employed for the adsorption of Hg(II) ions in aqueous solution and adsorption equilibrium has been reported to be achieved in 7 hours at pH 8 (Ghasemi et al., 2012). However, other researchers claimed that the main mechanism for removal of Hg(II) from aqueous solutions by utilizing TiO_2 is photocatalytic reduction as there was almost completely no adsorption of Hg(II) on TiO_2 in the absence of light (Katebat et al., 2014; Lenzi et al., 2011). The performance of TiO_2 photocatalyst in this application is highly dependent on pH. Performance is enhanced as pH is increased, with the highest efficiency reported at about pH 10. Organic additives such as methanol also enhanced the photocatalytic reduction to Hg^0 as these additives serve as hole scavenger which decreases recombination of photogenerated electron-hole pair (Dou & Chen, 2011; López-Muñoz et al., 2011). Anatase TiO_2 nanoparticles have also been reported to be able to remove Hg(II) by more than 65 % within 30 minutes under UV illumination (Dou & Chen, 2011). However, some researchers have shown that synthesized TiO_2 nanotubes performed better than commercial nanoparticles. They reported that the nanotubes managed to remove 97 % of the initial mercury concentration within 30 minutes reaction time as compared to only 80 % using the commercial nanoparticles (Katebat et al., 2014). The rate of photocatalytic reduction of Hg(II) in aqueous solution by TiO_2 increases with increasing temperature but the adsorption shows a decline when temperature rises because the adsorption is an exothermic process (Dou et al., 2011). In order to improve the photocatalytic performance of TiO_2 in mercury removal, researchers have also doped TiO_2 with metals. By doping Ag on the surface of TiO_2, a group of researchers performed photocatalytic reduction of Hg(II) in aqueous solution containing formic acid and reported that almost all the Hg(II) ions were reduced to Hg^0

within 3 hours (Lenzi et al., 2011). Another group of researchers who used silica-titania composite to remove trace levels of Hg(II) in aqueous solution reported that 90 % Hg(II) removal was achieved within 1 hour with adsorption alone and only slightly better results with UV illumination (Byrne & Mazyck, 2009).

2.3 TiO_2 Nanostructure Synthesis Methods

In many of its applications, TiO_2 have shown better performance when it is in nanosize. This is especially true in the case of photocatalysis as larger surface area will enhance catalysis activity. Thus, the use of nanostructures as photocatalyst has attracted much attention.

TiO_2 nanoparticles can be synthesized using sol-gel and precipitation methods (Lee et al., 2010). On the other hand, TiO_2 nanotubes are synthesized using sol-gel, hydrothermal, and anodization techniques (Lai & Sreekantan, 2011; Macwan et al., 2011; Paulus et al., 2011). All the methods mentioned above have certain drawbacks. Out of these methods, anodization has the advantage of producing well-aligned individual nanotubes (Roy et al., 2011).

Typically, sol-gel and hydrothermal methods require precursors to fabricate nanotubes and these precursors are usually commercially available TiO_2 such as Degussa (Lee et al., 2010). Thus, it is inconvenient in terms of costing due to the high cost of purchasing commercial TiO_2. Other than that, sol gel and hydrothermal methods require longer time (up to 10 hours) to produce nanotubes as compared to anodization method. Additionally, these methods consume high amount of chemicals and power for heating, cleaning, and calcining to produce a small amount of nanotubes.

However, the greatest drawback of the sol-gel and hydrothermal methods is that the nanotubes produced are not aligned and well-ordered. This is critical as certain applications such as photocatalysis, solar cell, and gas sensing require well-aligned architecture oxide film to provide specific functional properties. Furthermore, these well-ordered self-organized architecture have high surface area which makes them much more reactive and effective in their applications (Baker & Kamat, 2009).

2.3.1 Sol-gel method

In the sol-gel method, inorganic or organic-inorganic materials are made at relatively low temperature and consist of hydrolysis of the constituent molecular precursors and subsequent polycondensation to glass-like form. This technique allows the incorporation of organic and inorganic additives during the process of formation of the glassy network at room temperature. This method has allowed the formation and study of a large number of sophisticated materials (Brinker & Scherer, 2013).

Nanosize TiO_2 has also been successfully synthesized using the sol-gel method. The precursors are usually organic titanates and the products produced with this method are highly homogenous. The last step in this method is to calcine the gel powder at high temperature, typically 300 ℃ (Macwan et al., 2011).

2.3.2 Hydrothermal method

This method is typically used to produce TiO_2 nanotubes. The raw starting material is usually TiO_2 nanoparticle powder, which is then processed in alkali solution such as NaOH in an autoclave at high temperature up to 150 ℃ and time up to 50 hours. This process will transform the titania nanoparticles into nanotubes. During the hydrothermal treatment, NaOH disturbs the crystalline structure of the TiO_2 crystals and breaks the Ti-O-Ti bonding between the octahedra. This leads to the formation of two dimensional nanosheets. When treated at high temperature, these nanosheets then curl up into nanotubes due to high surface energy (Paulus et al., 2011; Sikhwivhilu et al., 2009).

2.3.3 Anodization method

Due to the simple preparation and ease of processing, TiO_2 synthesis via anodization method has caught the attention of the scientific community. It is a simple process where a titanium substrate is used as anode of an electrochemical anodization setup with electrolytes containing fluoride ions (F^-). Anodization leads to the oxidation of the titanium substrate and the F^- ions will etch the oxide layer to form nanotubular or nanoporous structure, depending on the anodization conditions.

Generally, the morphology of the self-ordered nanostructure is strongly affected by the electrochemical anodization conditions such as anodization potential and electrolyte composition (Lai & Sreekantan, 2011). There are three stages of development of TiO_2 nanotubes synthesis via anodization method.

The first generation of TiO_2 nanotubes was formed using HF electrolytes or acidic HF. The source of F^- ions in this first generation stage came from the HF acid (Kim et al., 2008). This method was established based on the mechanism where the main role played by the F^- ions in the electrolyte. Oxidized Ti species react with oxygen ions from water to form an oxide layer of TiO_2. The applied voltage induces the field ion transport which controls the oxide growth. The field reduces as the oxide layer grows thicker because the system is under constant applied voltage. In the presence of F^- ions, the TiO_2 layer that formed is attacked and dissolved to form nanostructures. This is due to the ability of F^- ion to form water soluble TiF_6^{2-} complexes and its small ionic radius which allows it to enter the growing TiO_2 lattice and transport through the oxide by applied field. The formation of TiF_6^{2-} leads to permanent chemical dissolution of the TiO_2 and prevent formation of $Ti(OH)_xO_y$ on the surface as Ti^{4+} ion that transports to oxide/solution interface can form TiF_6^{2-} (Lai & Sreekantan, 2011).

The second generation anodization was an improvement of the previous generation due to the drawback of the first generation where the TiO_2 layers could only be grown to a thickness not exceeding 600 nm (Roy et al., 2011). This is due to the severe dissolution along the pore walls at the top part of the nanotubes caused by HF, thus shortening the nanotubes. The second generation anodization replaced HF electrolytes with buffered neutral electrolytes containing NH_4F or KF. Most electrolytes used are a mixture of SO_4^{2-} ions from Na_2SO_4 or NH_4SO_4. Using these electrolytes with less corrosive F^- ions, longer nanotubes were produced by adjusting the dissolution rate of TiO_2 through localized acidification at the pore bottom while a benign environment is maintained along the pore mouth and walls (Grimes, 2007). However, researchers have found that the nanotubes formed with this method are limited to 2.4 µm in length. This is due to competition between the formation of porous oxide and its dissolution. As pH strongly affects the chemical dissolution rate, the existence of H^+ limits the length of the nanotubes (Regonini et al., 2010). This has led to the development of the third generation anodization method.

The second generation nanotubes have serrated side walls which causes a variation in wall thickness. This phenomenon is reportedly caused by the electrochemical current transient during anodization due to irregular current oscillations (Cao et al., 2011; Grimes, 2007). Every current transient is accompanied by a pH burst at the pore tip, leading to temporarily increased dissolution rate due to local acidification. Since diffusion is the main effect balancing local acidification, a way to overcome pH bursts is to dampen the fluctuations by decreasing the diffusion constant in the electrolyte. According to Stokes-Einstein relation, diffusion constant, D is proportional to $1/\eta$, where η is the solution viscosity. Therefore, more viscous electrolytes will produce lower current density with lower local acidification and lower amount of competing chemical dissolution. Thus, the fluctuation of the current transient can be reduced and pH burst can be controlled by using highly viscous electrolytes such as glycerol (Grimes, 2007).

2.4 Mercury

Mercury is one of the earliest known metals and has been used by humankind for more than 2300 years (Arshadi, 2015). With the symbol Hg and atomic number of 80, mercury is also known as hydrargyrum or quicksilver. The silvery white mercury freezes into a soft solid at -38.87 ℃ and boils at 356.9 ℃. Placed in the d-block in the periodic table, mercury is an unusual transition metal which is liquid at room temperature and pressure. Moreover, mercury has high vapor pressure at room temperature (1.9 x 10^{-3} torr) and the only element that can exist as a monoatomic vapor besides noble gasses (Hutchison & Atwood, 2003).

The three different forms of mercury are: elemental- Hg^0 (zero valent), inorganic- Hg^I (monovalent) and Hg^{II} (divalent), as well as organic- RHg. The monovalent oxidation state of mercury is only found as the diatomic Hg_2^{II} and never straight as Hg^I (Hutchison & Atwood, 2003). The key properties, fate and transport of different forms of mercury in the environment are summarized in Table 2.2. In the aquatic environment, mercury exists in all its three different forms (elemental, inorganic and organic). Elemental mercury has relatively low water solubility and high volatility. Among the two valences of inorganic mercury, divalent mercury is more widely spread in the environment. Hg(II) consists of Hg^{2+} free ions and various complexes of Hg^{2+} such as chloride, hydroxide and sulfide. There are two categories of aqueous organic mercury which are: covalently-bonded organomercurials (methylmercury and dimethylmercury) and mercuric complexes with organic matter (humid substances) (J. Wang et al., 2010). The common mercury transformations are shown as follows (Rafati-Rahimzadeh et al., 2014):

$$\mathrm{Hg^0} \underset{\text{reduction}}{\overset{\text{oxidation}}{\rightleftarrows}} \mathrm{Hg^{+1}} \text{ or } \mathrm{Hg^{+2}} \underset{\text{demethylation}}{\overset{\text{methylation}}{\rightleftarrows}} \mathrm{HgCH_3/HgCH_3Hg}$$

Table 2.2: Key properties, fate and transport of different forms of mercury (EPA, 1999)

Forms	Elemental (Hg^0)	Divalent (Hg^{2+})	Methylmercury
Key properties	• Comprises 95% of atmospheric mercury	• Comprises 5% of atmospheric mercury • Found in soil and water as complex ions • Forms inorganic mercuric salts	• Produced by bacteria in water or sediment as lipophilic ion • Comprises nearly all mercury in fish
Transport and fate	• Remains airborne • Travels long distances before conversion to other forms and deposition	• Easily deposited on earth's surface • Volatilize or partition into particulates in water and transported to sediment	• Enters food chain and uptakes into fish tissue • Travels up food chain and bioaccumulates, reaching highest concentration in organisms at highest trophic level

There are more than 25 mercury-containing minerals in Earth's mantle, but with the abundance of only about 0.5 ppm. Mercury comes from the principal ore called cinnabar (HgS) with major deposits located in Spain, Slovenia and Italy. Mercury comes from many different sources, which can be divided into two types, which are natural and anthropogenic sources. Figures 2.5 and 2.6 show the global mercury emissions by natural and anthropogenic sources (Pirrone et al., 2010). Almost 70% of the total amount of mercury entering the atmosphere each year is from natural sources (UNEP, 2013). Among the natural sources of mercury emissions, ocean is the major contributor for global mercury emissions, which account for 52% (2682 Mg yr^{-1}) of the estimated total mercury emissions by natural sources. On the other hand, lakes are one of the smallest contributors of mercury, accounting for only 2% (96 Mg yr^{-1}) of the estimated total mercury emissions by natural sources. Studies have shown that the evasion of elemental mercury from surface waters is driven by several factors which are (i) the concentration gradient of mercury between the top-water microlayer and air above the surface water, (ii) solar irradiation which is responsible for the photo-reduction of oxidized mercury in the top-water microlayer, and (iii) the temperature of the top-water microlayer and air above the surface water . Biomass burning was the second largest contributor of mercury emissions by natural sources, at about 13% (675 Mg yr^{-1}) of total emissions. Other major contributors of mercury emissions by natural sources are desert/metalliferous/non-vegetated zones which account for 10% (546 Mg yr^{-1}) of total emissions and tundra/grassland/savannah/prairie/chaparral which account for 9% (448 Mg yr^{-1}) of total emissions. Other natural sources of mercury emission include forests (342 Mg yr^{-1}), agricultural areas (128 Mg yr^{-1}), evasion after mercury depletion events (200 Mg yr^{-1}) and volcanoes and geothermal areas (90 Mg yr^{-1}). In total, the estimated global mercury emission by natural sources in 2008 is 5207 Mg yr^{-1} (Pirrone et al., 2010). The estimated global mercury emission by natural sources in 2008 is illustrated in Figure 2.5.

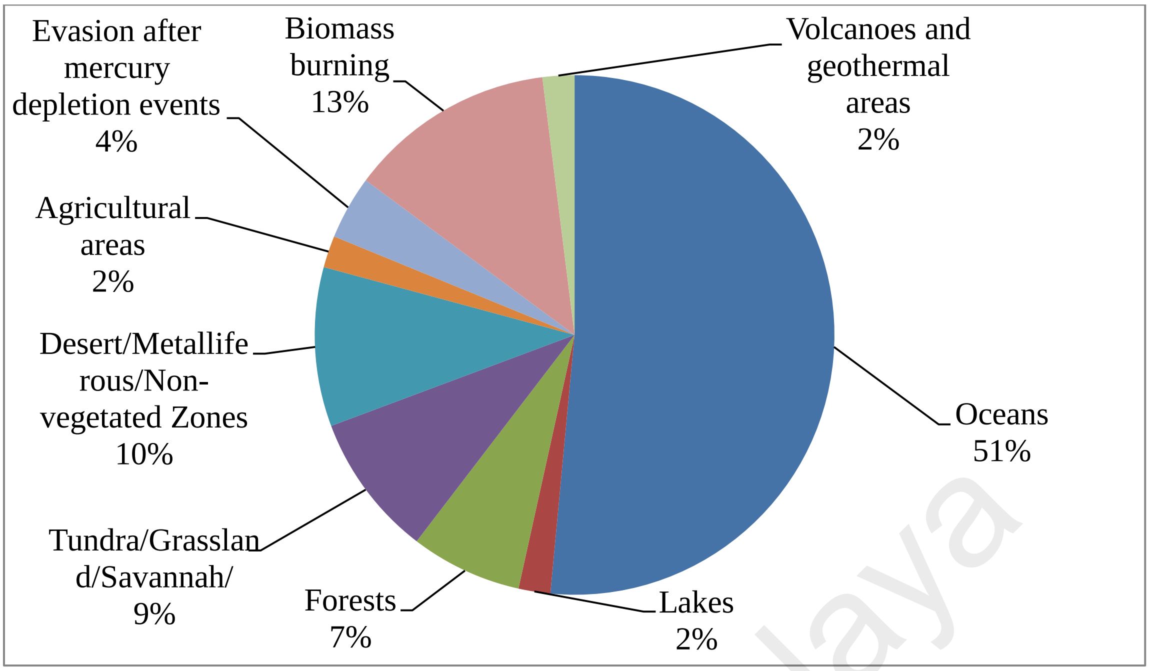

Figure 2.5: Global mercury emissions from natural sources in 2008 (UNEP, 2013)

About 30% of the total amount of mercury entering the atmosphere each year comes from anthropogenic sources (UNEP, 2013). Man-made sources of mercury emission include coal burning, cement production, oil refining, artisanal and small-scale gold production, cremation, oil and natural gas combustion, as well as mining, smelting, and production of iron and non-ferrous metals. Mercury emission from different industrial processes is estimated using three main parameters: the bulk material amount, the mercury content of the material, and the technology adopted to reduce emissions (Pirrone et al., 2010). Among the different anthropogenic sources of mercury emission, artisanal and small-scale gold mining contributed the largest amount of emission, with a total emission of 727 tonnes or 37% of the estimated total mercury emissions by anthropogenic sources. The reason for this large amount of mercury emission is due to the rise in the price of gold along with increase of rural poverty, causing an increase in activity in this sector (UNEP, 2013; Veiga et al., 2006). The next major contributor of mercury emission is coal burning with a total emission of 474 tonnes (24% of the estimated total mercury emissions by anthropogenic sources) followed by primary production of non-ferrous metals (Al, Cu, Pb, Zn) with a total emission of 193 tonnes (10% of the estimated total mercury emissions by anthropogenic sources) and cement production with a total emission of 173 tonnes (9% of the estimated total mercury emissions by anthropogenic sources). Mercury emissions from other anthropogenic sources are relatively minor, such as consumer product waste (95.6 tonnes), large scale gold production (97.3 tonnes), contaminated sites (82.5 tonnes), primary production of ferrous metals (45.5 tonnes), oil and natural gas burning (9.9 tonnes), oil refining (16 tonnes), chlor-alkali industry (28.4 tonnes), mine production of mercury (11.7 tonnes), and cremation (dental amalgam) (3.6 tonnes). As a result of human activity, an estimated total of 1960 tonnes of mercury was released into the atmosphere in 2010 (UNEP, 2013). The global mercury emission from anthropogenic sources in 2010 is illustrated in Figure 2.6.

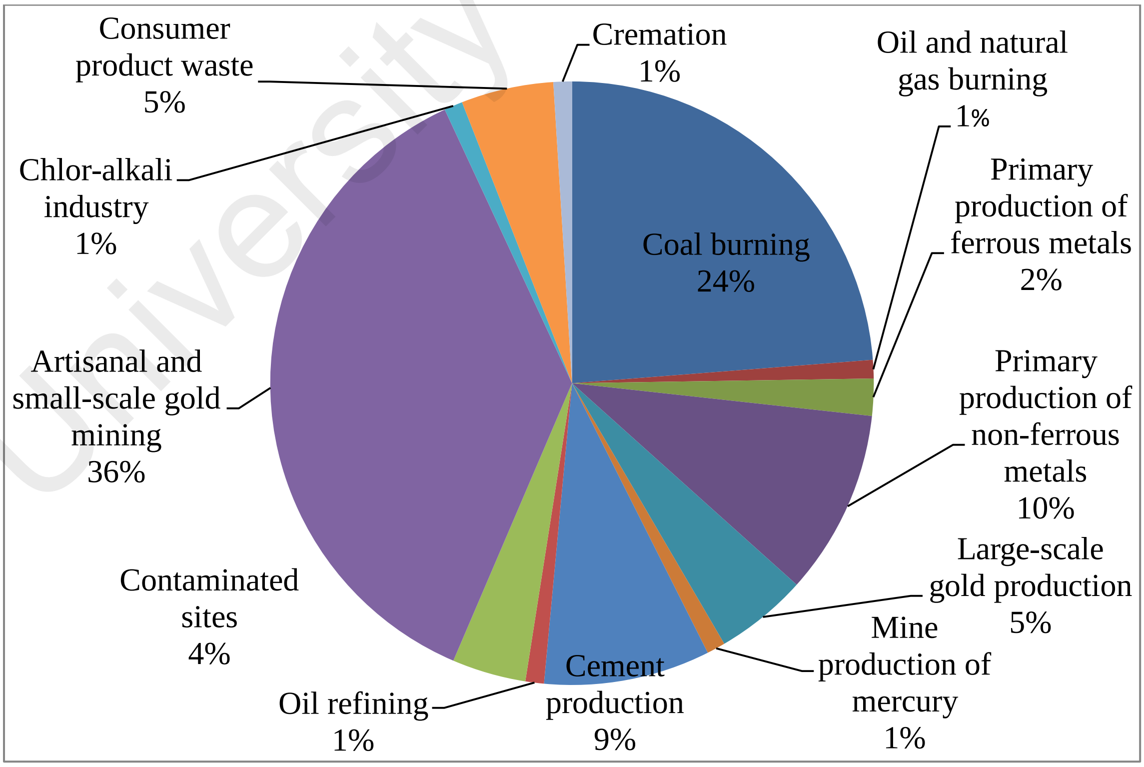

Figure 2.6: Global mercury emissions from anthropogenic sources in 2010 (UNEP, 2013)

2.4.1 Applications of Mercury

Mercury has many specialist uses and applications due to its unique properties (liquid form at STP, high surface tension, high specific gravity, and low electrical resistance). Mercury is often used in electrical equipment and control devices, where the fluidity stability, high density and electrical conductivity are essential. It is still sometimes used in electrical switches as a liquid contact. Other than that, mercury oxide is often used in mercury batteries, which are compact and stable energy sources (Jaishankar et al., 2014).

Another major application of mercury is in thermometers, thanks to its high rate of thermal expansion that is fairly constant over a wide temperature range. Also, due to its high density, mercury is used in barometers and manometers. Thus, pressure is often measured in millimeters of mercury. Furthermore, calomel (mercurous chloride, Hg_2Cl_2) is used as a standard in electrochemical measurements.

In the chemical industry, mercury is mainly used as a catalyst. Previously its major use was as liquid electrolyte for the manufacture of sodium hydroxide and chlorine by electrolysis of brine but is being phased out in favor of safer alternatives (Krishnan & Anirudhan, 2002; Manohar et al., 2002). Mercuric sulfide (vermilion) is a high-grade, bright-red paint pigment, but is very toxic so is now only used with great care (Deonarine & Hsu-Kim, 2009).

Mercury is also often used in agriculture as a fungicide and bactericide. Mercuric chloride (corrosive sublimate, $HgCl_2$) prevents attacks of fungus in seeds and bulbs. It is also used as an insecticide and an ingredient in rat poison (Gochfeld, 2003).

Mercury compounds also have many uses in the pharmaceutical sector. Mercurous chloride (calomel) is still used as an antiseptic. Also, calomel is a good purgative and disinfectant. Other than that, mercuric oxide is often used in skin ointments (Gochfeld, 2003; Tchounwou et al., 2003). In the dental industry, mercury is often used as a component for dental amalgams for making teeth fillings. This is because mercury is good to amalgamate aluminum, zinc and other metals. The amalgam of 70% silver and 30% tin when mixed with mercury formed a pliable material that could be inserted into the tooth and the amalgam expanded as it dried to fill the entire cavity. However this amalgam has been replaced by a similar one made from 60% silver, 27% tin and 13% copper (Clarkson, 2002; Clarkson & Magos, 2006).

Due to the diverse range of applications of mercury throughout the past, mercury pollution has become a serious and enduring threat to the environment. It has affected the organisms along the food chain, including humans. In order to overcome the adverse effects of mercury pollution, policy makers should take advantage of the updated information about the global mercury emissions from time to time to protect human health and the ecosystem from this highly toxic pollutant.

2.4.2 Impacts of Mercury

In this section, the impacts of mercury pollution will be highlighted. Mercury pollution mainly impacts the ecosystem (environment, organisms and humans) and the industry sector. Mercury is highly dangerous to the environment mainly because of its ability to build up in organisms along the food chain. This is particularly true in the case of methylmercury, which is very vulnerable to being absorbed and accumulated along the food chain in comparison to other forms of mercury (Arshadi, 2015; Jaishankar et al., 2014). The absorbtion rate of inorganic mercury is much slower than methylmercury. This build up of methylmercury in organisms will ultimately affect not only animals but also humans. Most vulnerable to methylmercury absorbtion are fish and seafood, due to the increasing mercury pollution in sea water. Methylmercury bind to fish and seafood tissue strongly as the methylmercury are usually covalently bound to protein sulfhydryl groups. Due to the low elimination rate and high consumption rate of methylmercury, mercury concentrations in individuals of a given fish species tend to increase with age. This means that for fish of the same species, older fish usually have higher mercury concentrations in the tissues than younger fish. Thus, organisms at the top levels of the food chain such as humans, seabirds, and seals are particularly prone to the threat of methylmercury (Clarkson & Magos, 2006). Methylmercury is a poison that targets the central nervous system while inorganic mercury usually damages the kidneys. Animals affected by mercury poisoning have shown signs of neurological impairment, such as birds showing signs of difficulty flying and other abnormal behaviours. Besides that, mercury poisoning also affects reproduction because methylmercury can easily cross the placenta barrier and destroy the developing nervous system of the fetus (Clarkson & Magos, 2006; Tchounwou et al., 2003; Zahir et al., 2005).

The symptoms and toxicity of mercury depends on its chemical form, with different symptoms for exposure to elemental mercury, inorganic mercury, or organic mercury compounds. The highly toxic methylmercury greatly affects the nervous system. At the early stage of methylmercury exposure, adults usually show non-specific symptoms such as malaise, paresthesia, and blurred vision. With increased exposure, other signs will appear, such as deafness, dysarthria, coma and finally death. For infants exposed to methylmercury during pregnancy, the symptoms include mental impairment, gross motor, microcephaly and sometimes blindness or deafness. In milder cases of mercury poisoning, the symptoms appear later during the development of the infant as psychomotor and mental impairment or persistent pathological reflexes (Clarkson & Magos, 2006; Gochfeld, 2003; Zahir et al., 2005). The Minamata disease, which is basically due to mercury poisoning, occurred in Minamata, Japan in 1956. Due to this catastrophe, the overall prevalence rate of neurological and mental disorders in the Minamata region was reported to be as high as 59%. While most of the affected adults were suffering from paresthesia, ataxia, tremors, hearing impairment and difficulty in walking, their congenital offspring were also affected, and were very late in reaching developmental milestones (Ekino et al., 2007). Excessive exposure to elemental and inorganic mercury will affect the neurological, renal, respiratory, cardiovascular, immunity, and reproductive systems in humans. Humans are usually exposed to elemental mercury from dental amalgams but exposure at work may exceed this by many times (Clarkson, 2002). As for inorganic mercury, diet is the most important source for the general population. Other than that, skin-lightening creams and soaps may also contain mercury and the use of traditional medicine containing mercury can also lead to exposure to elemental or inorganic mercury (Gochfeld, 2003; Zahir et al., 2005).

Eventhough the effects of mercury pollution towards the environment are a global concern, the effects of mercury emissions on the industry sector should not be ignored. Mercury compounds have long been known as a culprit in destroying the profit margins of some industries. Most susceptible to the effects of mercury compounds is the oil and gas industry because mercury is found in nearly all oil and gas reservoirs. In some crude oils, mercury compounds are found in many forms such as elemental mercury, mercuric chloride, mercuric sulfide, mercuric selenide, dimethylmercury and diethylmercury. Elemental mercury can cause amalgamation, amalgam corrosion, liquid metal embrittlement, and galvanic corrosion of the metal made reactors. Mercury has also been a constant problem for plant maintenance when it concentrates and drops out as liquid in the colder sections of the plant. This has caused sudden heat exchanger failures which resulted in plant shutdowns, repairs, fires, and explosions (Hylander & Goodsite, 2006; Wilhelm & Kirchgessner, 2001). Other than that, mercury also tends to contaminate gas treatment processes such as chloride removal systems, acid gas removal systems and glycol dehydration units. Mercury can also deactivate downstream catalyst and poison catalysts in ethylene, aromatics and olefins manufacture in petrochemical plants. The presence of mercury in feedstock, even at very low concentrations, can result in permanent poisons on precious metals, such as palladium supported on alumina catalyst which is commonly used for selective hydrogenation of acetylenes (Hylander & Goodsite, 2006). Overall, mercury contamination causes catalyst poisoning which will then cause a decrease in production yields and shorten catalyst lifetime. Thus, it is necessary to design an effective mercury removal system to prevent accidents which can lead to economical loss in production plants.

2.4.3 Mercury Remediation

Due to the numerous cases of mercury pollution and the huge threat that it poses, many remediation technologies have been emerging since the past few decades. Different remediation techniques are applied with the different mediums where mercury is found in. Typically, mercury is found in different mediums such as water, air, soil, oil, and gas.

Mercury contaminated soil is usually remediated by excavation and disposal. The soil is removed and disposed in a landfill but it is possible for the mercury to leach back into the environment. The contaminated soil can also be roasted or washed to recover the mercury (Wang et al., 2004; Zornoza et al., 2010). Plants are also used to remediate contaminated soil, where a species of plant life is introduced and cultivated onto the contaminated area. This process is also known as phytoremediation. The cultivated plants will absorb the contaminants through their root system, and then detoxify them after a period of time (Garbisu & Alkorta, 2001). This technique is already being employed to remediate organic contaminants such as trichloroethylene and metals (nickel and lead). However, phytoremediation faces several setbacks in the case of mercury remediation as mercury is toxic to most plants (Patra & Sharma, 2000). This means that most species of plants cannot survive long enough to remediate the mercury contaminants, limiting the choices of plants for phytoremediation. Anyhow, the problem remains because the mercury-saturated plants are now a toxic waste.

Bioremediation, which is the use of microscopic organisms to clean up contamination, has emerged as a promising remediation method for polluted sites. This is due to the discovery of some bacteria strains which are able to convert inorganic and methylmercury to elemental mercury (Wagner-Döbler et al., 2000). The process of bioremediation of waste water is relatively cheap and has been found to effectively remove mercury. However, this method is not suitable for the remediation of wastewater with high concentration of mercury because high mercury concentration can overcome the bacteria’s defense system and kill them. This means that in situ remediation is not suitable and an extensive reactor setup is required (Essa et al., 2002; Sinha & Khare, 2012). Some researchers have suggested the use of genetic engineering to modify the bacteria by adding the polyphosphate kinase (ppk) gene into some bacteria that already contain the mercury transport mer genes but not the reduction enzyme. These bacteria were engineered to replace the merA enzyme, so that when mercury levels were increased tremendously within the bacteria, polyphosphate was synthesized to chelate the mercury and prevented it from interfering with the processes within the cell. This allowed the bacteria to hyperaccumulate mercury without being affected or killed (Ruiz et al., 2011; Sinha et al., 2012; Dash et al., 2014). However, as the bacteria are used in filter systems, this remediation technique faces similar problems as other filters, such as requiring replacement when saturated. Other than that, it is in the opinion of some researchers that bio-accumulating bacteria are not suitable for in situ remediation because they will involve in the local food chain and could increase the bioactivity of the mercury (Wagner-Döbler et al., 2000).

Other than phytoremediation and bioremediation, another method of mercury waste remediation frequently utilized is filtration. Using physical or chemical absorbents to absorb mercury to the filters, these filters will eventually saturate and will then require replacement or regeneration. The most popular mercury sorbent is activated carbon. Activated carbon has proven to be very effective in purifying vapor streams but it is a poor sorbent for aqueous mercury waste (Hu et al., 2009; Rao et al, 2009). Thus, different sorbents are usually used for aqueous mercury waste remediation, usually ion exchange resins with sulfur based group to bind mercury. In this process, mercury ions from dilute solutions are exchanged with ions held by electrostatic forces on the exchange resin. Ion-exchange resin, either synthetic or natural solid resin, has the specific ability to exchange its cations with the metals in the wastewater (Chiarle et al., 2000). Among the many ion exchange resins available, arguably the most effective sorbent is TMR (Total Mercury Removal) which is able to absorb 0.7g of mercury per gram of resin. The resin can be regenerated upon saturation, by treatment with concentrated hydrochloric acid. However, upon treatment with hydrochloric acid, a new batch of toxic waste is created and the disposal of this secondary waste is a problem itself (Podkościelna & Kołodyńska, 2013). Other than that, one of the commonest problems with this process is the presence of organic matter in water supplies. These substances can become irreversibly adsorbed within the anion beads, reducing their exchange capacity and leading to a reduction in treated water quality (Merrifield et al., 2004).

Waste gas that contains mercury is usually treated by passing the gas through a bed of adsorbent. Adsorbents that are commonly used include zeolite, alumina, bentonite, and also activated carbon (Tan et al., 2012). As with any type of adsorbents, the adsorbents used to remove mercury will eventually become saturated and require replacement from time to time.

Another popular method of mercury removal is chemical precipitation. In this method, Hg^{II} is reduced to Hg^0 which is far less soluble, then extracted from the waste stream by sedimentation or filtration. Eventhough chemical precipitation is a well-established technology with ready availability of chemicals and equipment, the resulting metallic mercury still poses a problem as it has to be recovered and the chemicals used in this process itself may be harmful (Matlock et al., 2002).

Without proper effort to remediate and control the mercury emissions which is polluting our environment, this phenomenon will get out of hand and the human population will soon feel its ill effects. Reliable sources continue to report on the increasing worldwide mercury concentrations yet the global community does not seem to be alarmed with this phenomenon and mercury from anthropogenic sources are still increasing year to year. Therefore, environmental standards should be reviewed and existing environmental regulations should be strongly enforced to prevent a major mercury catastrophe.

CHAPTER 3: METHODOLOGY

In this chapter, the procedures used to synthesize the WO_3-loaded TiO_2 nanotubes, the characterization techniques, and the photocatalytic mercury removal performance tests are described in detail. In this research, WO_3-loaded TiO_2 nanotubes were synthesized via single step electrochemical anodization technique. The overview of the research methodology is displayed in Figure 3.1.

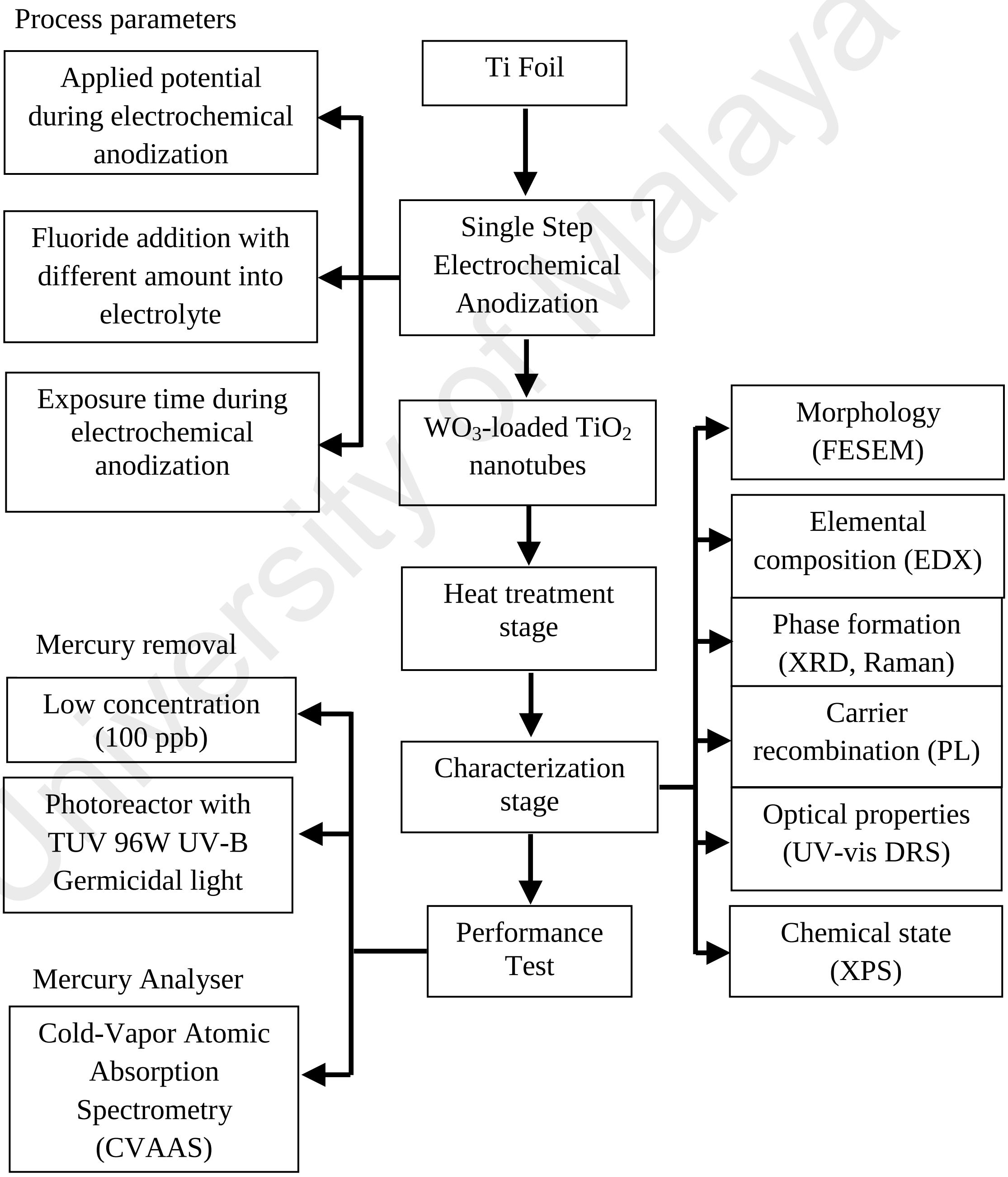

Figure 3.1: Overview of research methodology

3.1 Materials Synthesis

3.1.1 Raw Materials

Chemical and material selections play a critical role in determining the morphology and structure of the WO_3-loaded TiO_2 nanotube arrays and their functional properties. Previous researches have shown that nanotubes with high aspect ratio will exhibit superior properties. In this research, WO_3-loaded TiO_2 nanotube arrays were synthesized by anodic oxidation in fluorinated-organic electrolyte under different conditions. The general information and some properties of the raw materials and chemicals used in this research are detailed in Table 3.1.

Table 3.1: Raw materials and chemicals used for the synthesis of WO_3-loaded TiO_2 nanotube arrays

Material	Function	Manufacturer	Properties
Titanium foil	Substrate/Anode	Sigma Aldrich	Purity: 99.6% Thickness: 0.127 mm
Tungsten foil	Cathode	Sigma Aldrich	Purity: 99.9% Thickness: 0.127 mm
Ethylene glycol	Anodization electrolyte	Friendemann Schmidt	Chemical formula: $C_2H_6O_2$ Purity: >99.5%
Ammonium fluoride	Etching agent	Merck	Chemical formula: NH_4F Purity: ACS reagent, >98%
Hydrogen peroxide	Oxidizing agent	Friendemann Schmidt	Chemical formula: H_2O_2 Purity: 30%
Acetone	Cleaning agent	Friendemann Schmidt	Chemical formula: $(CH_3)_2CO$ Purity: >99.5%

3.1.2 Sample Preparation

3.1.2.1 Foil preparation

The cleanliness and purity of the Ti foil is very important to ensure better architecture of nanotubes growth. Thus, any form of contamination such as finger prints and debris must be removed before the Ti foil is used for anodization. Ti foil that has been cut into desired dimension (5 cm x 1 cm) was immersed in acetone and then introduced to ultrasonic bath cleaning for 15 minutes. Then, the Ti foil was rinsed with deionized (DI) water followed by drying. This procedure will ensure the surface of the Ti foil is thoroughly cleaned which allows the nanotubes to grow perpendicularly on the titanium metal substrate.

3.1.2.2 Electrolyte preparation

Electrolyte composition has significant influence on the morphology of the nanostructures that were formed. The composition of electrolyte will determine whether the film will form compact or porous structure. The electrolyte used in this study consists of ethylene glycol with dissolved NH_4F and H_2O_2. NH_4F and H_2O_2 were added into the ethylene glycol electrolyte and the mixture was stirred by magnetic agitation for 30 minutes to dissolve the mixture homogenously before electrochemical anodization was performed.

3.1.2.3 Anodization procedure

In this electrochemical anodizing cell, the Ti foil is made as the anode by connecting it to the positive terminal of DC power supply (CBS Scientific EPS-200X). The cathode is a W foil and connected to the negative terminal. The Ti foil and W foil were then positioned approximately 2 cm apart and immersed into the prepared electrolyte. The DC power supply was then adjusted to the desired potential and switched on to begin the anodization process. The anodization process was terminated by switching off the DC power supply when the desired exposure time had been reached. Throughout the anodization process, the electrolyte was continuously stirred by magnetic agitation. The set-up of the electrochemical cell is shown in Figure 3.2.

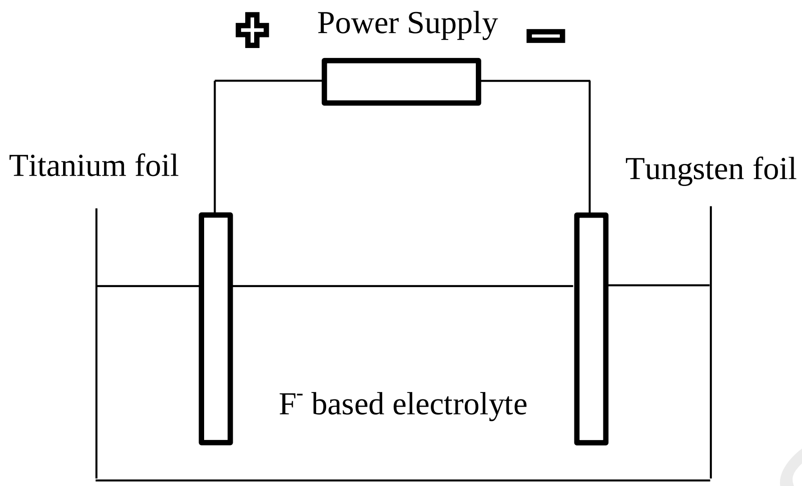

Figure 3.2: Set-up of electrochemical cell with Ti as anode and W as cathode

3.1.2.4 Cleaning TiO_2 nanotubes

After the anodization process, the Ti foil which had formed nanotubes was cleaned with deionized water. This was done by immersing the Ti foil in DI water and ultrasonicated in an ultrasonic bath for 1 minute. This cleaning process will remove the remaining electrolyte on the Ti foil and eliminate the debris and precipitation layers on top of the nanotubes.

3.1.2.5 Annealing process

Annealing is a heat treatment where a material is heated and maintained at a suitable temperature and then cooled down to produce changes in its properties such as strength, hardness, and phase composition. In this research, annealing is used to convert innate amorphous structure of as-anodized nanotube arrays to crystalline phase. This is important because it is well known that the photocatalytic activity of crystalline phase such as anatase is more effective compared to amorphous structure.

There are three stages in the annealing process, which are heating, soaking, and cooling. Annealing was done in air atmosphere. The heating rate used in this research was determined at 10 ℃/min while the soaking temperature was determined at 400 ℃, which is the typical temperature for forming anatase phase. The dwell time was 4 hours, after which the furnace was switched off and the sample was cooled down slowly in the furnace. The example of annealing profile is shown in Figure 3.3.

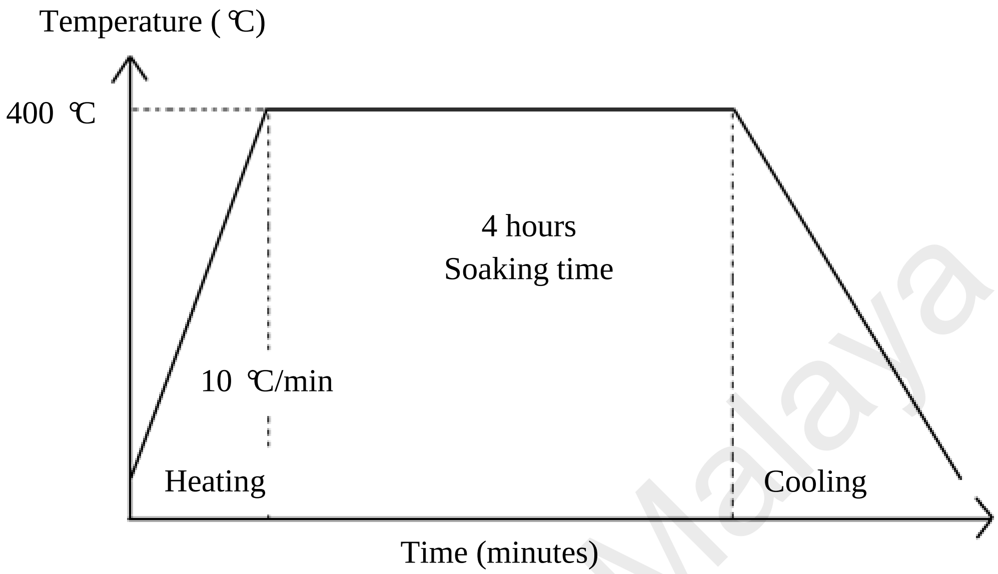

Figure 3.3: Annealing profile of anodized Ti foil

3.2 Characterization Techniques

In this stage, the synthesized WO_3-loaded TiO_2 nanotubes were characterized using various techniques to comprehend the properties of the material. The principles of the characterization techniques and the parameters set to characterize the samples were described and recorded. These characterization techniques include Field Emission Scanning Electron Microscopy (FESEM) for morphological studies, Energy-dispersive X-ray Spectroscopy (EDX) for elemental composition analysis, X- ray diffraction (XRD) and Raman Spectroscopy for phase structure analysis, Photoluminescence Spectroscopy (PL) for carrier recombination analysis, UV-vis Diffuse Reflectance Spectroscopy (UV-vis DRS) for optical properties analysis and also X-ray Photoelectron Spectroscopy (XPS) for chemical state analysis.

3.2.1 Field Emission Scanning Electron Microscope

The field emission scanning electron microscope (FESEM) is a non-destructive technique used to study surface topography, morphology, and composition of solid samples. FESEM is often preferred in place of optical imaging because it provides enhanced depth of field. The working principle of FESEM is based on an electron beam that passes through a vacuum column and focused onto the specimen's surface. The signal that is gathered in a FESEM varies and can include secondary electrons, characteristic x-rays, and back scattered electrons. These signals come not only from the primary electron beam impinging upon the sample, but also from other interactions with the sample near the sample's surface. FESEM images have great depth of field, yielding a characteristic three-dimensional appearance which is useful for understanding the surface structure of a sample. In this research, WO_3-loaded TiO_2 nanotubes were examined using a JEOL JSM 7600-F field emission scanning electron microscope operated at 3 kV and 5 kV and magnifications of 10, 30, 50 and 100 kX were typically used for detailed characterization.

Other than that, the FESEM is also equipped with Energy dispersive X-ray spectrometer (EDX) which is an analytical tool used for elemental content characterization. The working principle of EDX is based on an electron beam which strikes the surface of a conducting sample and causes X-rays to be emitted from that point on the material. The X-rays are generated in a region about two microns in depth, and thus EDX is not a surface science technique. The X-ray which was emitted from the material will strike the detector and generates photoelectrons. The photoelectrons then generate electron-hole pairs which are attracted to opposite ends of the detector with the aid of a strong electric field. Depending on the number of electron-hole pairs created, a current pulse will be generated and an X-ray spectrum can be acquired. This spectrum gives information on the elemental composition of the material under examination.

3.2.2 X-ray Diffraction

X-ray diffraction was used to obtain information about the phase structure of the WO_3-loaded TiO_2 nanotubes. In this research, XRD analysis was conducted using a Bruker D8 Advance diffractometer from 10 to 80 with Cu Kα radiation (α=1.5406 Å).

The basic principle of XRD is based on monochromatic X-ray beam that is directed onto a crystalline material which will get diffracted to produce diffraction patterns. These patterns will be indexed to get information on the phase of the material. By exposing the material to radiation, reflections are recorded by a detector and observed at different angles with respect to the primary beam. Using Braggs law: $n\lambda=2d\sin\theta$, the d-spacings can be calculated and generated in an X-ray scan, which provides a unique fingerprint of the materials present in the sample. By comparing the generated XRD spectrum with reference patterns from the International Centre of Diffraction Data (ICDD) database, the phases of the sample can be evaluated and identified.

3.2.3 Raman Spectroscopy

Raman spectroscopy can be used for sample phase identification by providing information about molecular vibrations. In this technique, the specimen is irradiated with a monochromatic beam and the scattered light is recorded by a detector. The majority of the scattered light is of the same frequency as the excitation source, which is known as elastic scattering. A small amount of the scattered light is shifted in energy from the laser frequency due to interactions with vibrational energies of the molecules in the specimen. The Raman spectrum is then plotted from the intensity of the shifted light versus frequency, which indicates the energy levels of different functional group vibrations. In this research, the crystal structures of the samples were identified by using a Raman spectrometer (Renishaw inVia, United Kingdom) over the range of 100 cm^{-1} to 1000 cm^{-1}, at an excitation wavelength of 532 nm generated by an Ar ion laser.

3.2.4 Photoluminescence Spectroscopy

Photoluminescence spectroscopy is a contactless and non-destructive method of examining the electronic structure and recombination mechanism of materials. Photoluminescence is a process in which a substance absorbs photons and its electrons are excited to a higher energy state then emit photons and return to a lower energy state. The energy of the emitted photons (photoluminescence) relates to the difference in energy levels between the two electron states involved in the transition between the excited state and equilibrium state. In semiconductors, the most common electron states involved in radiative transitions are the conduction and valence bands, and the transition energy is known as the band gap energy. The decrease in energy state to equilibrium energy is known as recombination. The intensity of photoluminescence corresponding to the level of recombination depends on the level of photoexcitation and temperature. In this research, recombination in the samples was characterized using Renishaw inVia (United Kingdom) Raman Microscope with 325 nm wavelength monochromatic beam. The photoluminescence were recorded in the range of 350 nm to 750 nm.

3.2.5 UV-vis Diffuse Reflectance Spectroscopy

UV-vis spectrophotometers were developed to determine the absorption values of liquid samples by measuring the relative change of transmittance of light as it passes through the solution. If the material has electronic energy levels that are separated by energy in the wavelength of light, then it may absorb the light energy to move electrons from the filled energy level (valence band) into this empty level (conduction band), which causes a relative decrease in the amount of light at that particular energy. The spectrophotometer then measures this relative decrease in light transmission or increase in light absorbance. It is then possible to compute the energy band gap value of the material based on the UV-vis spectrum, which shows the interaction of the material with light of various wavelengths resulting from excitation of the electrons from the valence bands into the conduction band.

The absorption and reflectance measurements of solid samples are done using UV-vis diffuse reflectance spectrophotometers. Since light cannot penetrate opaque solid samples, it is reflected on the surface of the samples and DRS measures the relative change in the amount of reflected light off of the surface of the samples. This will produce a DRS spectrum which shows the interaction of the samples with light of various wavelengths resulting from excitation of the electrons from the valence bands into the conduction band, similar to the transmission/absorbance UV-vis spectrum.

In this research, the optical properties of the WO_3-loaded TiO_2 nanotube arrays was investigated using a Shimadzu UV-2700 UV-vis Spectrophotometer and DRS measurements were done in wavelength range of 240 to 800 nm using an integrating sphere.

3.2.6 X-ray Photoelectron Spectroscopy

X-ray photoelectron spectroscopy utilizes photo-ionization and analysis of the surface energy distribution of the emitted photoelectrons of a core electron to investigate chemical and electronic states of the surface. The electron binding energies are dependent on the chemical environment of the atom, making the XPS an important tool to identify the chemical state and oxidation state of an atom. In this research, the investigation of chemical and oxidation states of WO_3-loaded TiO_2 nanotube arrays was performed on a PHI Quantera II scanning X-ray microprobe using an Al cathode (hv = 1486.8 eV) with 100 microns spot size and 280 eV pass energy. The core level spectra of Ti2p, O1s, C1s, and W4d were subsequently recorded through high resolution narrow scans.

3.3 Photocatalytic Mercury Removal Performance Test

The synthesized WO_3-loaded TiO_2 nanotubes were applied in photocatalytic removal of mercury in aqueous system. In this experiment, 10 ppm of mercury chloride ($HgCl_2$) stock solution was prepared with 0.01 g of $HgCl_2$ in 1.00 m^3 of deionized water using a 1.00 L volumetric flask. The working solution was prepared by diluting the stock solution with deionized water. The annealed WO_3-loaded TiO_2 nanotubes were then dipped in 100 ml of 100 ppb $HgCl_2$ solution in quartz glass, as shown in Figure 3.4, and placed in a photoreactor. After leaving the samples in the reactor for 30 minutes in dark environment for dark adsorption, the samples were photoirradiated at room temperature by using TUV 96 W UV-B Germicidal light. 5 ml solution was withdrawn from quartz tubes every 60 minutes. Cold-Vapour Atomic Absorption Spectrometry (CVAAS) was used to measure the concentration of the $HgCl_2$ solutions.

Atomic absorption spectroscopy is a spectroanalytical procedure for the quantitative determination of chemical elements using the absorption of optical radiation (light) by free atoms in the gaseous state. It can be used to determine the concentration of a particular element in a sample. This technique makes use of absorption spectrometry to assess the concentration of an element in a sample. It requires standards with known elemental content to establish the relation between the measured absorbance and the elemental concentration. In this technique, the electrons of the atoms in the atomizer can be promoted to higher orbitals (excited state) for a short period of time (nanoseconds) by absorbing a defined quantity of energy (radiation of a given wavelength). This wavelength is specific to a particular electron transition in a particular element. In general, each wavelength corresponds to only one element, and the width of an absorption line is only of the order of a few picometers (pm), which gives the technique its elemental selectivity. The radiation flux without a sample and with a sample in the atomizer was measured using a detector, and the ratio between the two values (the absorbance) is converted to elemental concentration or mass using the Beer-Lambert Law.

In this research, the CVAAS used to measure the concentration of the samples is a mercury analyser (NIC RA-3120, Japan). The sample was contained in a test tube and reducing reagents ($SnCl_2$ and H_2SO_4) are added to the sample and rapidly aerated. Reduced mercury is transferred via the dehumidifier (trapped all water vapour) and only dry Hg^0 enters the absorption cell to measure at 253.7 nm. Measured Hg^0 is trapped in an exhaust filter before venting back to the ambient as zero-air. The bubbler is then rinsed by flushing with distilled water before commencing to the next sample. The operation of this instrument requires no special-grade bottle gas (just ambient air) as carrier for purge gas even down to 1 ppt detection limit.

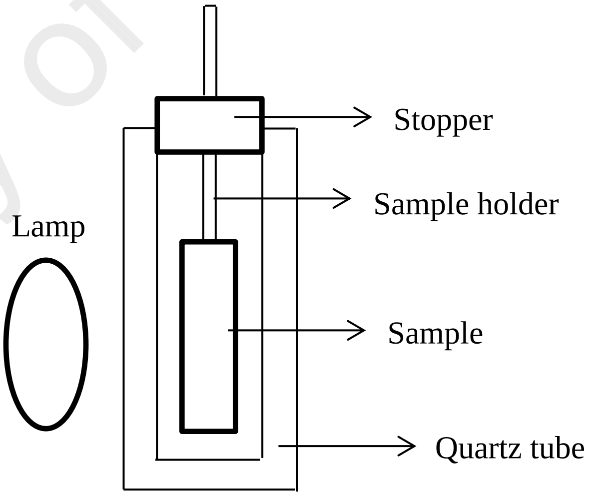

Figure 3.4: Schematic diagram of photoreactor in which mercury removal was performed

CHAPTER 4: RESULTS AND DISCUSSION

In this chapter, the results of the experiment conducted and the discussion on the experiment results are presented. There are two main sections in this chapter. The first section presents the information regarding to the formation of highly ordered WO_3-loaded TiO_2 nanotubes in ethylene glycol electrolyte containing NH_4F. The effect of anodization voltage, fluoride content, and anodization duration on resultant WO_3-loaded TiO_2 nanotubes are evaluated in detail. The second section of this chapter will illustrate the influence of surface morphology, aspect ratio, and geometric surface area factor of the resultant WO_3-loaded TiO_2 nanotubes on the photocatalytic removal of mercury under UV irradiation. The efficiency of mercury removal using WO_3-loaded TiO_2 nanotubes will also be compared to pure TiO_2 nanotubes. Based on our investigations, WO_3-loaded TiO_2 nanotubes showed better photocatalytic mercury removal performance compared to pure TiO_2 nanotubes because the coupling of WO_3 and TiO_2 suppressed the recombination of the photogenerated carriers and increased charge separation of TiO_2.

4.1 Transient and Steady State Current Density Analysis

Figure 4.1 shows the current density curve for a WO_3-loaded TiO_2 nanotubes sample produced at 40 V and anodized for 30 min in electrolyte containing 0.5 g NH_4F. Current density is the measurement of electric current (charge flow in amperes) per unit area of cross section (m^2). The current transients were recorded during anodization of Ti samples. About 5 min after application of the voltage, the measured current density reduced from about 49 mA/cm^2 to around 15 mA/cm^2, point P2 on the plot. The reduced current density resulted from the field-assisted oxidation of the Ti metal surface, which forms a compact oxide layer (Lai & Sreekantan, 2011; Song et al., 2011) H_2O_2 is a powerful oxidant which contributes HO_2^- and H^+ in the electrolyte. HO_2^- plays the role of oxygen provider, which increases the oxidation rate of Ti to form TiO_2. Furthermore, in the presence of electron, HO_2^- may further decompose to form •OH and HO_2• (Equations 4.1 to 4.3), which assisted in the oxidation of Ti as well. The reactions occurred is represented by the equations below:

$H_2O_2 \rightarrow HO_2^- + H^+$ [Equation 4.1]

$H_2O_2 + e^- \rightarrow \bullet OH + OH^-$ [Equation 4.2]

$H_2O_2 + \bullet OH \rightarrow H_2O + HO_2\bullet$ [Equation 4.3]

$Ti \rightarrow Ti^{4+} + 4e^-$ [Equation 4.4]

$Ti^{4+} + 2H_2O \rightarrow TiO_2 + 4H^+$ [Equation 4.5]

Region P2 to P3 represents the field-assisted dissolution of the oxide layer caused by high electric field across the thin layer. The current gradually drops with a corresponding increase in porous structure depth. Fine pits or cracks form on the oxide surfaces which arise from chemical and field-assisted dissolution of the oxide at local points of high energy. The reduced oxide layer thickness at these points decreases the current density (Lai & Sreekantan, 2011; Grimes, 2007). The reaction that occurred is represented by the following equation:

$TiO_2 + 4H^+ + 6F^- \rightarrow [TiF_6]^{2-} + 2H_2O$ [Equation 4.6]

Point P3 shows the transition between the porous and nanotube structures. As further chemical and field-assisted dissolution of the oxide layer occurs, the porous structures transition into nanotube structures and the nanotube array continue to increase in length. Nanotube array length increases to point P4 after which the current is cut off and the reaction is ended.

The following equation represents the formation of WO_3 species for the synthesis of anodic WO_3-loaded TiO_2 nanostructure:

$$W^{6+} + 3H_2O \rightarrow WO_3 + 6H^+ \qquad \text{[Equation 4.7]}$$

The current density curves for experiments conducted with other parameters are not plotted since they follow the same path as the 40 V experiment (within reasonable error). The formation of WO_3-loaded TiO_2 nanotubes is illustrated in Figure 4.2.

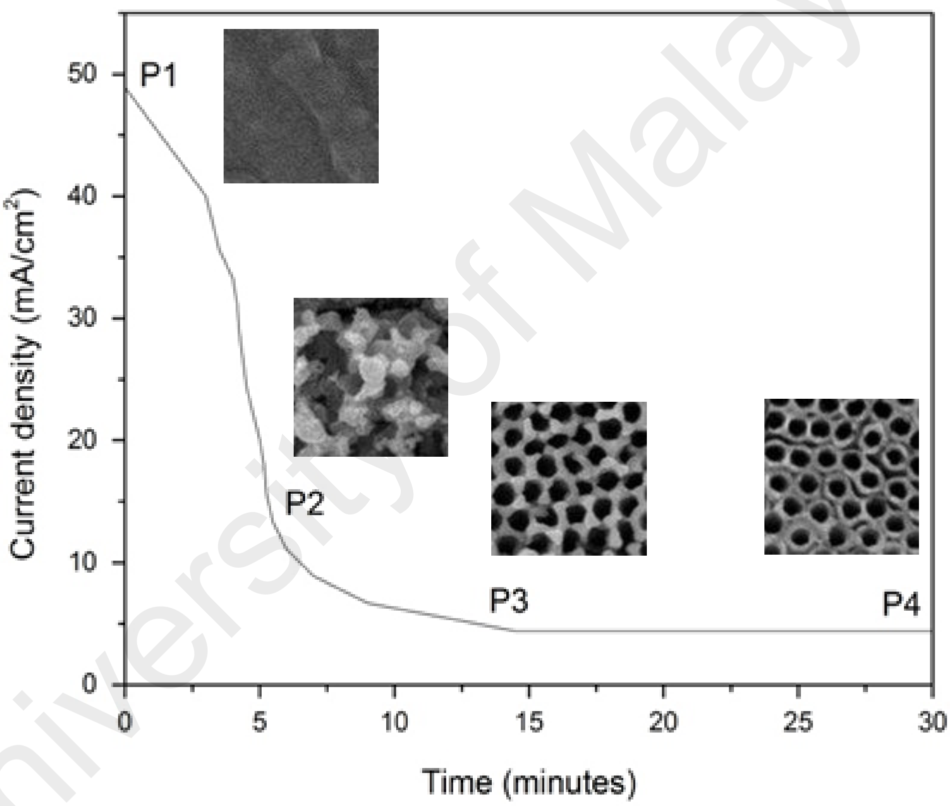

Figure 4.1: Anodization current behavior of WO_3-loaded TiO_2 nanotubes synthesized at 40 V and anodized for 30 min in electrolyte containing 0.5 g NH_4F

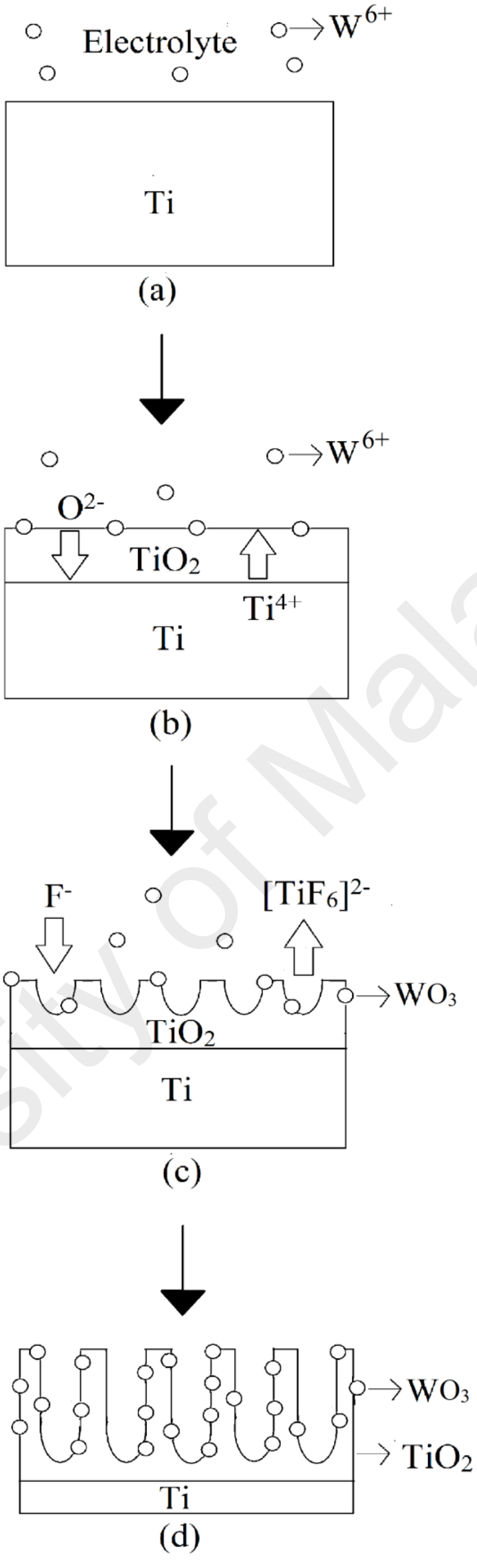

Figure 4.2: Formation of WO_3-loaded TiO_2 nanotubes: (a) Ti foil, (b) oxide layer formation, (c) chemical dissolution of oxide layer and (d) WO_3-loaded TiO_2 nanotubes

4.2 The Effect of Anodization Voltage

The morphology and structure of the nanotubes layer are affected strongly by the electrochemical conditions, especially the anodization voltage, as it is the key factor controlling the tube diameter. Generally, nanotubes growth occurs proportional to the applied potential up to a voltage where dielectric breakdown of the oxide occurs. Tube diameter is affected by voltage but it is not affected by time. Instead, the time of anodization influences the thickness of the nanotube layer. Thus, the influence of anodization voltage on the formation of WO_3-loaded TiO_2 nanotube arrays was investigated in this study with the aim to fabricate nanotubes with optimum length, wall thickness, and pore diameter for better photocatalysis application. The nanotube diameter is expected to increase with increasing voltage due to higher field assisted oxidation rate of Ti metal to form TiO_2 layer and field assisted dissolution rate of Ti metal ions in the electrolyte.

4.2.1 Morphological Studies and Elemental Analysis by FESEM-EDX

An anodization applied voltage controls field-assisted oxidation and field-assisted dissolution during anodization process and, thus, varies the diameter and the length of the anodic WO_3-loaded TiO_2 nanotubes (Lockman et al., 2010). Therefore, the electrochemical anodization was performed in ethylene glycol containing 0.5 wt% NH_4F for 30 minutes. The voltage was varied from 10 V to 40 V.

Figure 4.3 clearly shows that the applied voltage affects the geometric features of the nanotubes on the Ti foils. Anodization voltage of 10 V produced nanotube arrays with smallest average pore diameter of 47 nm and shortest length of approximately 0.9 μm. At anodization voltage of 20 V, nanotube arrays with average pore diameter of 56 nm and length of approximately 1.2 μm were produced. As anodization voltage is increased to 30 V, the average pore diameter and length of the nanotube arrays also increased to

65 nm and 1.4 μm respectively. Anodization voltage of 40 V produced nanotube arrays with the longest tube length of approximately 1.6 μm and largest average pore size of 74 nm. At anodization voltage of 50 V, anodization was done for duration up to ten minutes, after which the sample tends to corrode. This is caused by the high rate of chemical dissolution of Ti and TiO_2 due to etching by fluoride ions, which is greatly enhanced by the presence of H^+ ion. Furthermore, the high voltage will provide higher driving force for ionic species (H^+ and F^-) which significantly increases the chemical dissolution rate of Ti and TiO_2 (Prakasam et al., 2007). The average diameter, length, wall thickness, aspect ratio (AR), and geometric surface area factor (G) of the nanotubes anodized at different applied voltage are summarized in Table 4.1. The aspect ratio and geometric surface area factor were calculated as follows:

$$AR = L/ (D + 2w) \qquad \text{[Equation 4.8]}$$

$$G = [4\pi L\ (D + w)]/ [\sqrt{3}\ (D + 2w)^2] + 1 \qquad \text{[Equation 4.9]}$$

where L = nanotube length in nm; D = pore size; w = wall thickness (Shankar et al., 2007)

The diameter and length of nanotubes were found to increase with anodization voltage up to 40 V because of the high electric field dissolution at the barrier layer of nanotubes (Lai & Sreekantan, 2011). At low potential (10 V), the low field assisted oxidation rate and field-assisted dissolution rate during the anodization process resulted in small diameter of pores. Thus, short and small nanotubular structures were formed. However, at higher potential, these small nanotubular structures were then etched into larger pores due to the higher field assisted oxidation and dissolution rate. Higher voltage will provide higher driving force for ionic species (H^+, F^-, and O^{2-}) to move through the barrier layer at the bottom of the nanotube, which allows for faster movement of the Ti/TiO_2 interface into the Ti metal (Lai & Sreekantan, 2011; Crawford

& Chawla, 2009). Nanotube arrays with longer length will be produced from this improved pore deepening process. Thus, optimization of anodization voltage was 40 V in order to grow the well-aligned one-dimensional WO_3-loaded TiO_2 nanotubes because this voltage produced nanotubes with the highest aspect ratio and geometric surface area factor. This voltage will be used in subsequent sections for WO_3-loaded TiO_2 nanotubes synthesis.

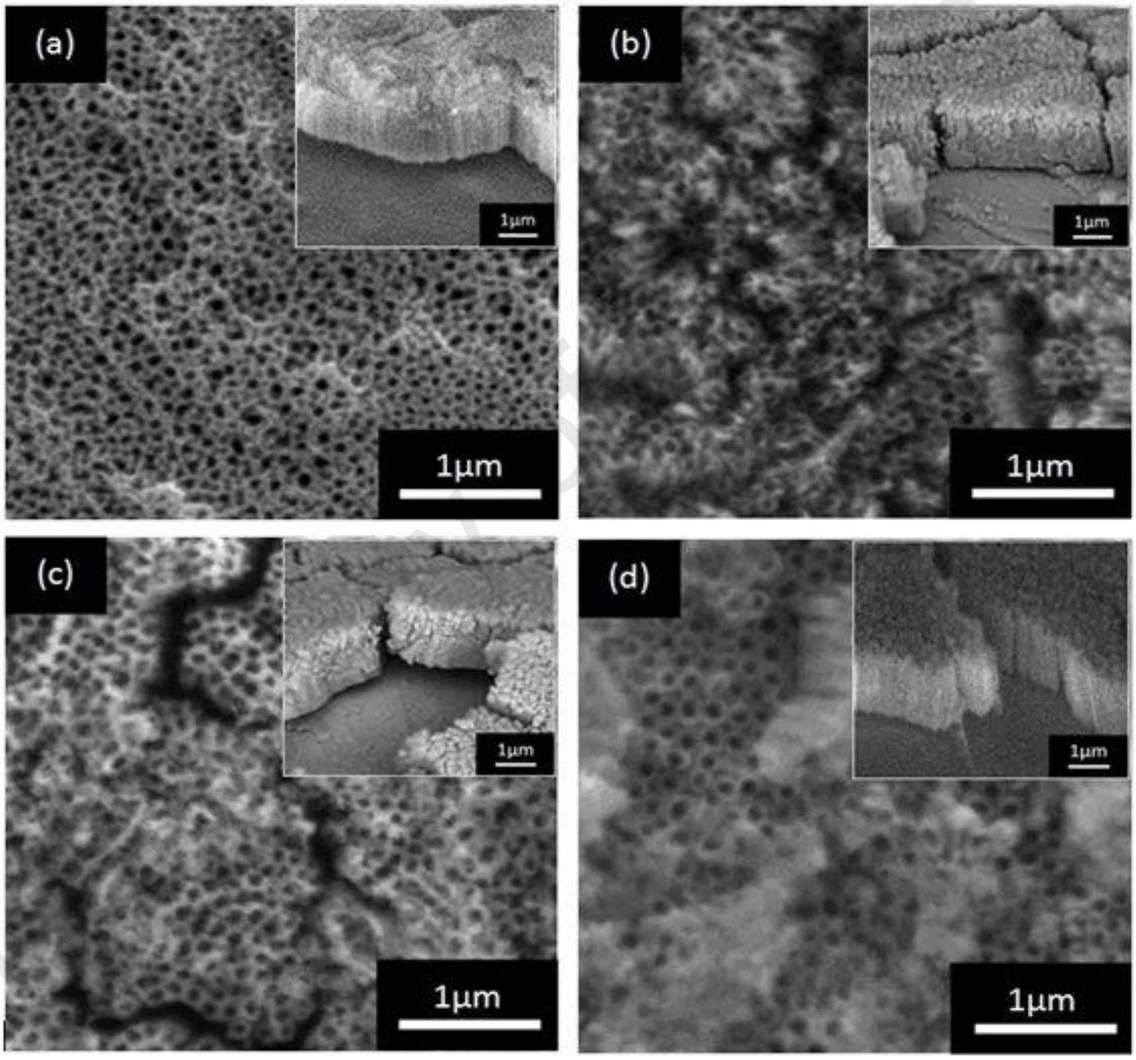

Figure 4.3: FESEM images of WO_3-loaded TiO_2 nanotubes obtained for different anodization voltage at: (a) 10 V; (b) 20 V; (c) 30 V and (d) 40 V in ethylene glycol containing 0.5 wt% NH_4F for 30 minutes. Insets are the side views of the samples

Table 4.1: Pore diameter, length, wall thickness, aspect ratio, and geometric surface area factor of WO_3-loaded TiO_2 nanotubes synthesized with different anodization voltage in ethylene glycol containing 0.5 wt% NH_4F for 30 minutes

Voltage	Diameter (nm)	Length (µm)	Wall thickness (nm)	Aspect Ratio	Geometric surface area factor, G
10V	47 ±3.5	0.9 ±0.1	13 ±1.2	12.33	74.52
20V	56 ±2.7	1.2 ±0.1	15 ±1.3	13.95	84.58
30V	65 ±3.2	1.4 ±0.1	17 ±1.6	14.14	85.98
40V	74 ±4.1	1.6 ±0.2	18 ±0.9	14.55	89.26

The quantitative elemental analysis of WO_3-loaded TiO_2 nanotubes was carried out by cross sectional FESEM-EDAX to confirm the presence of W throughout the length of the nanotubes and the average elemental compositions (at%) were obtained by taking eight spots along the nanotubes. The percentage of each element is shown in Table 4.2. The WO_3-loaded TiO_2 nanotubes show the presence of Ti, O, W and C elements. The presence of C species is attributed to the ethylene glycol electrolyte which is an organic electrolyte and can contribute to carbon doping onto TiO_2 nanotubes (Lai & Sreekantan, 2013b). The presence of W within the nanotube arrays was found to increase with anodization voltage. This is because increasing voltage will increase the strength of electric field in the electrolyte solution, thereby increasing the mobility and rate of migration of W^{6+} ions towards the titanium foil (Issaq et al., 1991). Therefore, at higher anodization voltage, more W will be incorporated into the TiO_2 nanotubes.

Table 4.2: Energy dispersive X-ray elemental analysis of WO_3-loaded TiO_2 nanotubes synthesized with different anodization voltage in ethylene glycol containing 0.5 wt% NH_4F for 30 minutes

Voltage	Atomic %			
	Ti	O	W	C
10V	43.81	51.79	1.06	3.34
20V	48.16	46.95	1.36	3.53
30V	59.22	31.83	2.01	6.94
40V	47.38	44.11	3.29	5.22

4.2.2 Phase Structure Analysis by XRD

Figure 4.4 is an XRD profile of the WO_3-loaded TiO_2 nanotubes formed at different anodization voltage from 10 V to 40 V after annealing at 400 ℃ in air atmosphere for 4 h. The result shows the presence of TiO_2 with anatase phase [JCPDS No. 21-1272]. The diffraction peaks at 25.37°, 38.67°, 48.21°, and 54.10° are corresponding to (101), (112), (200), and (105) crystal planes for the anatase phase, respectively. Additionally, for the sample synthesized at 40 V, small additional peaks at 23.62° and 29.16° corresponds with the (020) and (120) crystal planes of the monoclinic WO_3 phase.

The intensity of the (101) peak at 25.37° increased with increasing anodization voltage, indicating the increased crystallinity of anatase phase. This increase in anatase intensity is due to more growth of TiO_2 nanotubes as voltage is further increased. Furthermore, TiO_2 layer formed at higher voltages are thicker and denser, resulting in higher anatase intensity (Park et al., 2006). However, the XRD patterns did not show any obvious WO_3 phase for samples synthesized at 10 V, 20 V and 30 V. A possible explanation would be that the XRD analysis was not sensitive enough to detect very low WO_3 content (<3 at% from EDX analysis) within the TiO_2 lattice due to the nearly similar ionic radius of W^{6+} and Ti^{4+} (Lai et al., 2012; Leghari et al., 2011).

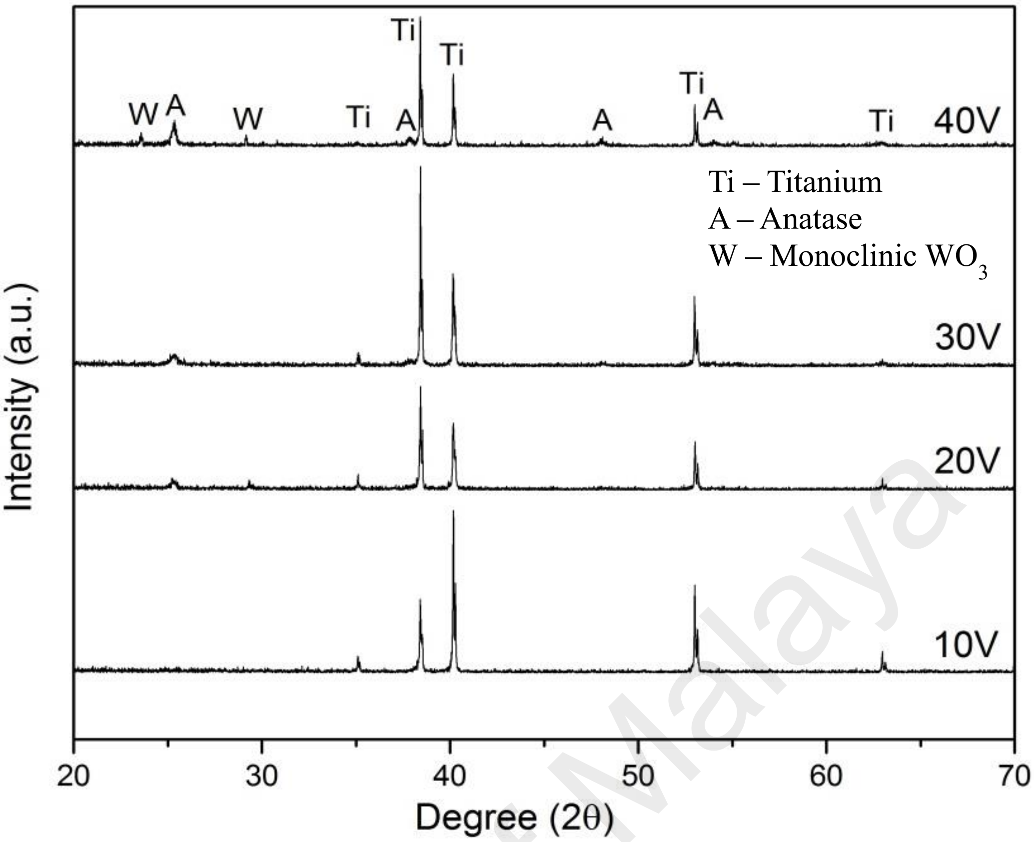

Figure 4.4: X-ray diffraction patterns of WO_3-loaded TiO_2 nanotubes produced at different anodization voltage in ethylene glycol containing 0.5 wt% NH_4F for 30 minutes

4.2.3 Chemical Structure Analysis by Raman Spectroscopy

Raman analysis was conducted to detect the presence of WO_3 and to confirm the XRD inferences of WO_3-loaded TiO_2 nanotubes. Figure 4.5 is the Raman spectrums of the WO_3-loaded TiO_2 nanotubes formed at different anodization voltage which shows five characteristic modes at 145, 198, 396, 518, and 639 cm^{-1}. The mode at 145 cm^{-1} is strong and assigned as the E_g phonon of the anatase structure and B_{1g} phonon of the rutile structure. The latter four modes are assigned as E_g, B_{1g}, B_{1g}, and E_g modes of the anatase phase, respectively. The positions and intensities of the five Raman active modes correspond well with the anatase phase of TiO_2 (Song et al., 2007). The Raman spectrums show increasing intensity of peaks from 10 V to 40 V. Higher intensity of peaks corresponds to higher crystallinity. The increase in anatase intensity from 10 V to 40 V is due to more growth of TiO_2 nanotubes as voltage is increased. Furthermore,

TiO_2 layer formed at higher voltages are thicker and denser, resulting in higher anatase intensity (Park et al., 2004). However, Raman bands for WO_3 was not detected because typical characteristic modes for WO_3 are similar to those for anatase (e.g., 330, 641, and 714 cm^{-1}) and were overlapped by the strong and broad bands for the anatase phase (Lai & Sreekantan, 2013; Picquart et al., 2000).

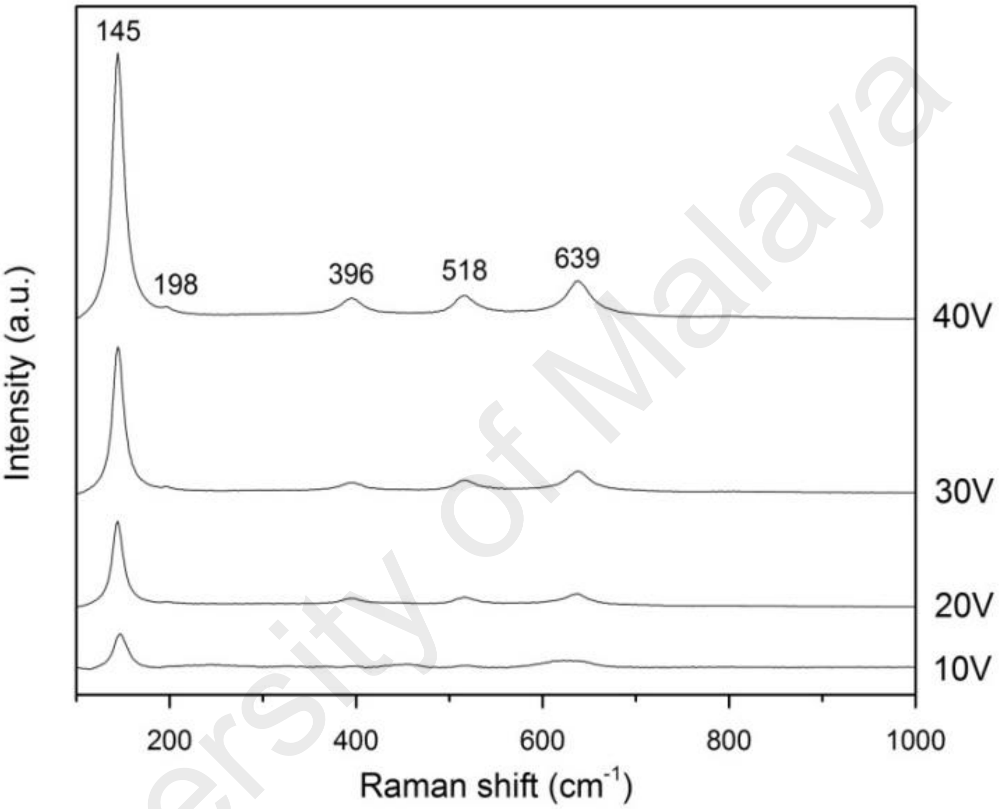

Figure 4.5: Raman spectrum of WO_3-loaded TiO_2 nanotubes produced at different anodization voltage in ethylene glycol containing 0.5 wt% NH_4F for 30 minutes

4.3 The Effect of Fluoride Ion Content

The etching power of F^- ions plays an important role in chemical etching and dissolution of TiO_2 layer to form porous structure during anodization process and, thus, varies the diameter and the length of the anodic WO_3-loaded TiO_2 nanotubes (Acevedo-Peña et al., 2013; Cipriano et al., 2014; Chen & Hsieh, 2010). Therefore, the electrochemical anodization was performed at 40 V for 60 minutes. The fluoride ion content in ethylene glycol was varied from 0 to 0.5 wt%.

4.3.1 Morphological Studies and Elemental Analysis by FESEM-EDX

Figure 4.6 clearly shows that the fluoride ion content in ethylene glycol affects the geometric features of the anodic WO_3-loaded TiO_2 nanotubes. Without any fluoride content, no nanostructures were produced and only an oxide layer of TiO_2 was observed. The reason might be attributed to the absence of F^- ionic species during the electrochemical anodization stage. The sample prepared in ethylene glycol containing 0.1 wt% NH_4F showed irregular features and small oxide pits. The inadequate F^- levels probably caused incomplete chemical dissolution and oxidation at the interface between Ti and the barrier layer. For the 0.3 wt% NH_4F content, a hollow cylindrical oxide was observed, which indicates that the amount of F^- present in the ethylene glycol was sufficient to increase the chemical dissolution. This led to further acidification to develop a nanotubular structure with pore diameter of approximately 65 nm, length of 1.8 µm, and wall thickness of 24 nm. When fluoride ion content was increased to 0.5 wt%, pore diameter increased to approximately 80 nm but the length and wall thickness decreased to approximately 1.5 µm and 17 nm respectively due to increased chemical dissolution of oxide layer. The average diameter, length, wall thickness, aspect ratio (AR), and geometric surface area factor (G) of the nanotubes anodized with varying fluoride ion content are summarized in Table 4.3. Optimization of fluoride ion content in order to grow well-aligned WO_3-loaded TiO_2 nanotubes was identified to be 0.3 wt% for 60 minutes anodization duration at potential of 40 V because this fluoride ion content produced nanotubes with the highest aspect ratio and geometric surface area factor. This fluoride ion content will be used in subsequent sections for WO_3-loaded TiO_2 nanotubes synthesis.

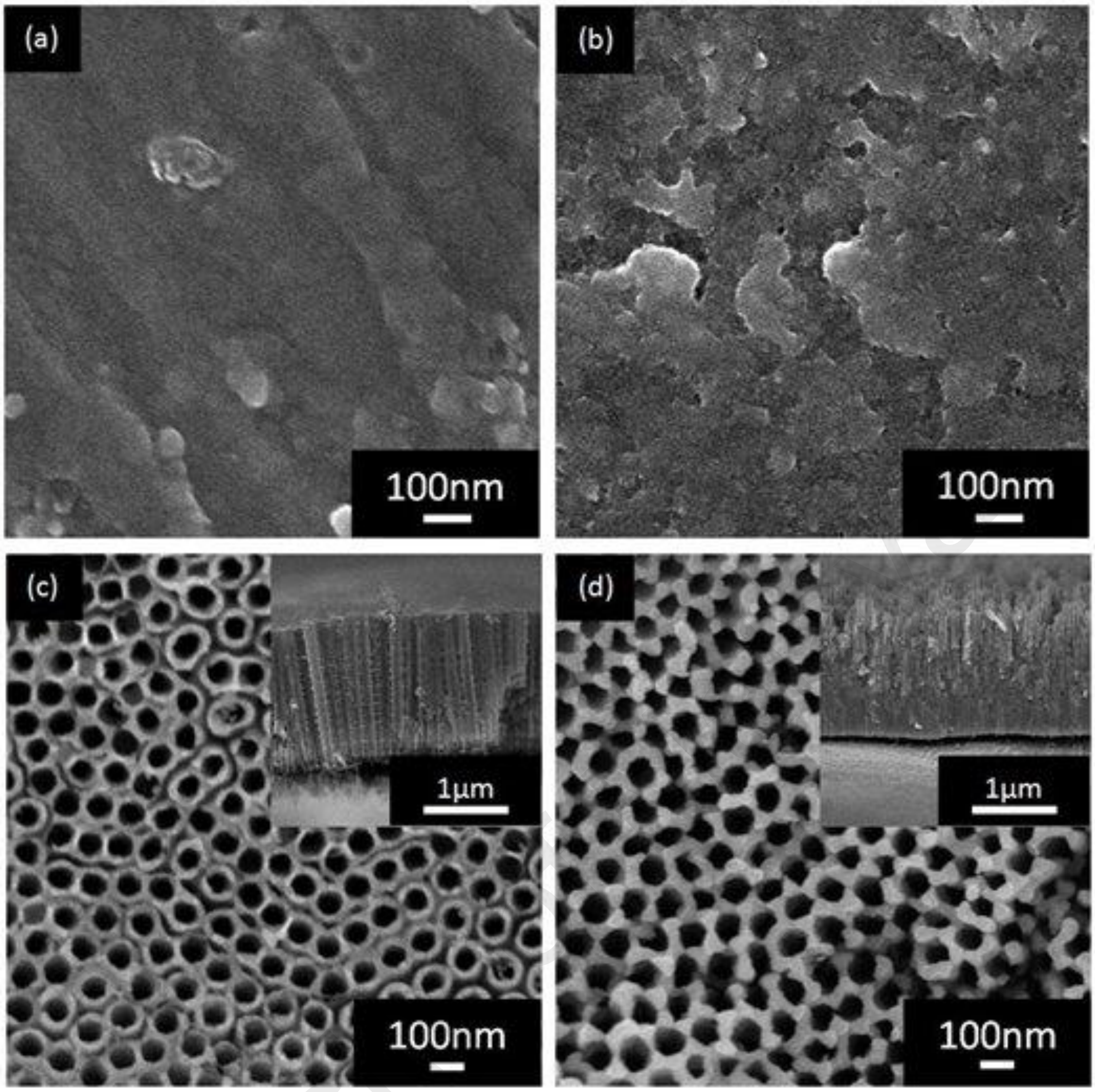

Figure 4.6: FESEM images of WO_3-loaded TiO_2 nanotubes obtained with varying fluoride ion content: (a) 0 wt%, (b) 0.1 wt%, (c) 0.3 wt% and (d) 0.5 wt% at 40 V for 60 minutes. Insets are the side views of the samples

Table 4.3: Pore's diameter, length, wall thickness, aspect ratio, and geometric surface area factor of WO_3-loaded TiO_2 nanotubes synthesized with varying fluoride ion content at 40 V for 60 minutes

NH_4F content	**Diameter (nm)**	**Length (µm)**	**Wall thickness (nm)**	**Aspect Ratio**	**Geometric surface area factor, G**
0 wt%	-	-	-	-	-
0.1 wt%	-	-	-	-	-
0.3 wt%	65 ±2.8	1.8 ±0.3	24 ±2.1	15.9	92.0
0.5 wt%	80 ±6.1	1.5 ±0.2	17 ±1.5	13.2	82.2

The percentage of each element is shown in Table 4.4. The WO_3-loaded TiO_2 nanotubes show the presence of Ti, O, W and C elements. The presence of C species is attributed to the ethylene glycol electrolyte which is an organic electrolyte and can contribute to carbon doping onto TiO_2 nanotubes (Lai & Sreekantan, 2013b). The presence of W within the nanotube arrays was also found to increase with increasing fluoride ion content. This is because increasing fluoride ion content will increase the chemical dissolution rate of W in the electrolyte solution due to the high etching power of F^- ions, thereby increasing amount of W^{6+} ions which migrate towards the titanium foil (Lai, 2014). Therefore, with higher fluoride ion content, more W will be incorporated into the TiO_2 nanotubes.

Table 4.4: Energy dispersive X-ray elemental analysis of WO_3-loaded TiO_2 nanotubes synthesized with varying fluoride ion content at 40 V for 60 minutes

NH_4F content	Atomic %			
	Ti	O	W	C
0 wt%	85.49	7.78	0.22	6.51
0.1 wt%	42.17	51.80	1.50	4.53
0.3 wt%	26.97	65.43	2.36	5.24
0.5 wt%	34.28	58.80	2.90	4.02

4.3.2 Phase Structure Analysis by XRD

Figure 4.7 shows the XRD profile of the WO_3-loaded TiO_2 nanotubes formed using different fluoride ion content from 0 to 0.5 wt% after annealing at 400 ˚C in air atmosphere for 4 hours, which is the typical temperature and time for heat treatment to transform the amorphous structure of TiO_2 into the crystalline anatase phase. The XRD spectrum indicates the presence of anatase phase of TiO_2 [JCPDS No 21-1272]. The diffraction peaks at 25.37 °, 38.67 °, 48.21 ° and 54.10 ° are corresponding to (101), (112), (200) and (105) crystal planes for the anatase phase, respectively. Furthermore, small additional peaks at 23.62 ° and 29.16 ° corresponds with the (020) and (120) crystal planes of the monoclinic WO_3 phase.

We observed that the peaks corresponding to anatase phase were most intense for the sample produced with 0.3 wt% NH_4F followed by 0.5 wt% NH_4F and 0.1 wt% NH_4F. Anatase peaks were not detected for the sample produced with 0 wt% NH_4F. This corresponds with the increased growth of TiO_2 nanotubes which can be explained with the faster movement of the Ti/TiO_2 interface into the Ti metal due to higher content of ionic species which move through the barrier layer at the bottom of the nanotube. The improved pore deepening process results in longer nanotube length, which explains the increasing anatase peaks intensity. When fluoride ion content was further increased to 0.5 wt% NH_4F, anatase peaks intensity decreased slightly due to excessive chemical etching of oxide layer during the chemical dissolution reactions which caused a decrease in nanotube length. However, only the XRD pattern of sample produced with 0.3 and 0.5 wt% NH_4F showed obvious WO_3 phase. A possible explanation would be that the XRD analysis was not sensitive enough to detect very low WO_3 content within the TiO_2 lattice of the samples produced using lower fluoride ion content due to the nearly similar ionic radius of W^{6+} and Ti^{4+} (Lai et al., 2012; Leghari et al., 2011).

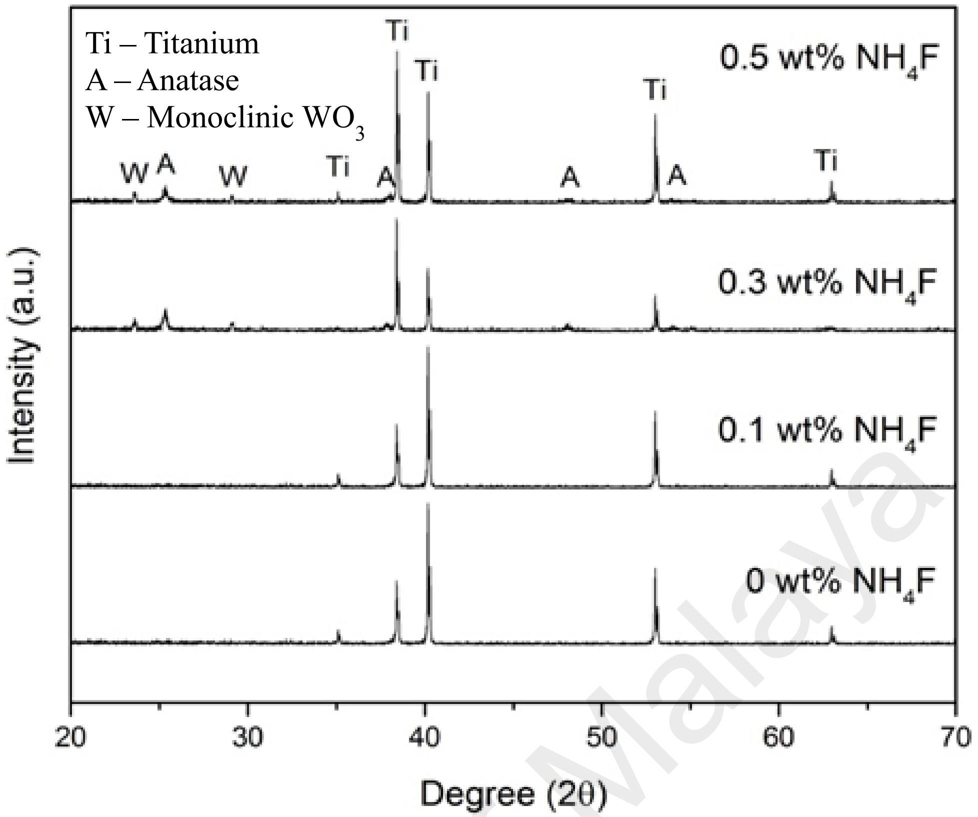

Figure 4.7: X-ray diffraction patterns of WO_3-loaded TiO_2 nanotubes produced with different fluoride ion content at 40 V for 60 minutes

4.3.3 Chemical Structure Analysis by Raman Spectroscopy

Figure 4.8 shows the Raman spectrum of anodic WO_3-loaded TiO_2 nanotubes formed using different fluoride ion content and there are five characteristic modes observed at 145, 198, 396, 518, and 639 cm^{-1}. The mode at 145 cm^{-1} is strong and assigned as the E_g phonon of the anatase structure and B_{1g} phonon of the rutile structure. The latter four modes are assigned as E_g, B_{1g}, B_{1g}, and E_g modes of the anatase phase, respectively. The positions and intensities of the five Raman active modes correspond well with the anatase phase of TiO_2. The lower intensity of anatase peaks for the 0 wt% and 0.1 wt% NH_4F sample corresponds with the short and small nanotubes produced. The sample produced with 0.3 wt% NH_4F showed the highest intensity of anatase peaks because the TiO_2 layer formed is denser and thicker. However, when fluoride ion content is increased to 0.5 wt%, the intensity of anatase peaks decreased. This showed that more oxide layer had been dissolved due to higher chemical dissolution rate, leading to thinner TiO_2 layer. Raman bands for WO_3 was not detected because typical characteristic modes for WO_3 are similar to those for anatase (e.g., 330, 641, and 714 cm^{-1}) and were overlapped by the strong and broad bands for the anatase phase (Lai & Sreekantan, 2013; Picquart et al., 2000).

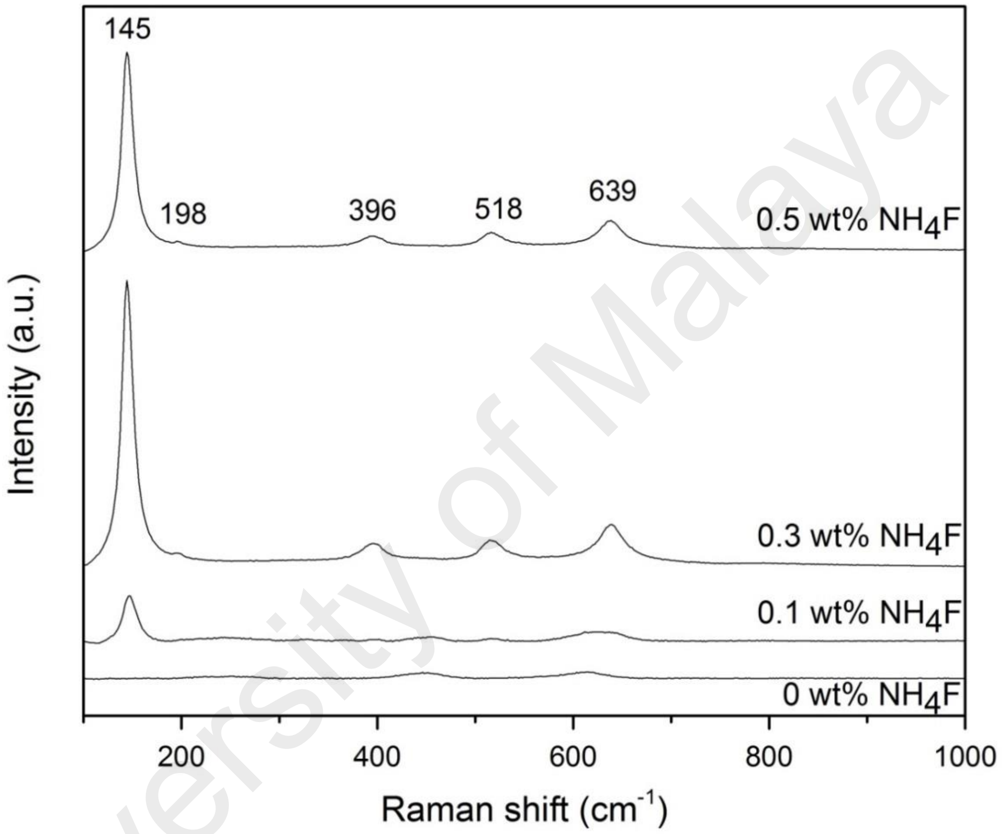

Figure 4.8: Raman spectrum of WO_3-loaded TiO_2 nanotubes produced with different fluoride ion content at 40 V for 60 minutes

4.4 The Effect of Anodization Duration

Anodization duration greatly affects the diameter and the length of the anodic WO_3-loaded TiO_2 nanotubes because the exposure time determines the amount of chemical etching and dissolution of TiO_2 layer to form porous structure during anodization process. Therefore, the electrochemical anodization was performed in ethylene glycol containing 0.3 wt% NH_4F at 40 V. The anodization duration was varied from 15 to 120 minutes.

4.4.1 Morphological Studies and Elemental Analysis by FESEM-EDX

Figure 4.9 clearly shows that the anodization duration affects the geometric features of the anodic WO_3-loaded TiO_2 nanotubes. At anodization duration of 15 minutes, random small oxide pits started to form on the Ti surface which arises from chemical and field-assisted dissolution of the oxide at local points of high energy. From the FESEM micrograph, it is observed that the porous oxide layer that formed was approximately 0.9 μm thick. When anodization duration was increased to 30 minutes, these random small oxide pits turned into larger pores structure due to further field-assisted dissolution of oxide layer, which eventually interconnected to form a uniform nanotubular structure with tube length of approximately 1.6 μm and average pore size of 50 nm. When anodization duration is further increased to 60, 90 and 120 minutes, the nanotubes produced has increasing length, which are approximately 1.8 μm, 5.2 μm and 6.1 μm respectively. The pore diameter of the nanotubes also increased, where the 60 minutes sample had average pore diameter of 65 nm and both the 90 and 120 minutes samples had average pore diameter of 91 nm. The average diameter, length, wall thickness, aspect ratio (AR), and geometric surface area factor (G) of the nanotubes anodized at different anodization duration are summarized in Table 4.5. The sample synthesized at 120 minutes is the best sample because it has the highest aspect ratio and geometric surface area factor.

The length and pore diameter of the nanotubes were found to be increased with increasing anodization duration due to the continuous field assisted oxidation and dissolution as well as chemical dissolution of the oxide layer, which causes the nanotube array to continue to increase in length with longer anodization times.

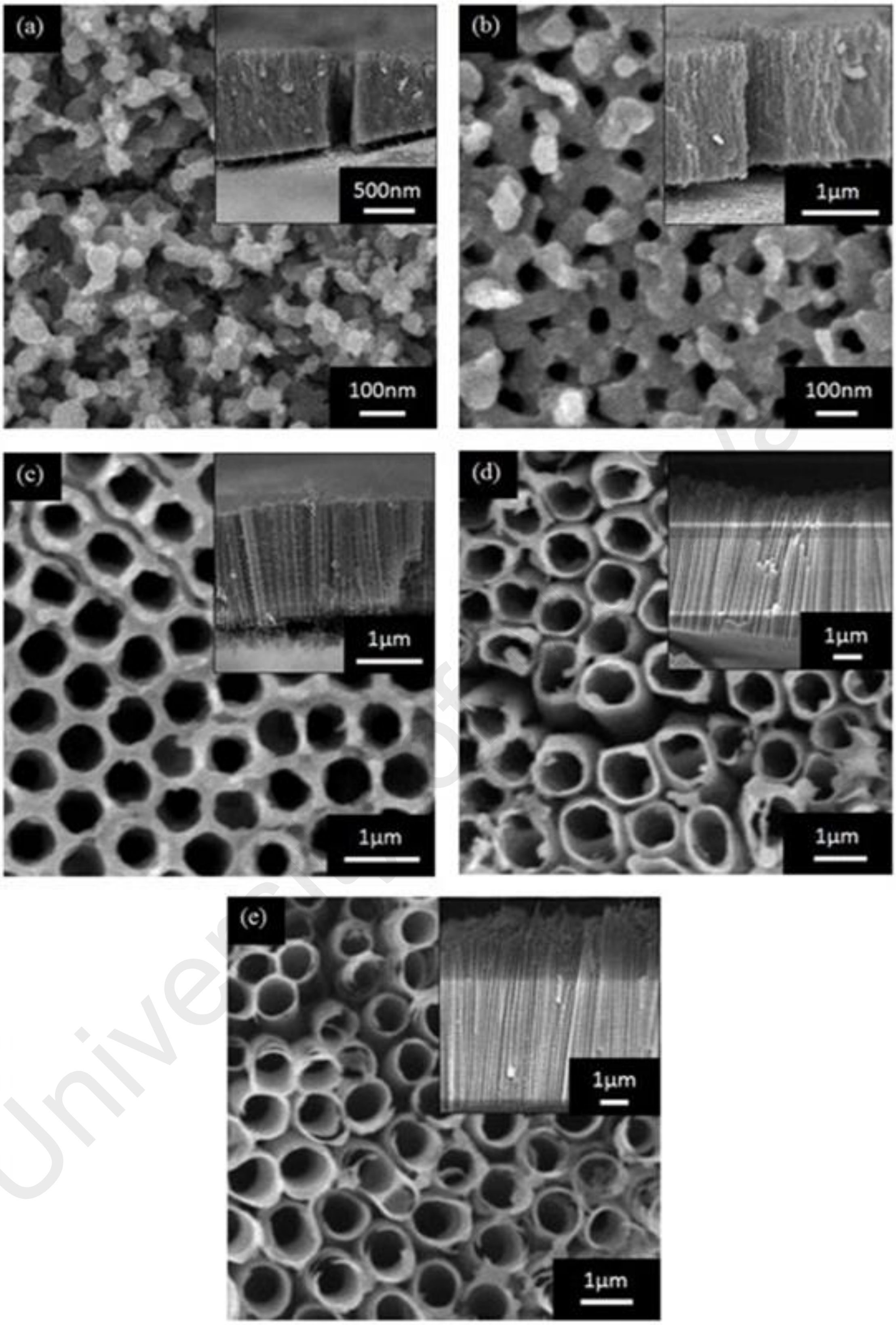

Figure 4.9: FESEM images of WO_3-loaded TiO_2 nanotubes obtained with varying anodization duration: (a) 15 min, (b) 30 min, (c) 60 min, (d) 90 min, and (e) 120 min in ethylene glycol containing 0.3 wt% NH_4F at 40 V. Insets are the side views of the samples

Table 4.5: Pore's diameter, length, wall thickness, aspect ratio, and geometric surface area factor of WO_3-loaded TiO_2 nanotubes obtained with varying anodization duration in ethylene glycol containing 0.3 wt% NH_4F at 40 V

Anodization Duration	Diameter (nm)	Length (µm)	Wall thickness (nm)	Aspect Ratio	Geometric surface area factor, G
15 min	-	0.9 ±0.1	-	-	-
30 min	50 ±3.5	1.6 ±0.1	40 ±1.5	12.31	62.82
60 min	65 ±2.8	1.8 ±0.3	24 ±2.1	15.93	92.02
90 min	91 ±8.5	5.2 ±0.2	15 ±1.6	42.98	274.14
120 min	91 ±7.5	6.1 ±0.2	12 ±0.8	53.04	345.68

The percentage of each element is shown in Table 4.6. The WO_3-loaded TiO_2 nanotubes show the presence of Ti, O, W and C elements. The presence of C species is attributed to the ethylene glycol electrolyte which is an organic electrolyte and can contribute to carbon doping onto TiO_2 nanotubes (Lai & Sreekantan, 2013b). The presence of W within the nanotube arrays was also found to increase with increasing anodization duration simply because more W^{6+} ions can migrate towards the titanium foil with longer anodization times.

Table 4.6: Energy dispersive X-ray elemental analysis of WO_3-loaded TiO_2 nanotubes obtained with varying anodization duration in ethylene glycol containing 0.3 wt% NH_4F at 40 V

Anodization duration	Atomic %			
	Ti	O	W	C
15 min	33.88	57.31	1.14	7.67
30 min	29.22	62.39	2.20	6.19
60 min	27.89	63.35	2.72	6.04
90 min	27.80	61.34	3.26	7.60
120 min	29.82	62.36	3.50	4.32

4.4.2 Phase Structure Analysis by XRD

Figure 4.10 is an XRD profile of the WO_3-loaded TiO_2 nanotubes formed at different anodization duration from 15 to 120 minutes after annealing at 400 °C in air atmosphere for 4 h. The result shows the presence of TiO_2 with anatase phase [JCPDS No. 21-1272]. The diffraction peaks at 25.37 °, 38.67 °, 48.21 °, and 54.10 ° are corresponding to (101), (112), (200), and (105) crystal planes for the anatase phase, respectively. Additionally, except for the sample synthesized at 15 minutes, small additional peaks at 23.62 ° and 29.16 ° corresponds with the (020) and (120) crystal planes of the monoclinic WO_3 phase.

The intensity of the (101) peak at 25.37 ° increased with increasing anodization duration, indicating the increased crystallinity of anatase phase. This increase in anatase intensity is due to more growth of TiO_2 nanotubes as anodization duration increased. Furthermore, TiO_2 layer formed at longer durations are thicker and denser, resulting in higher anatase intensity. However, the XRD patterns did not show any obvious WO_3 phase for samples synthesized at 15 minutes because of the insufficient amount of WO_3 loading onto the TiO_2 nanostructures due to short anodization duration. A possible explanation would be that the XRD analysis was not sensitive enough to detect very low WO_3 content (<3 at% from EDX analysis) within the TiO_2 lattice due to the nearly similar ionic radius of W^{6+} and Ti^{4+} (Lai et al., 2012; Leghari et al., 2011).

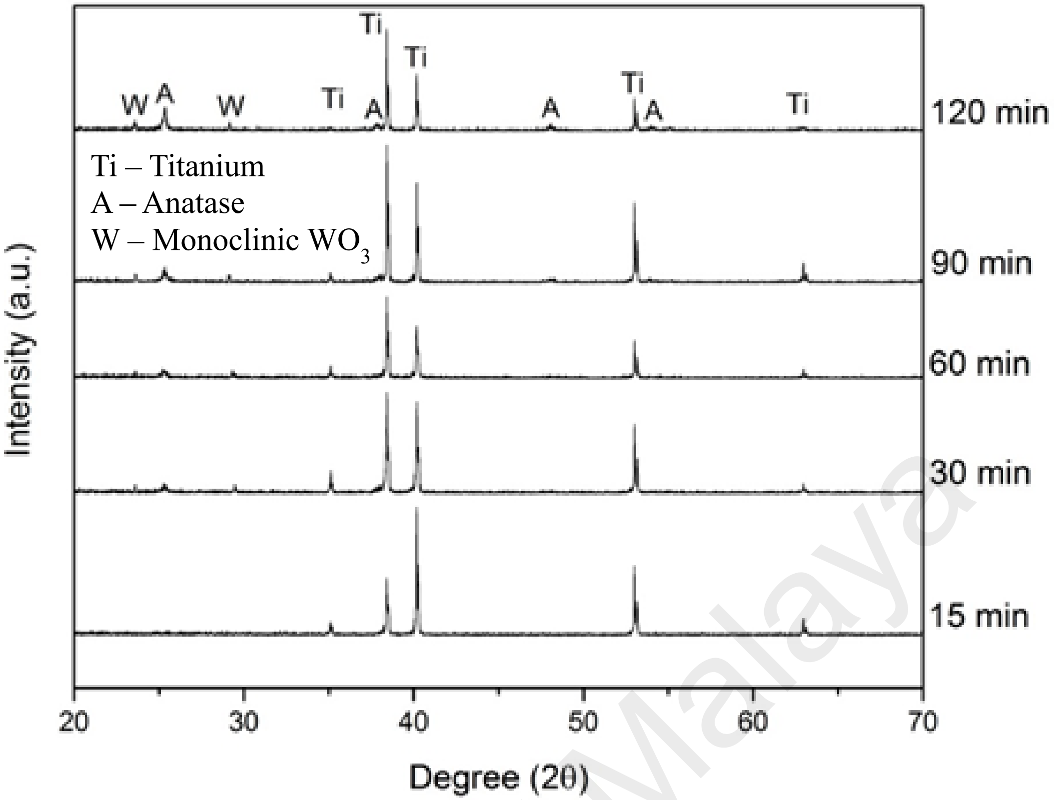

Figure 4.10: X-ray diffraction patterns of WO_3-loaded TiO_2 nanotubes produced at different anodization duration in ethylene glycol containing 0.3 wt% NH_4F at 40 V

4.4.3 Chemical Structure Analysis by Raman Spectroscopy

Figure 4.11 shows the Raman spectrum of anodic WO_3-loaded TiO_2 nanotubes formed at different anodization duration and there are five characteristic modes observed at 145, 198, 396, 518, and 639 cm^{-1}. The mode at 145 cm^{-1} is strong and assigned as the E_g phonon of the anatase structure and B_{1g} phonon of the rutile structure. The latter four modes are assigned as E_g, B_{1g}, B_{1g}, and E_g modes of the anatase phase, respectively. The positions and intensities of the five Raman active modes correspond well with the anatase phase of TiO_2. The lower intensity of anatase peaks for sample produced at 15 minutes corresponds with the short and small nanotubes produced. The sample produced at 120 minutes showed the highest intensity of anatase peaks because the TiO_2 layer formed is denser and thicker. Higher intensity of peaks corresponds to higher crystallinity. The increase in anatase intensity from 15 to 120 minutes is due to more growth of TiO_2 nanotubes as anodization duration is increased. Furthermore, TiO_2 layer formed at longer anodization duration are thicker and denser, resulting in higher anatase intensity. However, Raman bands for WO_3 was not detected because typical characteristic modes for WO_3 are similar to those for anatase (e.g., 330, 641, and 714 cm^{-1}) and were overlapped by the strong and broad bands for the anatase phase (Lai & Sreekantan, 2013b; Picquart et al., 2000).

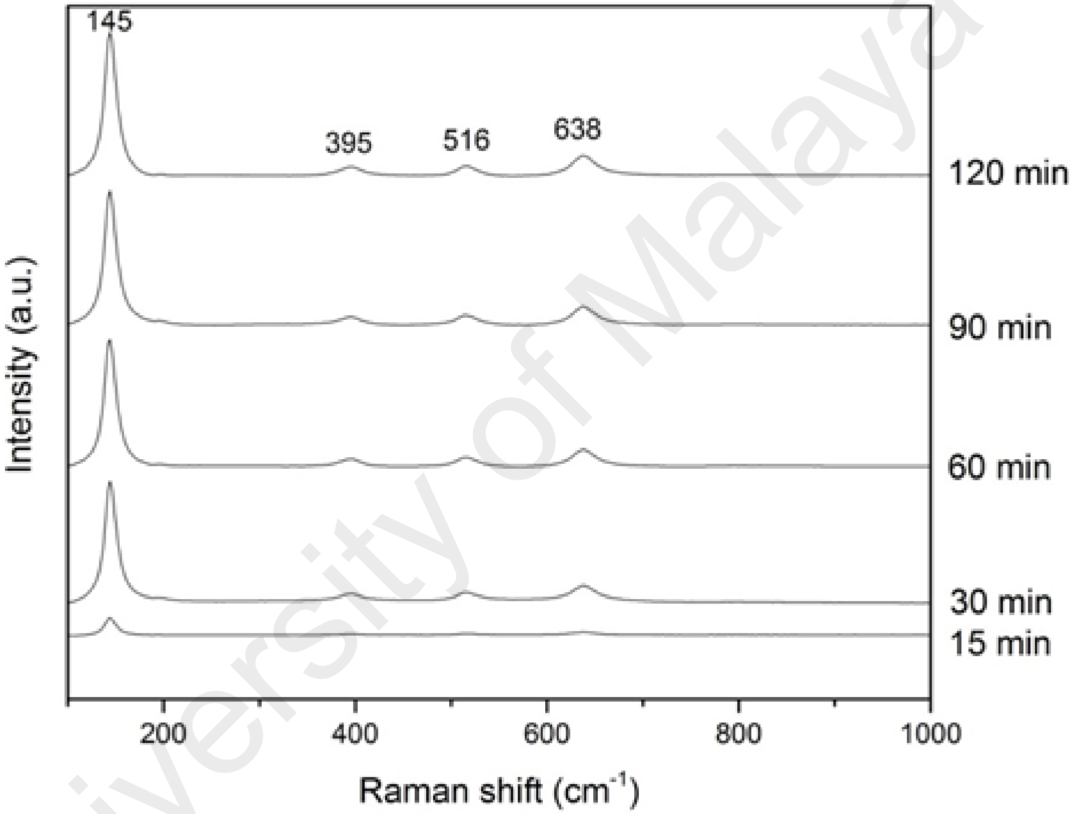

Figure 4.11: Raman spectrum of WO_3-loaded TiO_2 nanotubes produced at different anodization duration in ethylene glycol containing 0.3 wt% NH_4F at 40 V

4.5 Carrier Recombination Analysis by Photoluminescence Spectroscopy

The photoluminescence, PL emission spectra is a useful characterization tool which can be used to investigate the efficiency of charge carrier trapping by understanding the fate of electrons and holes in semiconductor because PL emission is the result of the recombination of free carriers. Thus, PL analysis was done on the selected best sample and the results were compared with the pure TiO_2 sample to investigate the effect of WO_3 doping on the optical properties of the nanotubes.

Figure 4.12 shows the PL spectra of WO_3-loaded TiO_2 nanotubes and pure TiO_2 nanotubes. It can be clearly seen that the PL emission intensity for pure TiO_2 nanotubes is higher than the PL emission intensity for WO_3-loaded TiO_2 nanotubes. Since the PL emission mainly results from the recombination of excited electrons and holes, we can deduce that the lower PL intensity indicates that the WO_3-loaded TiO_2 nanotubes have lower recombination rate compared to the pure TiO_2 nanotube sample. This variation in PL emission intensity may be due to the presence of WO_3 species in the WO_3-loaded TiO_2 nanotubes which suppressed the recombination of the photogenerated carriers and increased charge separation of TiO_2 (Schmidt, 2007). This is due to the more cathodic valence and conduction band potentials of TiO_2 which allows electron transfer from the conduction band of TiO_2 down to the conduction band of WO_3, thus suppressing the recombination of photogenerated carriers (Yu et al., 2010).

The ratio of I_{UV}/I_{Vis} of the samples is compared since I_{UV} is related to intrinsic characteristic of TiO_2 and I_{Vis} is related to the amount of defects in TiO_2 and thus the intensity ratio between the UV peak intensity and the visible peak intensity (I_{UV}/I_{Vis}) is a measure of the nanotubes film structural quality. The I_{UV}/I_{Vis} ratio of pure TiO_2 nanotube sample and WO_3-loaded TiO_2 nanotube sample were found to be approximately 0.13 and 0.21 respectively. The I_{UV}/I_{Vis} ratio of pure TiO_2 nanotube sample is significantly higher than that of WO_3-loaded TiO_2 nanotube sample, suggesting that lower defects were induced in the WO_3-loaded TiO_2 nanotube sample (Magne et al., 2013). Moreover, the pure TiO_2 nanotube sample showed intense visible band which signified the presence of severe structural defects in the sample. By comparison, the WO_3-loaded TiO_2 nanotube sample exhibited less intense visible emission indicating that fewer defects were detected (Ridha et al., 2013). The higher intensity I_{UV}/I_{Vis} ratio of the WO_3-loaded TiO_2 nanotube sample suggests that it has better optical quality than the pure TiO_2 nanotube sample (Asib et al., 2014).

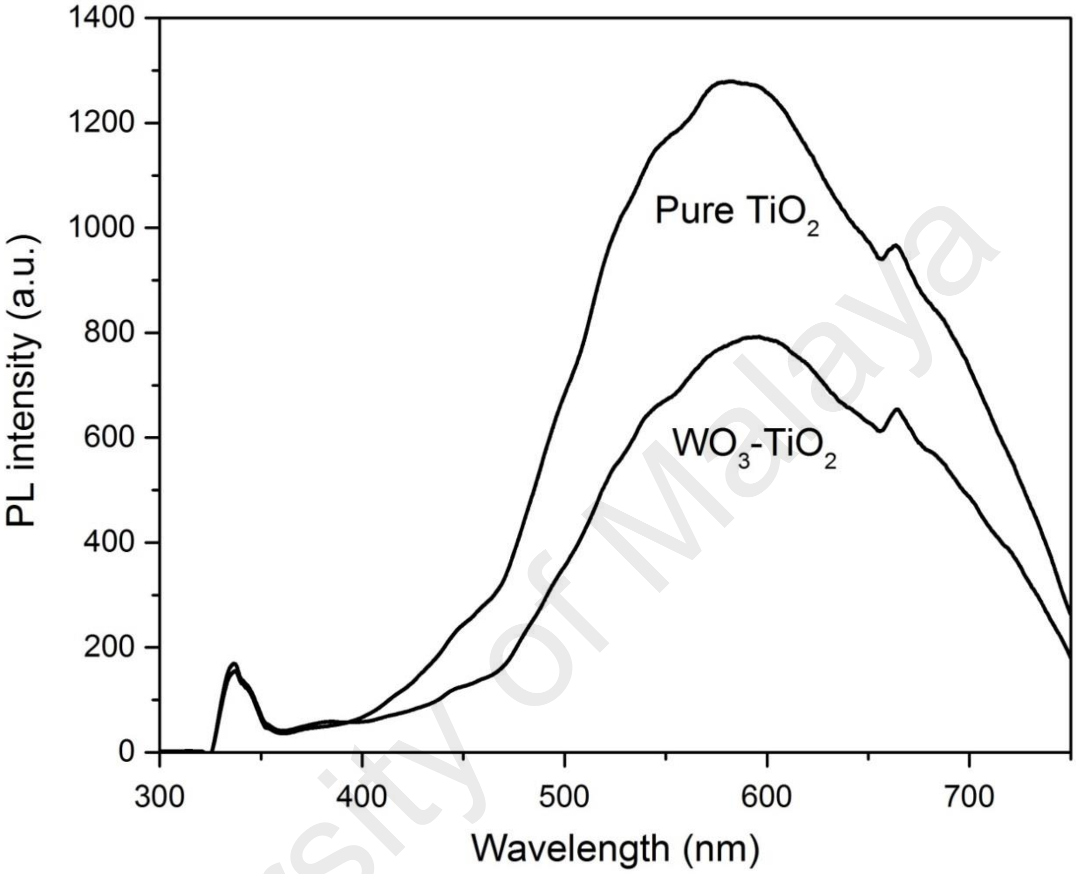

Figure 4.12: Smooth PL curve for WO_3-loaded TiO_2 nanotubes and pure TiO_2 nanotubes synthesized at 40 V in ethylene glycol containing 0.3 wt% NH_4F for 120 minutes

4.6 Optical Properties Analysis by UV-vis DRS

The optical absorption is a key factor in photocatalysis performance. UV-vis DRS is the key characterization technique to study the light absorption properties of materials because it can display the drift, accumulation and recombination of photogenerated carriers as well as useful in estimating the energy band gap (E_{bg}) of the samples. Thus, in this research, the effect of WO_3 doping on the optical absorption properties of TiO_2 nanotubes was investigated using UV-vis DRS.

Figure 4.13 shows the optical absorption patterns of WO_3-loaded TiO_2 nanotubes and pure TiO_2 nanotubes. Both the WO_3-loaded TiO_2 nanotubes and pure TiO_2 nanotubes show excellent absorption performance in the UV range. Furthermore, in the whole UV-vis light region, WO_3-loaded TiO_2 nanotubes exhibit higher light absorbance than pure TiO_2 nanotubes and show a red shift in the absorption edges.

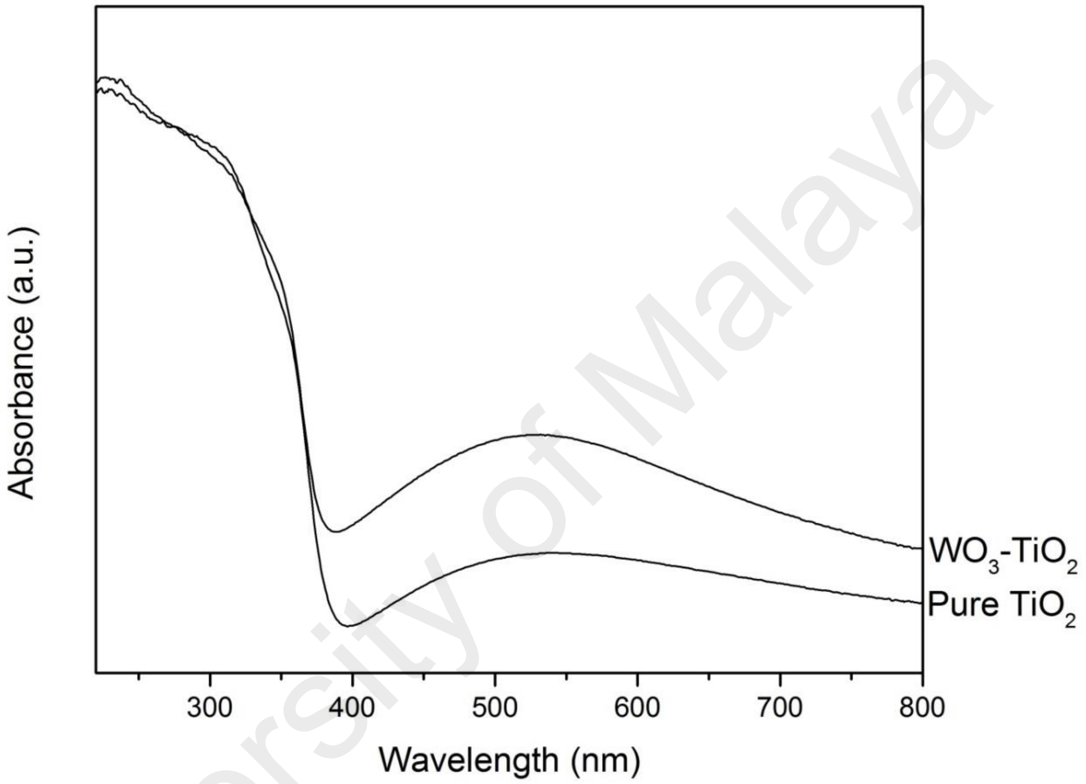

Figure 4.13: Absorption patterns of WO_3-loaded TiO_2 nanotubes and pure TiO_2 nanotubes synthesized at 40 V in ethylene glycol containing 0.3 wt% NH_4F for 120 minutes

The band gap energy values of pure TiO_2 nanotubes and WO_3-loaded TiO_2 nanotubes were estimated with the Kubelka-Munk function using the plot of $(\alpha h\nu)^{1/2}$ versus $h\nu$ as shown in Figures 4.14 and 4.15 respectively. According to Figure 4.14, the band gap energy of pure TiO_2 nanotubes was estimated to be 2.84 eV. This band gap value is significantly lower than the typical band gap value of TiO_2 (3.2 eV), attributed to the presence of carbon species within the TiO_2 nanotubes which significantly enhanced the visible light responsiveness of the TiO_2 nanotubes. The band gap energy of TiO_2 is narrowed down by the mixing of the delocalized p state of the carbon species with the 2p orbital of the oxygen species in the valence band of TiO_2 which shifts the valence band edge of TiO_2 upwards (Lai & Sreekantan, 2013b). The band gap energy decreased progressively to 2.72 eV for the WO_3-loaded TiO_2 nanotubes. This finding suggests that the conduction band of the TiO_2 nanotubes was reformed in the presence of W^{6+} ions (Xin et al., 2013). This result also shows that incorporation of WO_3 into TiO_2 would shift the light absorption threshold toward the visible light region and increase the light absorption ability (Lai & Sreekantan, 2013c).

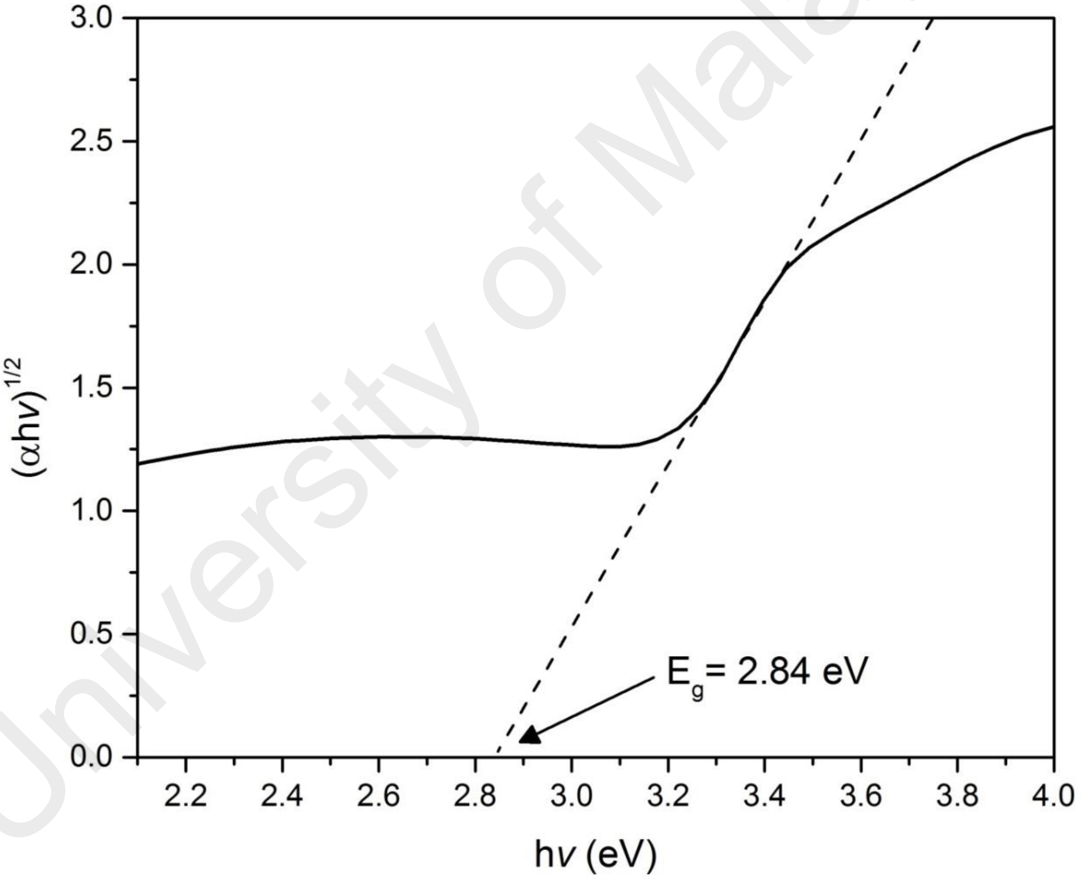

Figure 4.14: Plot of $(\alpha h\nu)^{1/2}$ versus hν employed to calculate the band gap value of pure TiO_2 nanotubes synthesized at 40 V in ethylene glycol containing 0.3 wt% NH_4F for 120 minutes

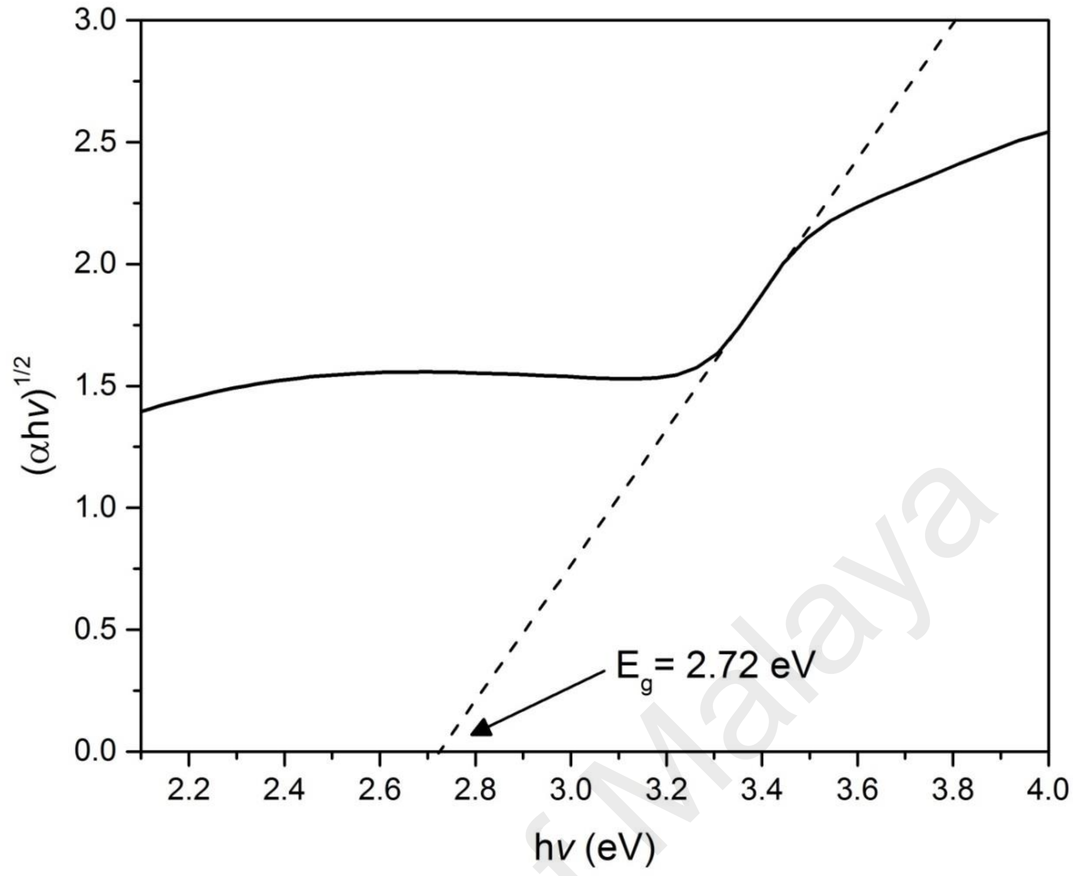

Figure 4.15: Plot of $(\alpha h\nu)^{1/2}$ versus hν employed to calculate the band gap value of WO_3-loaded TiO_2 nanotubes synthesized at 40 V in ethylene glycol containing 0.3 wt% NH_4F for 120 minutes

4.7 Chemical State Analysis by XPS

XPS measurements were carried out on selected best sample to investigate the chemical composition and oxidation state of the WO_3-loaded TiO_2 nanotubes and to compare it with the pure TiO_2 sample. Figure 4.16 shows the XPS survey spectra, which shows the presence of Ti, O, C and W elements within the prepared samples and indicating that WO_3 was successfully loaded onto the nanotubes. The XPS results also further confirmed the elemental identification by EDX analysis.

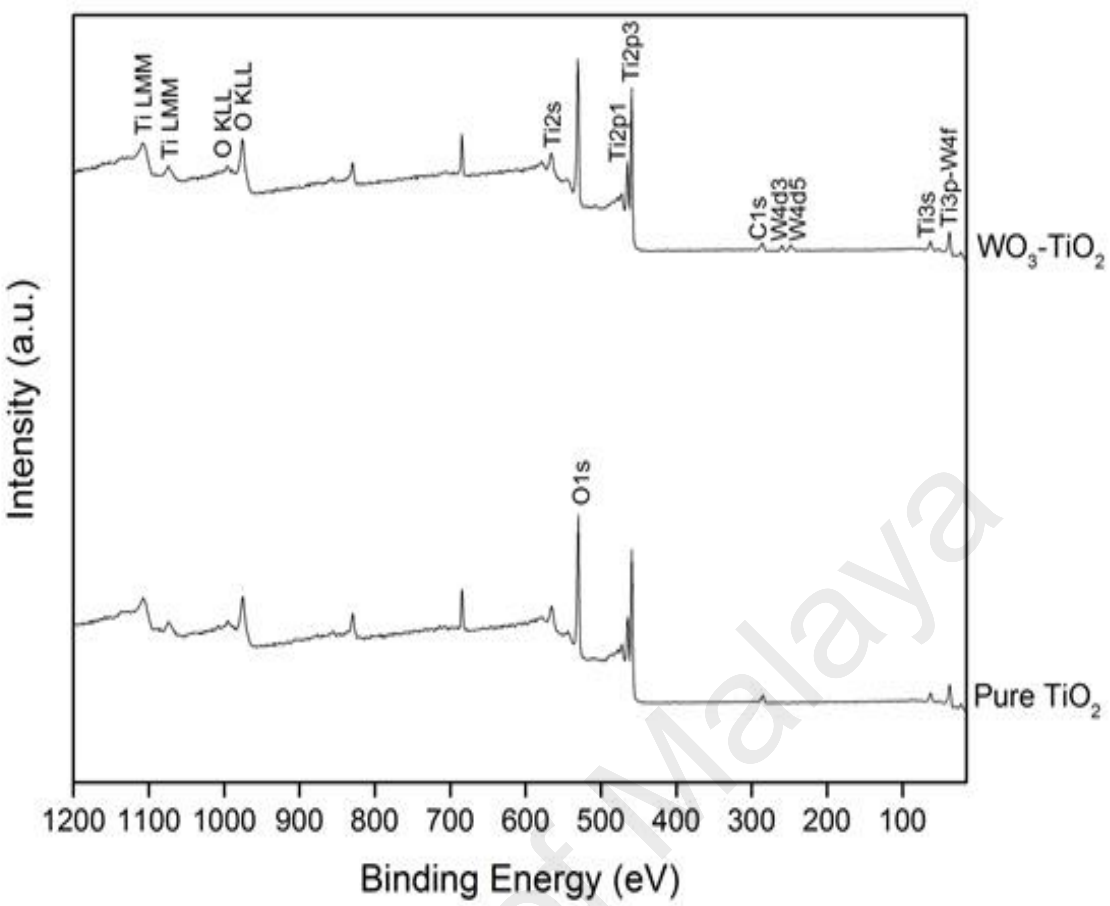

Figure 4.16: XPS survey spectra of WO_3-loaded TiO_2 nanotubes and pure TiO_2 nanotubes synthesized at 40 V in ethylene glycol containing 0.3 wt% NH_4F for 120 minutes

Figure 4.17 shows the Ti2p XPS spectra. The binding energies of $Ti2p_{3/2}$ and $Ti2p_{1/2}$ for pure TiO_2 nanotubes were located at 459.0 and 464.8 eV, respectively, which are attributed to the Ti^{4+}. For the WO_3-loaded TiO_2 nanotube samples, the binding energies of $Ti2p_{3/2}$ and $Ti2p_{1/2}$ were detected at 459.6 and 465.4 eV, respectively. The positive shift of the binding energy was mainly attributed to the presence of W–O–Ti linkage within the lattice and associated with the contraction of TiO_2 unit cells by diffusing of W^{6+} ions within the TiO_2 lattice. This result proves that the W^{6+} ions were loaded into the bulk TiO_2 lattice by displacing Ti^{4+}, and formed the W–O–Ti bonding (Lai & Sreekantan, 2013d; Lai & Sreekantan, 2012).

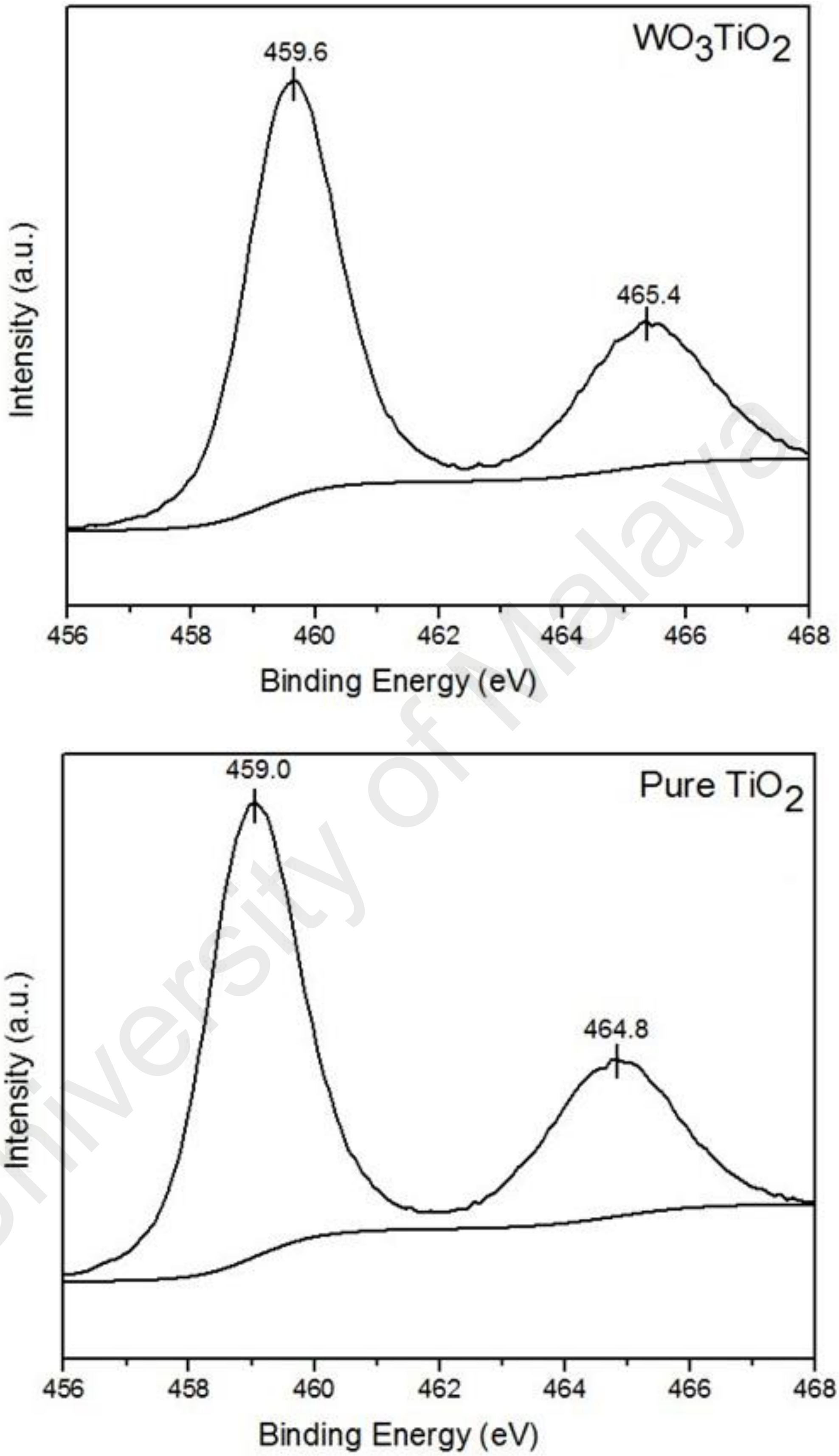

Figure 4.17: XPS spectra of Ti2p

The XPS spectra of the O 1s region are shown in Figure 4.18. The XPS spectra of the pure TiO_2 nanotubes showed binding energies of 530.1 and 531.8 eV, suggesting the presence of two kinds of oxygen species in the near-surface region, namely, oxygen in the TiO_2 structure and that adsorbed on the TiO_2 surface (–OH). There was a slight increase in O1s binding energy from 530.1 eV to 530.7 eV when WO_3 species were loaded on the TiO_2 nanotubes. This result indicates the formation of the W–O–Ti bond from Ti–O and W–O. The O state with higher intensity peak at 530.8 eV was assigned to the oxygen in the TiO_2 and WO_3 structures (Lai & Sreekantan, 2013d; Lai & Sreekantan, 2012).

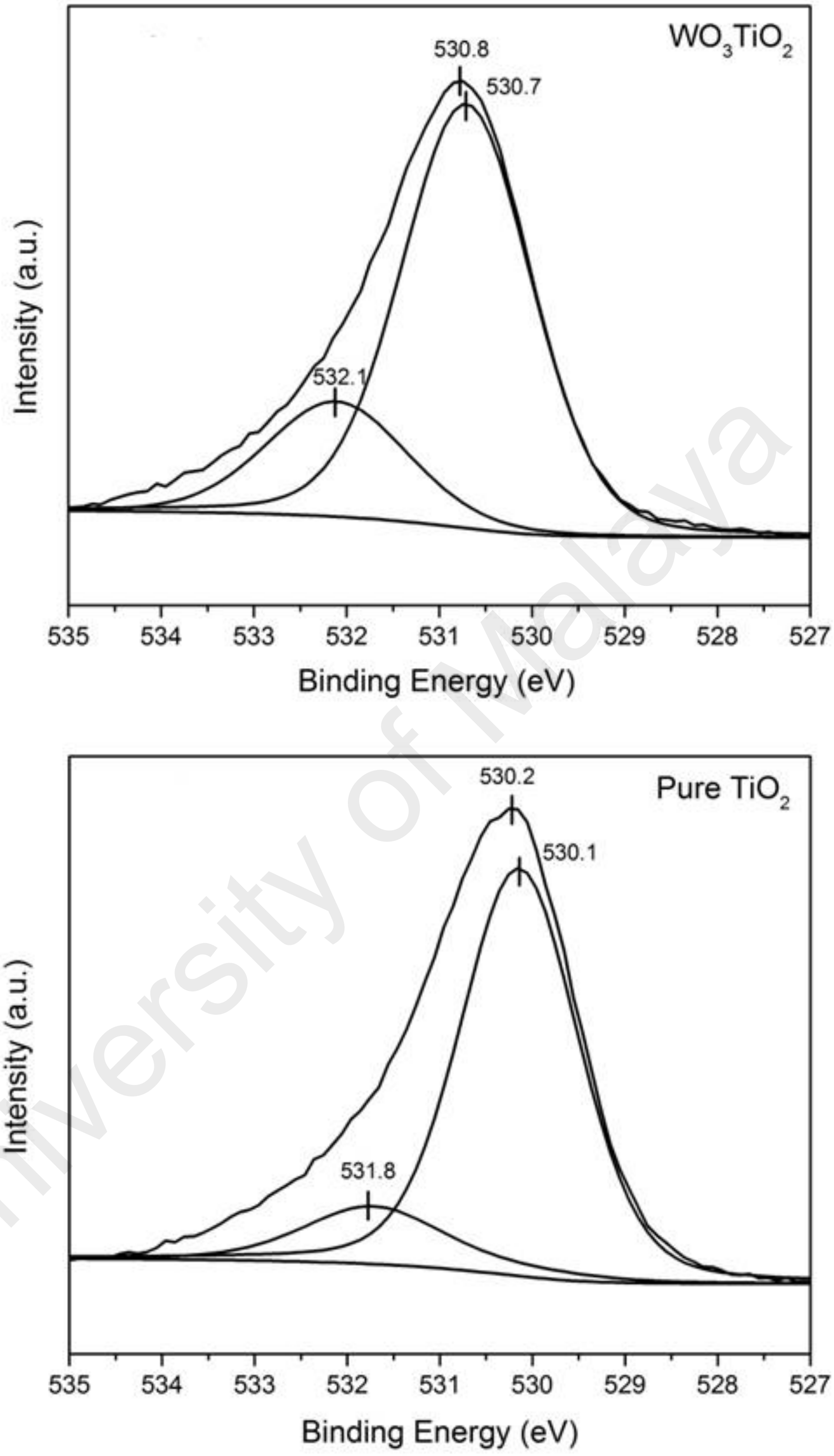

Figure 4.18: XPS spectra of O1s

The C1s binding energy is shown in Figure 4.19. For the pure TiO_2 sample, the presence of a carbon-binding energy at 284.5 eV is due to the adventitious hydrocarbon from the XPS instrument itself. The peak at 286.0–289.2 eV indicates that a small amount of carbonate species was present on the surface. The consistent C1s shift toward higher energies for WO_3-loaded TiO_2 nanotubes sample indicates that TiO_2 was modified by WO_3 species. Meanwhile, the peak at 285.7 eV is ascribed to the Ti–C–O bonds of the carbonate species originating from the residual C of the organic ethylene glycol electrolyte. The presence of C in the nanotube arrays resulted from the adsorption of carbonate species from the pyrogenation of EG, and the C atom was diffused into the TiO_2 crystal structure during the annealing process. Thus, heat treatment plays an important role to form the Ti–C–O bonds (Lai & Sreekantan, 2013d; Lai & Sreekantan, 2012).

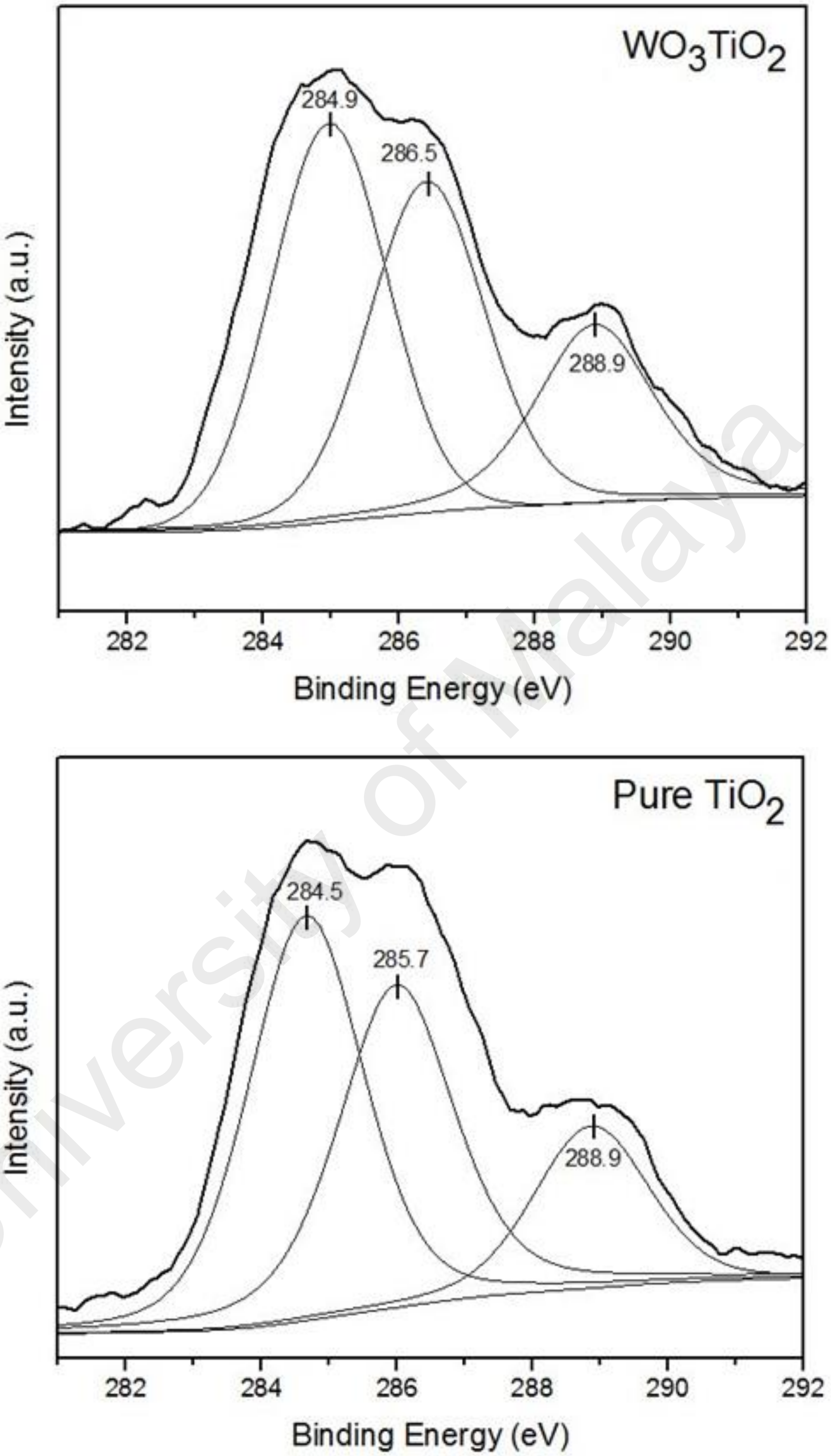

Figure 4.19: XPS spectra of C1s

Since the W4f peak and Ti3p peak were partially overlapping in the XPS spectra, the W4d peak is presented in Figure 4.20. The pure TiO_2 nanotube sample did not exhibit any W4d peak from the XPS spectra. The annealed WO_3-loaded TiO_2 nanotubes sample exhibited peaks at 248.3 and 260.3eV which were assigned to $W4d_{5/2}$ and $W4d_{3/2}$ respectively. These were attributed to the typical valence band peaks for W^{6+} species, suggesting the formation of W–O–Ti bonds in neutral form. This result confirms that W^{6+} species interacted with the TiO_2 lattice through the atomic layers. This result suggests that heat treatment can effectively incorporate W^{6+} ions into the TiO_2 lattice and form W–O–Ti bonds. The W^{6+} ion (74.0 pm) is similar in size to the Ti^{4+} ion (74.5 pm) (Lai & Sreekantan, 2013d; Lai & Sreekantan, 2012).

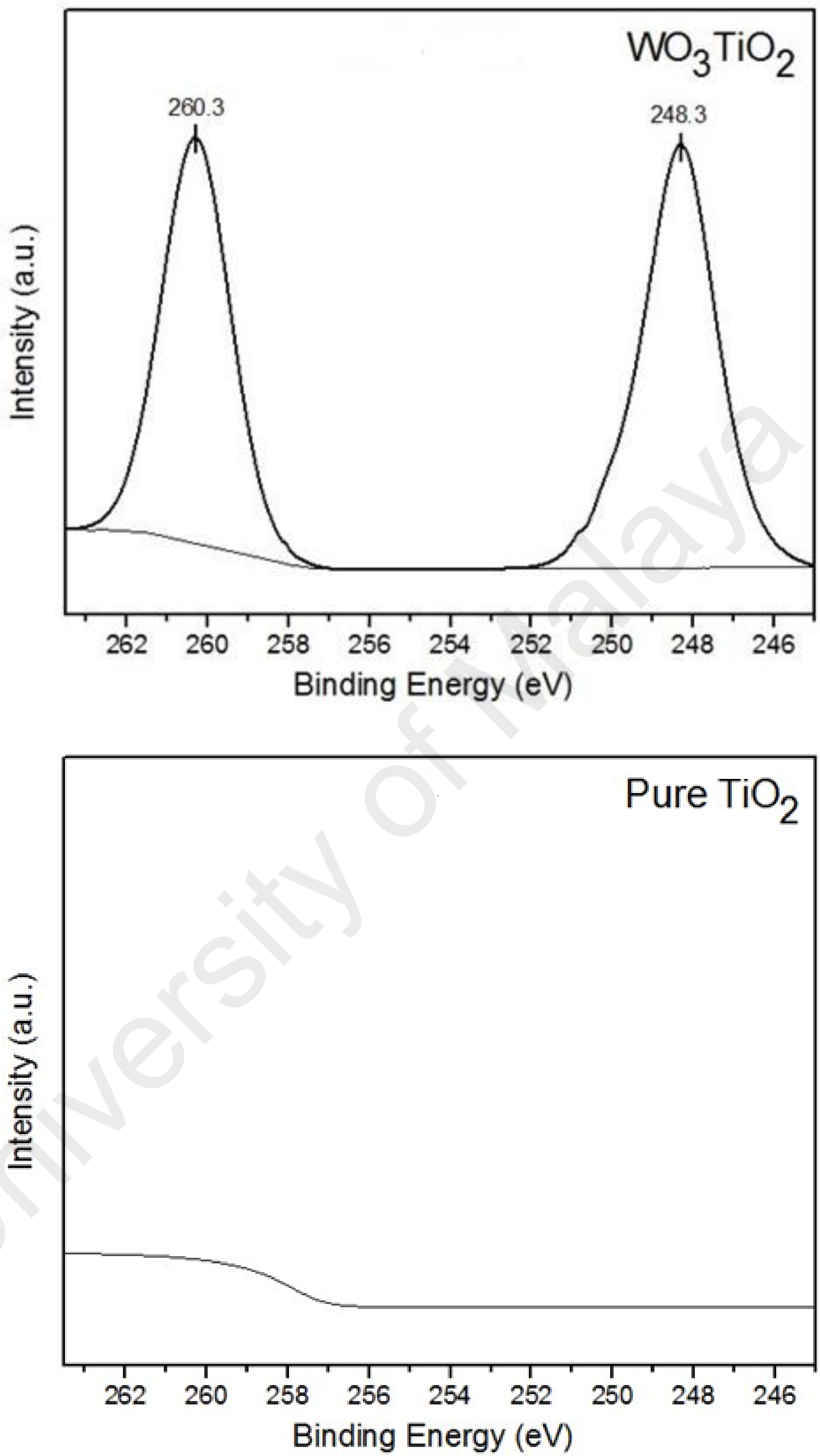

Figure 4.20: XPS spectra of W4d

4.8 Photocatalytic Mercury Removal Performance

It is well known that TiO_2 can reduce aqueous mercury ions under UV illumination. TiO_2 nanotubes, being of nanosize, will have much interaction with mercury ions, which can lead to absorbtion. Thus, photocatalytic reduction of mercury ions leads to conversion to lower oxidation states and probable deposition onto TiO_2 surface as a zerovalent metal (Suriyawong et al., 2009; Tsai et al., 2012). Researchers have shown that mercury removal involving TiO_2 would be greater under photocatalysis conditions (Byrne & Mazyck, 2009). Therefore, photocatalytic reduction of mercury ions using TiO_2 nanostructures has become a promising mercury removal method. Under UV light, TiO_2 will be photoactive and generate e^-/h^+ pairs (Equation 4.10). Then, the adsorbed Hg^{2+} ions will be reduced by the e^- on the TiO_2 surface (Equation 4.11). Figure 4.21 shows the absorbtion of Hg^{2+} onto the catalyst surface to undergo reduction to Hg^0.

$$TiO_2 + h\nu \rightarrow h^+ + e^- \qquad \text{[Equation 4.10]}$$

$$Hg^{2+} + 2e^- \rightarrow Hg^0 \qquad \text{[Equation 4.11]}$$

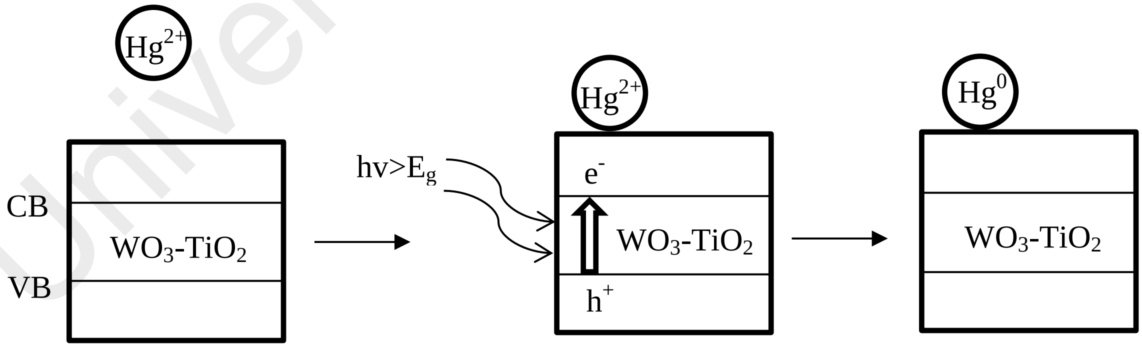

Figure 4.21: Photocatalytic reduction of Hg^{2+} ions by WO_3-loaded TiO_2 nanotubes: (a) Hg^{2+} in aqueous medium, (b) absorbtion of Hg^{2+} onto catalyst surface, and (c) reduction of Hg^{2+} ions to Hg^0

4.8.1 The Effect of Anodization Voltage

The photocatalytic reduction of Hg^{2+} in aqueous solution by WO_3-loaded TiO_2 nanotubes under UV illumination was investigated. As shown in Figure 4.22 and Table 4.7, the nanotubes produced at 40 V showed the best mercury removal performance where 65% of the mercury in initial solution was removed after two hours of UV irradiation. The sample produced at 30 V showed a slightly lower performance where 62% of the mercury in initial solution was successfully removed. The samples produced at 10 V and 20 V showed the lowest performance of mercury removal where only 28% and 46% of the initial mercury concentration were successfully removed, respectively.

The reason for the better performance of sample produced at 40 V is due to larger active surface area which increased the interaction between adsorbent and adsorbate, therefore increased mercury adsorption in a less time (Byrne & Mazyck, 2009). Furthermore, with larger active surface area, more UV photons could be absorbed or refracted to generate more photo-induced electron-hole pairs which allow more Hg^{2+} to undergo reduction (Skubal & Meshkov, 2002; Nischk et al., 2014). However the 20 V and 30 V samples have almost similar G value which is about 85, but the performance of the 30 V sample is about 20% higher than the 20 V sample. This is attributed to the higher tungsten dopant loading amount in the 30 V sample which is 2.01 at% tungsten compared with the 20 V sample with only 1.36 at% tungsten as shown in the EDX results. The higher amount of tungsten loading caused significant improvement in the photocatalytic activity of the nanotube arrays due to suppression of the recombination of the photogenerated carriers and increased charge separation of TiO_2 (Schmidt, 2007). In order to compare the photocatalytic activity of WO_3-loaded TiO_2 nanotubes with pure TiO_2 nanotubes, pure TiO_2 nanotubes were produced using the same parameters as the WO_3-loaded TiO_2 nanotubes synthesized at 40 V (with 0.5 wt% NH_4F and 30 minutes anodization) except replacing the tungsten cathode with a platinum cathode. As compared to WO_3-loaded TiO_2 nanotubes, pure TiO_2 nanotube arrays showed a lower efficiency of mercury removal, where 55% of the mercury in initial solution was removed after 2 hours. This shows that the coupling of WO_3 and TiO_2 gives significant improvement in the photocatalytic activity of the nanotube arrays due to suppression of the recombination of the photogenerated carriers and increased charge separation of TiO_2. When a photon with not enough energy to excite TiO_2 but is of enough energy to excite WO_3 is incident, the hole that is created in the WO_3 valence band is excited to the conduction band of TiO_2, while the electron is transferred to the conduction band of TiO_2. This electron transfer increases the charge separation, thus leading to a lower recombination rate (Schmidt, 2007). Furthermore, since the valence and conduction band potentials of TiO_2 are more cathodic than that of WO_3, photogenerated electrons can transfer from the conduction band of TiO_2 down to the conduction band of WO_3. This will suppress the recombination of photogenerated carriers (Yu et al., 2010).

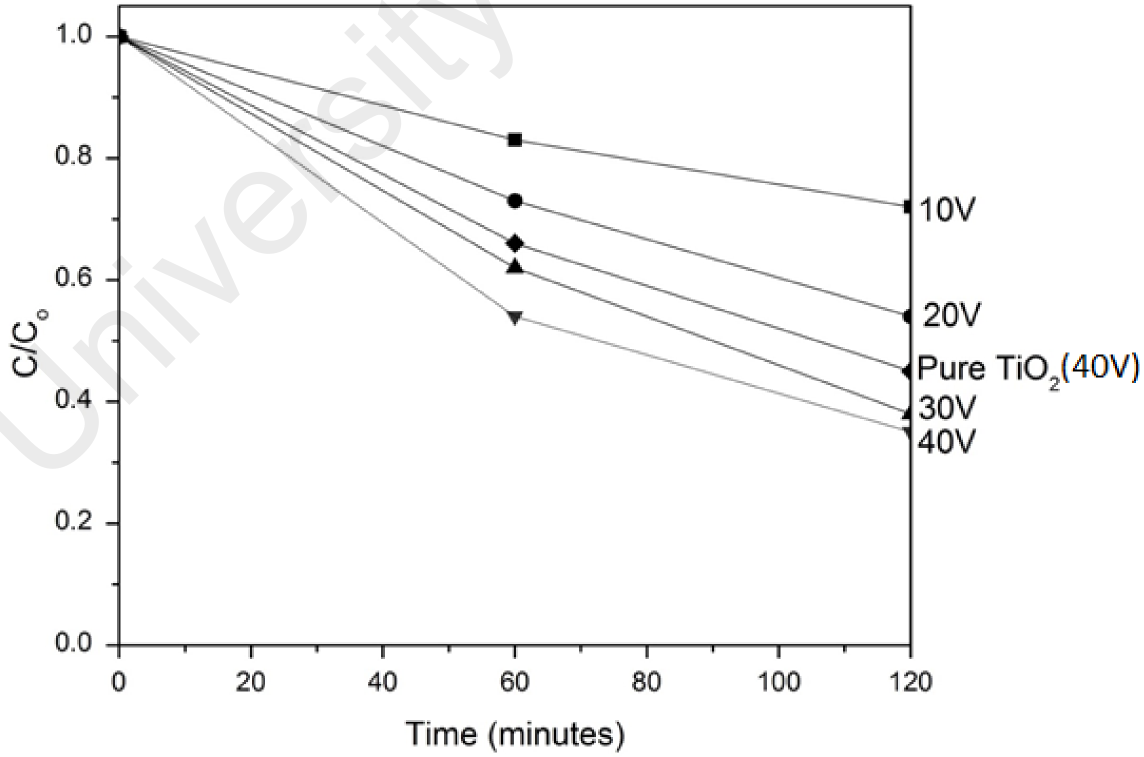

Figure 4.22: Removal of Hg^{2+} by WO_3-loaded TiO_2 nanotubes synthesized at different anodization voltage in ethylene glycol containing 0.5 wt% NH_4F for 30 minutes

Table 4.7: Initial mercury concentration removed by WO_3-loaded TiO_2 nanotubes synthesized at different anodization voltage in ethylene glycol containing 0.5 wt% NH_4F for 30 minutes

Sample	**Initial mercury concentration removed**
10 V	28%
20 V	46%
30 V	62%
40 V	65%
Pure TiO_2	55%

The kinetics of photocatalytic mercury removal is illustrated in Figure 4.23. The linearity of the curves suggests that the photocatalytic removal of mercury can be described by the first-order kinetic model, $\ln(C_0/C) = kt$, where C_0 is the initial concentration and C is the concentration at time t. The plots of the concentration data gave a straight line. The results of fitting experimental data to pseudo-first-order kinetics are given in Table 4.8. The rate constant increases with increasing anodization voltage. This shows that the WO_3-loaded TiO_2 nanotubes synthesized at 40 V demonstrated the best photocatalytic removal of mercury among the samples produced.

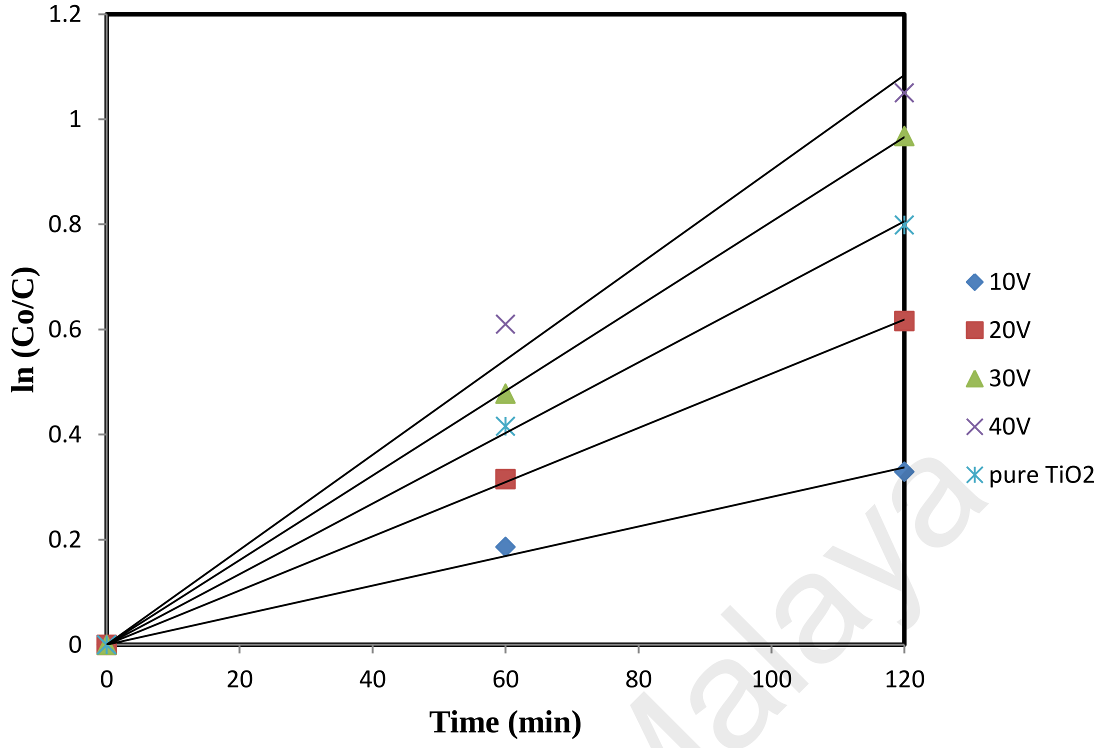

Figure 4.23: Pseudo-first-order kinetics for photocatalytic removal of mercury using WO_3-loaded TiO_2 nanotubes synthesized at different anodization voltage in ethylene glycol containing 0.5 wt% NH_4F for 30 minutes

Table 4.8: Rate constants for photocatalytic mercury removal by WO_3-loaded TiO_2 nanotubes synthesized at different anodization voltage in ethylene glycol containing 0.5 wt% NH_4F for 30 minutes

Sample	**Rate constant (*k*)**	**R^2**
10 V	0.0028	0.9932
20 V	0.0052	0.9998
30 V	0.0080	0.9999
40 V	0.0090	0.9896
Pure TiO_2	0.0067	0.9993

4.8.2 The Effect of Fluoride Ion Content

As shown in Figure 4.24 and Table 4.9, the nanotubes produced using 0.3 wt% NH_4F showed the best mercury removal performance where 76% of the mercury in initial solution was removed after two hours of UV irradiation. The sample produced using 0.5 wt% NH_4F showed a slightly lower performance where 71% of the mercury in initial solution was successfully removed. The samples produced with 0 and 0.1 wt% of NH_4F showed the lowest performance of mercury removal where only 9% and 43% of the initial mercury concentration were successfully removed, respectively.

The reason for the better performance of sample produced with 0.3 wt% NH_4F is due to larger active surface area which increased the interaction between adsorbent and adsorbate, therefore increased mercury adsorption in a less time (Byrne & Mazyck, 2009). Furthermore, with larger active surface area, more UV photons could be absorbed or refracted to generate more photo-induced electron-hole pairs which allow more Hg^{2+} to undergo reduction (Skubal & Meshkov, 2002; Nischk et al., 2014). In order to compare the photocatalytic activity of WO_3-loaded TiO_2 nanotubes with pure TiO_2 nanotubes, pure TiO_2 nanotubes were produced using the same parameters as the WO_3-loaded TiO_2 nanotubes synthesized using 0.3 wt% NH_4F (at 40V and 60 minutes anodization) except replacing the tungsten cathode with a platinum cathode. As compared to WO_3-loaded TiO_2 nanotubes, pure TiO_2 nanotube arrays showed a lower efficiency of mercury removal, where 57% of the mercury in initial solution was removed after 2 hours. This shows that the coupling of WO_3 and TiO_2 gives significant improvement in the photocatalytic activity of the nanotube arrays due to suppression of the recombination of the photogenerated carriers and increased charge separation of TiO_2 (Yu et al., 2010).

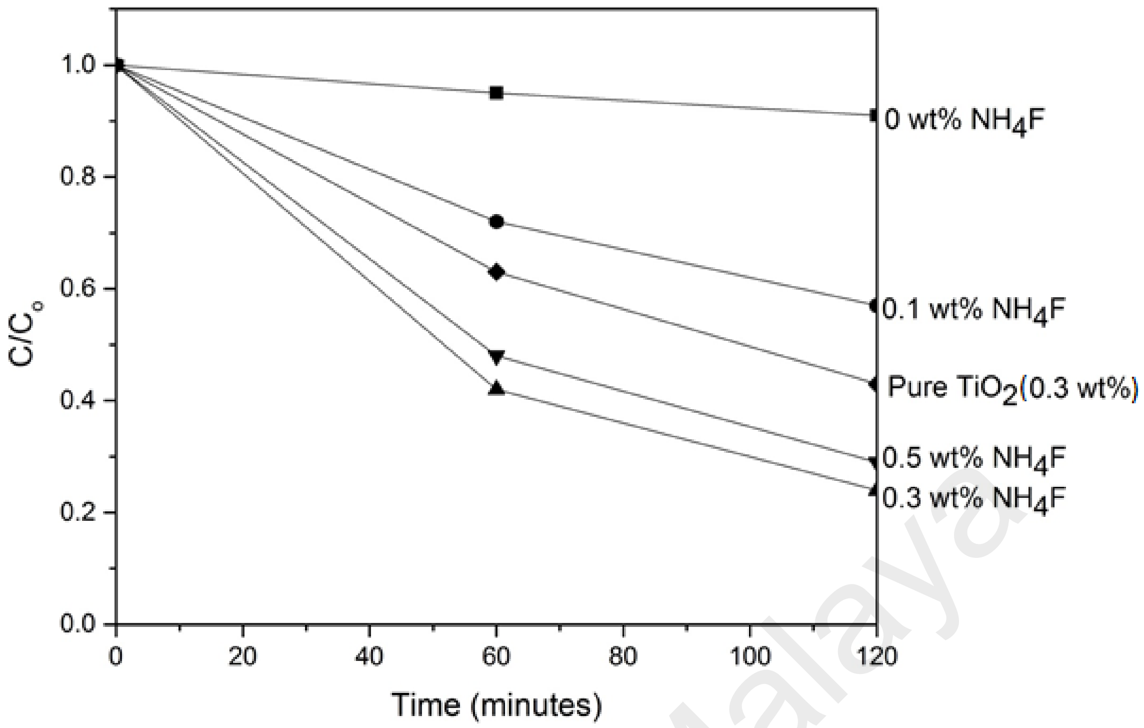

Figure 4.24: Removal of Hg^{2+} by WO_3-loaded TiO_2 nanotubes synthesized with different fluoride ion content at 40 V for 60 minutes

Table 4.9: Initial mercury concentration removed by WO_3-loaded TiO_2 nanotubes synthesized with different fluoride ion content at 40 V for 60 minutes

Sample	**Initial mercury concentration removed**
0 wt%	9%
0.1 wt%	43%
0.3 wt%	76%
0.5 wt%	71%
Pure TiO_2	57%

The kinetics of photocatalytic mercury removal is illustrated in Figure 4.25. The linearity of the curves suggests that the photocatalytic removal of mercury can be described by the first-order kinetic model, $\ln(C_0/C) = kt$, where C_0 is the initial concentration and C is the concentration at time t. The plots of the concentration data gave a straight line. The results of fitting experimental data to pseudo-first-order kinetics are given in Table 4.10. The rate constant firstly increases with increasing fluoride ion content up to 0.3 wt% then decreases with further increasing fluoride ion content. This shows that the WO_3-loaded TiO_2 nanotubes synthesized with 0.3 wt% NH_4F demonstrated the best photocatalytic removal of mercury among the samples produced.

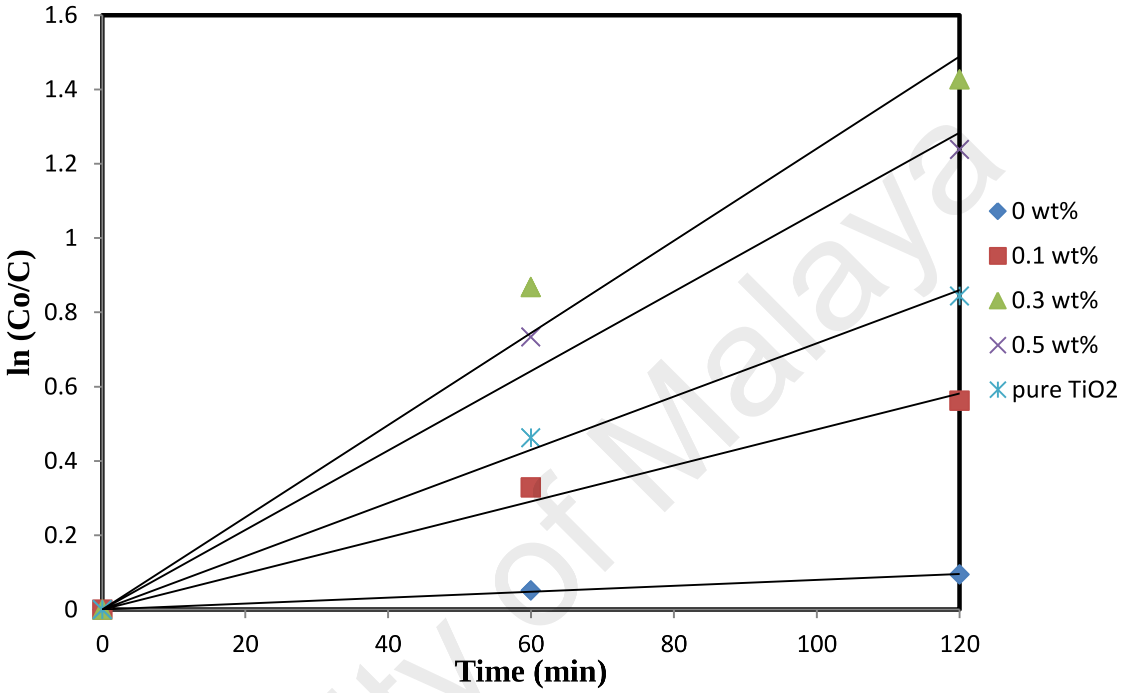

Figure 4.25: Pseudo-first-order kinetics for photocatalytic removal of mercury using WO_3-loaded TiO_2 nanotubes synthesized with different fluoride ion content at 40 V for 60 minutes

Table 4.10: Rate constants for photocatalytic mercury removal by WO_3-loaded TiO_2 nanotubes synthesized with different fluoride ion content at 40 V for 60 minutes

Sample	**Rate constant (*k*)**	R^2
0 wt%	0.0008	0.9971
0.1 wt%	0.0048	0.9884
0.3 wt%	0.0124	0.9815
0.5 wt%	0.0107	0.9864
Pure TiO_2	0.0072	0.9964

4.8.3 The Effect of Anodization Duration

As shown in Figure 4.26 and Table 4.11, the nanotubes produced at 120 minutes showed the best mercury removal performance where 91% of the mercury in initial solution was removed after two hours of UV irradiation. WO_3-loaded TiO_2 nanotubes produced at 90 minutes showed a slightly lower performance where 87% of the mercury in initial solution was successfully removed. The samples produced at 60 minutes and 30 minutes showed lower performance of mercury removal where only 77% and 53% of the initial mercury concentration were successfully removed, respectively. The sample produced at 15 minutes showed the lowest performance of mercury removal where only 11% of the initial mercury concentration was successfully removed.

The reason for the better performance of sample produced at 120 minutes is due to larger active surface area which increased the interaction between adsorbent and adsorbate, therefore increased mercury adsorption in less time (Byrne & Mazyck, 2009). Furthermore, with larger active surface area, more UV photons could be absorbed or refracted to generate more photo-induced electron-hole pairs which allow more Hg^{2+} to undergo reduction (Skubal & Meshkov, 2002; Nischk et al., 2014). In order to compare the photocatalytic activity of WO_3-loaded TiO_2 nanotubes with pure TiO_2 nanotubes, pure TiO_2 nanotubes were produced using the same parameters as the WO_3-loaded TiO_2 nanotubes synthesized at 120 minutes (at 40 V and 0.3 wt% NH_4F) except replacing the tungsten cathode with a platinum cathode. As compared to WO_3-loaded TiO_2 nanotubes, pure TiO_2 nanotube arrays showed a lower efficiency of mercury removal, where 65% of the mercury in initial solution was removed after 2 hours. This shows that the coupling of WO_3 and TiO_2 gives significant improvement in the photocatalytic activity of the nanotube arrays due to suppression of the recombination of the photogenerated carriers and increased charge separation of TiO_2 (Yu et al., 2010).

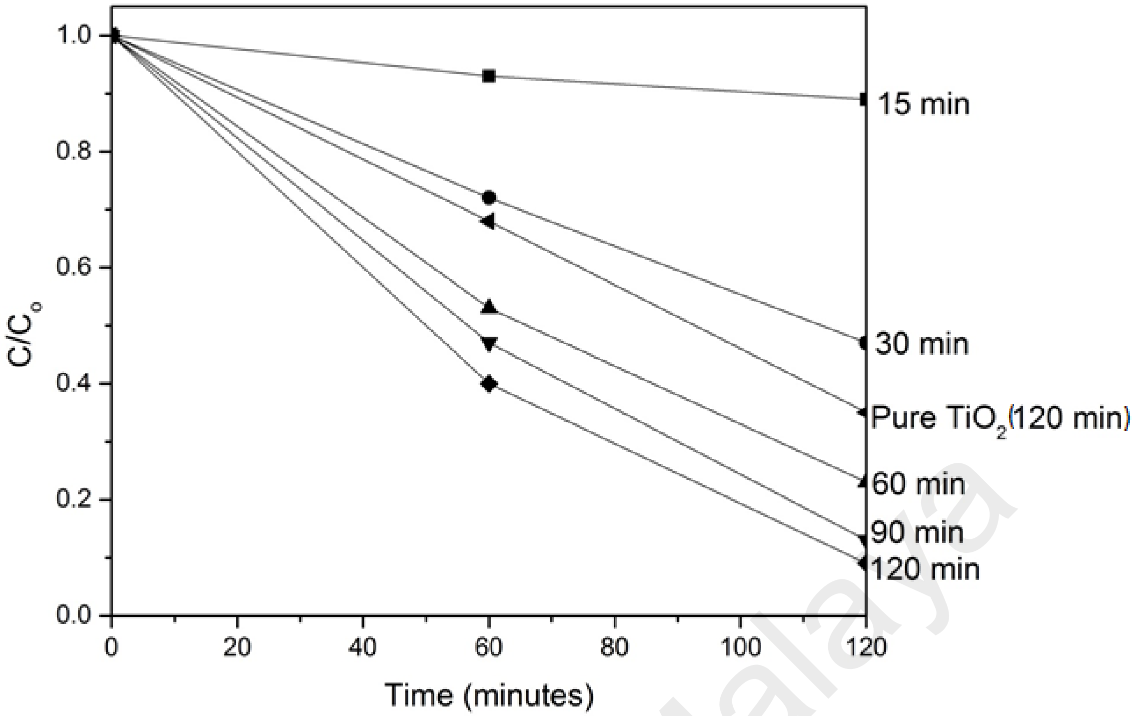

Figure 4.26: Removal of Hg^{2+} by WO_3-loaded TiO_2 nanotubes synthesized at different anodization duration in ethylene glycol containing 0.3 wt% NH_4F at 40 V

Table 4.11: Initial mercury concentration removed by WO_3-loaded TiO_2 nanotubes synthesized at different anodization duration in ethylene glycol containing 0.3 wt% NH_4F at 40 V

Sample	**Initial mercury concentration removed**
15 min	11%
30 min	53%
60 min	77%
90 min	87%
120 min	91%
Pure TiO_2	65%

The kinetics of photocatalytic mercury removal is illustrated in Figure 4.27. The linearity of the curves suggests that the photocatalytic removal of mercury can be described by the first-order kinetic model, $\ln(C_0/C) = kt$, where C_0 is the initial concentration and C is the concentration at time t. The plots of the concentration data gave a straight line. The results of fitting experimental data to pseudo-first-order kinetics are given in Table 4.12. The rate constant increases with increasing anodization duration. This shows that the WO_3-loaded TiO_2 nanotubes synthesized at 120 minutes demonstrated the best photocatalytic removal of mercury among the samples produced.

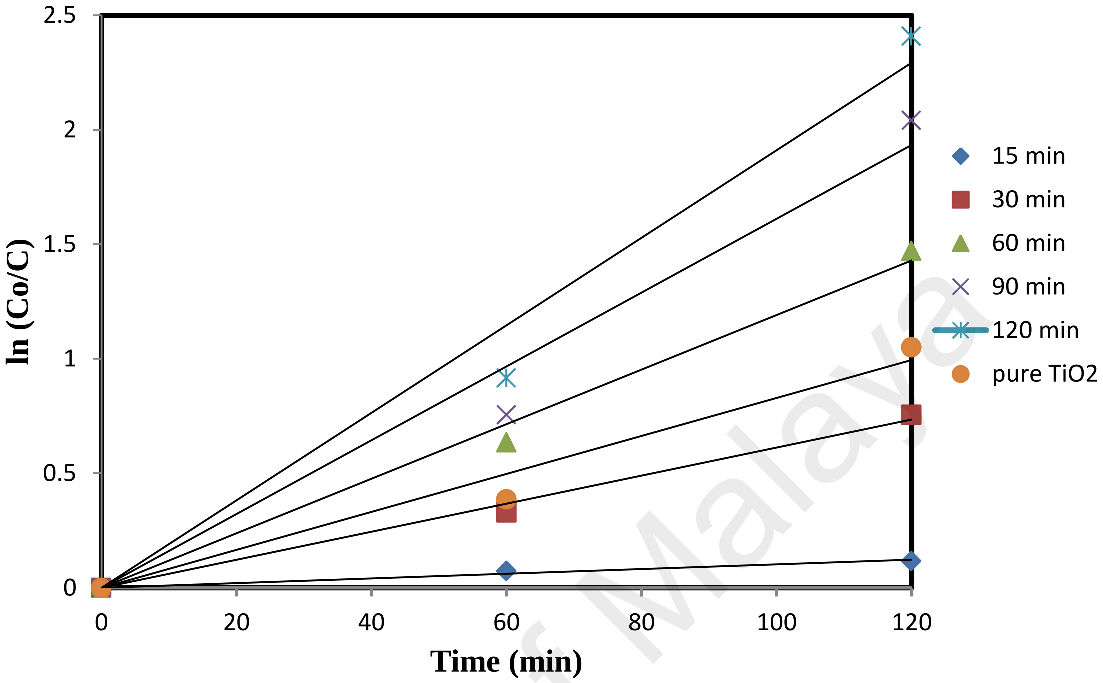

Figure 4.27: Pseudo-first-order kinetics for photocatalytic removal of mercury using WO_3-loaded TiO_2 nanotubes synthesized at different anodization duration in ethylene glycol containing 0.3 wt% NH_4F at 40 V

Table 4.12: Rate constants for photocatalytic mercury removal by WO_3-loaded TiO_2 nanotubes synthesized at different anodization duration in ethylene glycol containing 0.3 wt% NH_4F at 40 V

Sample	**Rate constant (*k*)**	**R^2**
15 min	0.0010	0.9759
30 min	0.0061	0.9934
60 min	0.0119	0.9926
90 min	0.0161	0.9736
120 min	0.0191	0.9775
Pure TiO_2	0.0083	0.9726

CHAPTER 5: CONCLUSION

5.1 Conclusion

This research was devoted to study the synthesis of WO_3-loaded TiO_2 nanotubes using single step electrochemical anodization technique for application in photocatalytic mercury removal under UV irradiation. In summary, the objectives of the experiment were achieved. In the first stage, WO_3-loaded TiO_2 nanotubes were successfully formed by anodization in ethylene glycol electrolyte containing fluoride ions. The conclusions attained in this part of the research are as follows:

- For the effect of applied voltage, the results showed that the nanotubes diameter and length increased when anodization voltage increased. However, excessive voltage will corrode the sample because high voltage will provide higher driving force for ionic species (H^+ and F^-) which significantly increases the chemical dissolution rate of Ti and TiO_2. Anodization voltage of 40 V produced nanotubes with the longest length and largest pore size without corroding the sample.
- The morphology of the nanostructure was also influenced by the amount of dissolution agent used in the anodization process. The optimum amount of NH_4F added in the electrolyte to produce nanotubes with high aspect ratio and surface area was determined to be 0.3 wt%.
- It has also been proven that longer anodization time will produce longer nanotubes. 2 hours was needed to produce nanotubes up to approximately 6 µm in length. However, 30 minutes of anodization is enough to form the TiO_2 nanotubes.

In the second stage, the WO_3-loaded TiO_2 nanotubes were used in the photocatalytic removal of mercury under UV irradiation. The efficiency of mercury removal using WO_3-loaded TiO_2 nanotubes were also compared to pure TiO_2 nanotubes. The conclusions attained in this part of the research are as follows:

- High aspect ratio and geometric surface area factor WO_3-loaded TiO_2 nanotubes exhibited better photocatalytic mercury removal performance due to larger active surface area which increased the interaction between adsorbent and adsorbate, therefore increased mercury adsorption in a less time. Furthermore, with larger active surface area, more UV photons could be absorbed or refracted to generate more photo-induced electron-hole pairs which allow more Hg^{2+} to undergo reduction.
- WO_3-loaded TiO_2 nanotubes showed approximately 1.4 times better photocatalytic mercury removal performance compared to pure TiO_2 nanotubes because the coupling of WO_3 and TiO_2 suppressed the recombination of the photogenerated carriers and increased charge separation of TiO_2.

5.2 Suggestions and Recommendations

In order to bring this technology to practical applications, further studies and developments are required. A few suggestions for further studies were proposed:

- To optimize the properties of the nanotubes, the effect of other parameters such as anodization temperature can be studied as temperature is said to increase the oxidation and dissolution rate during anodization.
- The mechanism of WO_3 species formation and loading onto the TiO_2 nanostructure using the single step anodization method has not been comprehensively studied. Therefore, further studies can be done to gain a deeper understanding on this topic.
- In this work, the use of WO_3-loaded TiO_2 nanotubes in photocatalytic removal of mercury was achieved using UV lamp as the source of energy. Thus, the study of using WO_3-loaded TiO_2 nanotubes in photocatalytic removal of mercury under solar irradiation would be a good suggestion for further studies.

REFERENCES

Abidi, N., Cabrales, L., & Hequet, E. (2009). Functionalization of a cotton fabric surface with titania nanosols: applications for self-cleaning and UV-protection properties. *ACS applied materials & interfaces, 1*(10), 2141-2146.

Acevedo-Peña, P., Lartundo-Rojas, L., & González, I. (2013). Effect of water and fluoride content on morphology and barrier layer properties of TiO_2 nanotubes grown in ethylene glycol-based electrolytes. *Journal of Solid State Electrochemistry, 17*(11), 2939-2947.

Arshadi, M. (2015). Manganese chloride nanoparticles: A practical adsorbent for the sequestration of Hg (II) ions from aqueous solution. *Chemical Engineering Journal, 259*, 170-182.

Asib, N., Afaah, A., Aadila, A., Mohamed, R., Alrokayan, S. A., Khan, H. A., & Khusaimi, Z. (2014). *Optical studies on the influence of annealing temperature of TiO_2 seed layer to the growth of ZnO nanostructures.* Paper presented at the Electrical, Electronics and System Engineering (ICEESE), 2014 International Conference on.

Baker, D. R., & Kamat, P. V. (2009). Disassembly, reassembly, and photoelectrochemistry of etched TiO_2 nanotubes. *The Journal of Physical Chemistry C, 113*(41), 17967-17972.

Brinker, C. J., & Scherer, G. W. (2013). *Sol-gel science: the physics and chemistry of sol-gel processing*: Academic press.

Byrne, H. E., & Mazyck, D. W. (2009). Removal of trace level aqueous mercury by adsorption and photocatalysis on silica–titania composites. *Journal of hazardous materials, 170*(2), 915-919.

Cao, C., Li, J., Wang, X., Song, X., & Sun, Z. (2011). Current characterization and growth mechanism of anodic titania nanotube arrays. *Journal of Materials Research, 26*(03), 437-442.

Chen, C.-C., & Hsieh, S.-J. (2010). Evaluation of Fluorine Ion Concentration in TiO_2 NT Anodization Process. *Journal of the Electrochemical Society, 157*(6), K125-K130.

Chen, X., & Mao, S. S. (2007). Titanium dioxide nanomaterials: synthesis, properties, modifications, and applications. *Chemical reviews, 107*(7), 2891-2959.

Cheng, X., Liu, H., Yu, X., Chen, Q., Li, J., Wang, P., & Wang, Q. (2013). Preparation of Highly Ordered TiO_2 Nanotube Array Photoelectrode for the Photoelectrocatalytic Degradation of Methyl Blue: Activity and Mechanism Study. *Science of Advanced Materials, 5*(11), 1563-1570.

Chiarle, S., Ratto, M., & Rovatti, M. (2000). Mercury removal from water by ion exchange resins adsorption. *Water research, 34*(11), 2971-2978.

Cipriano, A. F., Miller, C., & Liu, H. (2014). Anodic growth and biomedical applications of TiO_2 nanotubes. *Journal of Biomedical Nanotechnology, 10*(10), 2977-3003.

Clarkson, T. W. (2002). The three modern faces of mercury. *Environmental health perspectives, 110*(Suppl 1), 11.

Clarkson, T. W., & Magos, L. (2006). The toxicology of mercury and its chemical compounds. *CRC Critical Reviews in Toxicology, 36*(8), 609-662.

Crawford, G., & Chawla, N. (2009). Porous hierarchical TiO_2 nanostructures: Processing and microstructure relationships. *Acta Materialia, 57*(3), 854-867.

Dash, H. R., Mangwani, N., & Das, S. (2014). Characterization and potential application in mercury bioremediation of highly mercury-resistant marine bacterium Bacillus thuringiensis PW-05. *Environmental Science and Pollution Research, 21*(4), 2642-2653.

Deonarine, A., & Hsu-Kim, H. (2009). Precipitation of mercuric sulfide nanoparticles in NOM-containing water: Implications for the natural environment. *Environmental science & technology, 43*(7), 2368-2373.

Dou, B., & Chen, H. (2011). Removal of toxic mercury (II) from aquatic solutions by synthesized TiO_2 nanoparticles. *Desalination, 269*(1), 260-265.

Dou, B., Dupont, V., Pan, W., & Chen, B. (2011). Removal of aqueous toxic Hg (II) by synthesized TiO_2 nanoparticles and TiO_2/montmorillonite. *Chemical Engineering Journal, 166*(2), 631-638.

Ekino, S., Susa, M., Ninomiya, T., Imamura, K., & Kitamura, T. (2007). Minamata disease revisited: an update on the acute and chronic manifestations of methyl mercury poisoning. *Journal of the neurological sciences, 262*(1), 131-144.

Essa, A., Macaskie, L., & Brown, N. (2002). Mechanisms of mercury bioremediation. *Biochemical Society Transactions*(30), 672-674.

Fang, H., Gao, Y., Li, G., An, J., Wong, P.-K., Fu, H., & An, T. (2013). Advanced oxidation kinetics and mechanism of preservative propylparaben degradation in aqueous suspension of TiO_2 and risk assessment of its degradation products. *Environmental science & technology, 47*(6), 2704-2712.

Feng, X., Zhu, K., Frank, A. J., Grimes, C. A., & Mallouk, T. E. (2012). Rapid Charge Transport in Dye-Sensitized Solar Cells Made from Vertically Aligned Single-Crystal Rutile TiO_2 Nanowires. *Angewandte Chemie, 124*(11), 2781-2784.

Garbisu, C., & Alkorta, I. (2001). Phytoextraction: a cost-effective plant-based technology for the removal of metals from the environment. *Bioresource Technology, 77*(3), 229-236.

Ghasemi, Z., Seif, A., Ahmadi, T. S., Zargar, B., Rashidi, F., & Rouzbahani, G. M. (2012). Thermodynamic and kinetic studies for the adsorption of Hg (II) by nano-TiO_2 from aqueous solution. *Advanced Powder Technology, 23*(2), 148-156.

Gochfeld, M. (2003). Cases of mercury exposure, bioavailability, and absorption. *Ecotoxicology and environmental safety, 56*(1), 174-179.

Grätzel, M. (2001). Photoelectrochemical cells. *Nature, 414*(6861), 338-344.

Grimes, C. A. (2007). Synthesis and application of highly ordered arrays of TiO_2 nanotubes. *Journal of Materials Chemistry, 17*(15), 1451-1457.

Hanaor, D. A., & Sorrell, C. C. (2011). Review of the anatase to rutile phase transformation. *Journal of materials science, 46*(4), 855-874.

Hedgecock, I. M., Pirrone, N., Trunfio, G. A., & Sprovieri, F. (2006). Integrated mercury cycling, transport, and air-water exchange (MECAWEx) model. *Journal of Geophysical Research: Atmospheres (1984–2012), 111*(D20).

Hu, C., Zhou, J., He, S., Luo, Z., & Cen, K. (2009). Effect of chemical activation of an activated carbon using zinc chloride on elemental mercury adsorption. *Fuel Processing Technology, 90*(6), 812-817.

Hutchison, A. R., & Atwood, D. A. (2003). Mercury pollution and remediation: the chemist's response to a global crisis. *Journal of chemical crystallography, 33*(8), 631-645.

Hylander, L. D., & Goodsite, M. E. (2006). Environmental costs of mercury pollution. *Science of the Total Environment, 368*(1), 352-370.

Issaq, H., Atamna, I., Muschik, G., & Janini, G. (1991). The effect of electric field strength, buffer type and concentration on separation parameters in capillary zone electrophoresis. *Chromatographia, 32*(3-4), 155-161.

Jaishankar, M., Tseten, T., Anbalagan, N., Mathew, B. B., & Beeregowda, K. N. (2014). Toxicity, mechanism and health effects of some heavy metals. *Interdisciplinary Toxicology, 7*(2), 60-72.

Katebat, M., Suk Han, D., & Abdel-wahab, A. (2014). *Mercury Removal Using Titanium Dioxide Photocatalysis: Nanoparticle Versus Nanotube.* Paper presented at the Qatar Foundation Annual Research Conference.

Kim, D., Ghicov, A., Albu, S. P., & Schmuki, P. (2008). Bamboo-type TiO_2 nanotubes: improved conversion efficiency in dye-sensitized solar cells. *Journal of the American Chemical Society, 130*(49), 16454-16455.

Kim, I.-D., Rothschild, A., Lee, B. H., Kim, D. Y., Jo, S. M., & Tuller, H. L. (2006). Ultrasensitive chemiresistors based on electrospun TiO_2 nanofibers. *Nano letters, 6*(9), 2009-2013.

Krishnan, K. A., & Anirudhan, T. (2002). Removal of mercury (II) from aqueous solutions and chlor-alkali industry effluent by steam activated and sulphurised activated carbons prepared from bagasse pith: kinetics and equilibrium studies. *Journal of hazardous materials, 92*(2), 161-183.

Krýsa, J., Keppert, M., Waldner, G., & Jirkovský, J. (2005). Immobilized particulate TiO_2 photocatalysts for degradation of organic pollutants: Effect of layer thickness. *Electrochimica acta, 50*(25), 5255-5260.

Lai, C. W. (2014). Photocatalysis and Photoelectrochemical Properties of Tungsten Trioxide Nanostructured Films. *The Scientific World Journal, 2014*.

Lai, C. W., & Sreekantan, S. (2011). Effect of applied potential on the formation of self-organized TiO_2 nanotube arrays and its photoelectrochemical response. *Journal of Nanomaterials, 2011,* 11.

Lai, C. W., & Sreekantan, S. (2012). Optimized sputtering power to incorporate WO_3 into C–TiO_2 nanotubes for highly visible photoresponse performance. *Nano, 7*(06).

Lai, C. W., & Sreekantan, S. (2013a). Effect of heat treatment on WO_3-loaded TiO_2 nanotubes for hydrogen generation via enhanced water splitting. *Materials Science in Semiconductor Processing*.

Lai, C. W., & Sreekantan, S. (2013b). Incorporation of WO_3 species into TiO_2 nanotubes via wet impregnation and their water-splitting performance. *Electrochimica acta, 87,* 294-302.

Lai, C. W., & Sreekantan, S. (2013c). Single step formation of C-TiO_2 nanotubes: influence of applied voltage and their photocatalytic activity under solar illumination. *International Journal of Photoenergy, 2013*.

Lai, C. W., & Sreekantan, S. (2013d). Study of WO_3 incorporated C-TiO_2 nanotubes for efficient visible light driven water splitting performance. *Journal of alloys and compounds, 547,* 43-50.

Lee, J., & Choi, W. (2004). Effect of platinum deposits on TiO_2 on the anoxic photocatalytic degradation pathways of alkylamines in water: Dealkylation and N-alkylation. *Environmental science & technology, 38*(14), 4026-4033.

Lee, S., Cho, I.-S., Lee, J. H., Kim, D. H., Kim, D. W., Kim, J. Y., & Park, N.-G. (2010). Two-Step Sol− Gel Method-Based TiO_2 Nanoparticles with Uniform Morphology and Size for Efficient Photo-Energy Conversion Devices. *Chemistry of Materials, 22*(6), 1958-1965.

Leghari, S. A. K., Sajjad, S., Chen, F., & Zhang, J. (2011). WO_3/TiO_2 composite with morphology change via hydrothermal template-free route as an efficient visible light photocatalyst. *Chemical Engineering Journal, 166*(3), 906-915.

Lenzi, G., Fávero, C., Colpini, L., Bernabe, H., Baesso, M., Specchia, S., & Santos, O. (2011). Photocatalytic reduction of Hg (II) on TiO_2 and Ag/TiO_2 prepared by the sol–gel and impregnation methods. *Desalination, 270*(1), 241-247.

López-Muñoz, M., Aguado, J., Arencibia, A., & Pascual, R. (2011). Mercury removal from aqueous solutions of HgCl 2 by heterogeneous photocatalysis with TiO_2. *Applied Catalysis B: Environmental, 104*(3), 220-228.

Luttrell, T., Halpegamage, S., Tao, J., Kramer, A., Sutter, E., & Batzill, M. (2014). Why is anatase a better photocatalyst than rutile?-Model studies on epitaxial TiO_2 films. *Scientific reports, 4*.

Macak, J., Schmidt-Stein, F., & Schmuki, P. (2007). Efficient oxygen reduction on layers of ordered TiO_2 nanotubes loaded with Au nanoparticles. *Electrochemistry Communications, 9*(7), 1783-1787.

Macak, J. M., Zlamal, M., Krysa, J., & Schmuki, P. (2007). Self-Organized TiO_2 Nanotube Layers as Highly Efficient Photocatalysts. *Small, 3*(2), 300-304.

Macwan, D., Dave, P. N., & Chaturvedi, S. (2011). A review on nano-TiO_2 sol–gel type syntheses and its applications. *Journal of materials science, 46*(11), 3669-3686.

Magne, C., Moehl, T., Urien, M., Grätzel, M., & Pauporté, T. (2013). Effects of ZnO film growth route and nanostructure on electron transport and recombination in dye-sensitized solar cells. *Journal of Materials Chemistry A, 1*(6), 2079-2088.

Manohar, D., Krishnan, K. A., & Anirudhan, T. (2002). Removal of mercury (II) from aqueous solutions and chlor-alkali industry wastewater using 2-mercaptobenzimidazole-clay. *Water research, 36*(6), 1609-1619.

Matlock, M. M., Howerton, B. S., & Atwood, D. A. (2002). Chemical precipitation of heavy metals from acid mine drainage. *Water research, 36*(19), 4757-4764.

Merrifield, J. D., Davids, W. G., MacRae, J. D., & Amirbahman, A. (2004). Uptake of mercury by thiol-grafted chitosan gel beads. *Water research, 38*(13), 3132-3138.

Montazer, M., & Seifollahzadeh, S. (2011). Enhanced Self-cleaning, Antibacterial and UV Protection Properties of Nano TiO_2 Treated Textile through Enzymatic Pretreatment. *Photochemistry and photobiology, 87*(4), 877-883.

Mor, G. K., Carvalho, M. A., Varghese, O. K., Pishko, M. V., & Grimes, C. A. (2004). A room-temperature TiO_2-nanotube hydrogen sensor able to self-clean photoactively from environmental contamination. *Journal of Materials Research, 19*(02), 628-634.

Natarajan, T. S., Natarajan, K., Bajaj, H. C., & Tayade, R. J. (2013). Enhanced photocatalytic activity of bismuth-doped TiO_2 nanotubes under direct sunlight irradiation for degradation of Rhodamine B dye. *Journal of nanoparticle research, 15*(5), 1-18.

Nischk, M., Mazierski, P., Gazda, M., & Zaleska, A. (2014). Ordered TiO_2 nanotubes: the effect of preparation parameters on the photocatalytic activity in air purification process. *Applied Catalysis B: Environmental, 144*, 674-685.

Ohno, T., Sarukawa, K., Tokieda, K., & Matsumura, M. (2001). Morphology of a TiO_2 Photocatalyst (Degussa, P-25) Consisting of Anatase and Rutile Crystalline Phases. *Journal of Catalysis, 203*(1), 82-86.

Park, I. S., Woo, T. G., Lee, M. H., Ahn, S. G., Park, M. S., Bae, T. S., & Seol, K. W. (2006). Effects of anodizing voltage on the anodized and hydrothermally treated titanium surface. *Metals and Materials International, 12*(6), 505-511.

Park, N.-G., Van de Lagemaat, J., & Frank, A. (2000). Comparison of dye-sensitized rutile-and anatase-based TiO_2 solar cells. *The Journal of Physical Chemistry B, 104*(38), 8989-8994.

Park, S. E., Joo, H., & Kang, J. W. (2004). Effect of impurities in TiO_2 thin films on trichloroethylene conversion. *Solar Energy Materials and Solar Cells, 83*(1), 39-53.

Patra, M., & Sharma, A. (2000). Mercury toxicity in plants. *The Botanical Review, 66*(3), 379-422.

Paulus, W., Devi, P., & Mahmoud, M. E. (2011). Fabrication of titania nanotubes by a modified hydrothermal method. *Journal of Science and Technology, 2*(2).

Picquart, M., Castro-Garcia, S., Livage, J., Julien, C., & Haro-Poniatowski, E. (2000). Structural studies during gelation of WO_3 investigated by in-situ Raman spectroscopy. *Journal of Sol-Gel Science and Technology, 18*(3), 199-206.

Pirrone, N., Cinnirella, S., Feng, X., Finkelman, R., Friedli, H., Leaner, J., & Streets, D. (2010). Global mercury emissions to the atmosphere from anthropogenic and natural sources. *Atmospheric Chemistry and Physics*, *10*(13), 5951-5964.

Podkościelna, B., & Kołodyńska, D. (2013). A new type of cation-exchange polymeric microspheres with pendant methylenethiol groups. *Polymers for Advanced Technologies, 24*(10), 866-872.

Prakasam, H. E., Shankar, K., Paulose, M., Varghese, O. K., & Grimes, C. A. (2007). A new benchmark for TiO_2 nanotube array growth by anodization. *The Journal of Physical Chemistry C, 111*(20), 7235-7241.

Rafati-Rahimzadeh, M., Rafati-Rahimzadeh, M., Kazemi, S., & Moghadamnia, A. A. (2014). Current approaches of the management of mercury poisoning: need of the hour. *DARU Journal of Pharmaceutical Sciences, 22*(1), 46.

Rao, M. M., Reddy, D. K., Venkateswarlu, P., & Seshaiah, K. (2009). Removal of mercury from aqueous solutions using activated carbon prepared from agricultural by-product/waste. *Journal of Environmental Management, 90*(1), 634-643.

Regonini, D., Jaroenworaluck, A., Stevens, R., & Bowen, C. R. (2010). Effect of heat treatment on the properties and structure of TiO_2 nanotubes: phase composition and chemical composition. *Surface and interface analysis, 42*(3), 139-144.

Ridha, N. J., Jumali, M. H. H., Umar, A. A., & Alosfur, F. (2013). Defects-controlled ZnO nanorods with high aspect ratio for ethanol detection. *Int. J. Electrochem. Sci, 8*, 4583-4594.

Roy, P., Berger, S., & Schmuki, P. (2011). TiO_2 nanotubes: synthesis and applications. *Angewandte Chemie International Edition, 50*(13), 2904-2939.

Ruiz, O. N., Alvarez, D., Gonzalez-Ruiz, G., & Torres, C. (2011). Characterization of mercury bioremediation by transgenic bacteria expressing metallothionein and polyphosphate kinase. *BMC biotechnology, 11*(1), 82.

Sahoo, C., Gupta, A., & Pal, A. (2005). Photocatalytic degradation of Methyl Red dye in aqueous solutions under UV irradiation using Ag^+ doped TiO_2. *Desalination, 181*(1), 91-100.

Schmidt, M. (2007). *Thermochemical treatment of TiO_2 nanoparticles for photocatalytic applications.* University of South Florida.

Seo, M.-H., Yuasa, M., Kida, T., Huh, J.-S., Shimanoe, K., & Yamazoe, N. (2009). Gas sensing characteristics and porosity control of nanostructured films composed of TiO_2 nanotubes. *Sensors and Actuators B: Chemical, 137*(2), 513-520.

Shankar, K., Mor, G. K., Prakasam, H. E., Yoriya, S., Paulose, M., Varghese, O. K., & Grimes, C. A. (2007). Highly-ordered TiO_2 nanotube arrays up to 220 μm in length: use in water photoelectrolysis and dye-sensitized solar cells. *Nanotechnology, 18*(6), 065707.

Sikhwivhilu, L. M., Ray, S. S., & Coville, N. J. (2009). Influence of bases on hydrothermal synthesis of titanate nanostructures. *Applied Physics A, 94*(4), 963-973.

Sinha, A., & Khare, S. K. (2012). Mercury bioremediation by mercury accumulating Enterobacter sp. cells and its alginate immobilized application. *Biodegradation, 23*(1), 25-34.

Sinha, A., Pant, K. K., & Khare, S. K. (2012). Studies on mercury bioremediation by alginate immobilized mercury tolerant Bacillus cereus cells. *International Biodeterioration & Biodegradation, 71*, 1-8.

Skubal, L., & Meshkov, N. (2002). Reduction and removal of mercury from water using arginine-modified TiO_2. *Journal of Photochemistry and Photobiology A: Chemistry, 148*(1), 211-214.

Song, H. Y., Jiang, H. F., Liu, X. Q., Jiang, Y. Z., & Meng, G. Y. (2007). Preparation of WOx-TiO_2 and the Photocatalytic Activity under Visible Irradiation. *Key Engineering Materials, 336*, 1979-1982.

Song, Y. Y., Gao, Z. D., Wang, J. H., Xia, X. H., & Lynch, R. (2011). Multistage coloring electrochromic device based on TiO_2 nanotube arrays modified with WO_3 nanoparticles. *Advanced Functional Materials, 21*(10), 1941-1946.

Suriyawong, A., Smallwood, M., Li, Y., Zhuang, Y., & Biswas, P. (2009). Mercury capture by nano-structured titanium dioxide sorbent during coal combustion: lab-scale to pilot-scale studies. *Aerosol and Air Quality Research, 9*(4), 394-403.

Tan, Z., Sun, L., Xiang, J., Zeng, H., Liu, Z., Hu, S., & Qiu, J. (2012). Gas-phase elemental mercury removal by novel carbon-based sorbents. *Carbon, 50*(2), 362-371.

Tchounwou, P. B., Ayensu, W. K., Ninashvili, N., & Sutton, D. (2003). Review: Environmental exposure to mercury and its toxicopathologic implications for public health. *Environmental Toxicology, 18*(3), 149-175.

Tian, W.-C., Ho, Y.-H., Chen, C.-H., & Kuo, C.-Y. (2013). Sensing performance of precisely ordered TiO_2 nanowire gas sensors fabricated by electron-beam lithography. *Sensors, 13*(1), 865-874.

Tsai, C.-Y., Kuo, T.-H., & Hsi, H.-C. (2012). Fabrication of Al-Doped TiO_2 Visible-Light Photocatalyst for Low-Concentration Mercury Removal. *International Journal of Photoenergy, 2012*.

UNEP, T. (2013). Global Mercury Assessment 2013: Sources, Emissions, Releases and Environmental Transport: UNEP Chemicals Branch Geneva, Switzerland.

Varghese, O. K., Gong, D., Paulose, M., Ong, K. G., & Grimes, C. A. (2003). Hydrogen sensing using titania nanotubes. *Sensors and Actuators B: Chemical, 93*(1), 338-344.

Veiga, M. M., Maxson, P. A., & Hylander, L. D. (2006). Origin and consumption of mercury in small-scale gold mining. *Journal of Cleaner Production, 14*(3), 436-447.

Vuong, N. M., Kim, D., & Kim, H. (2013). Electrochromic properties of porous WO_3–TiO_2 core–shell nanowires. *Journal of Materials Chemistry C, 1*(21), 3399-3407.

Wagner-Döbler, I., Von Canstein, H., Li, Y., Timmis, K. N., & Deckwer, W.-D. (2000). Removal of mercury from chemical wastewater by microoganisms in technical scale. *Environmental science & technology, 34*(21), 4628-4634.

Wahyuni, E. T., Kunarti, E. S., & Sugiharto, E. Performance of TiO_2 Nanoparticle Prepared on Lignin Structure as Photocatalyst for Hazardous Mercury Removal Through Photoreduction Mechanism.

Wang, J., Han, Y., Feng, M., Chen, J., Li, X., & Zhang, S. (2011). Preparation and photoelectrochemical characterization of WO_3/TiO_2 nanotube array electrode. *Journal of materials science, 46*(2), 416-421.

Wang, J., Zheng, S., Shao, Y., Liu, J., Xu, Z., & Zhu, D. (2010). Amino-functionalized Fe_3O_4@ SiO_2 core–shell magnetic nanomaterial as a novel adsorbent for aqueous heavy metals removal. *Journal of colloid and interface science, 349*(1), 293.

Wang, X., Yolcubal, I., Wang, W., Artiola, J., Maier, R., & Brusseau, M. (2004). Use of cyclodextrin and calcium chloride for enhanced removal of mercury from soil. *Environmental toxicology and chemistry, 23*(8), 1888-1892.

Wei, P., Liu, J., & Li, Z. (2013). Effect of Pt loading and calcination temperature on the photocatalytic hydrogen production activity of TiO_2 microspheres. *Ceramics International, 39*(5), 5387-5391.

Wilhelm, S. M., & Kirchgessner, D. (2001). *Mercury in Petroleum and Natural Gas--estimation of Emissions from Production, Processing, and Combustion*: United States Environmental Protection Agency, National Risk Management Research Laboratory.

Xin, Y., Liu, H., Liu, Y., Ma, D., & Chen, Q. (2013). Composition and photoelectrochemical properties of WO_3/TNAs photoelectrodes fabricated by in situ electrochemical method. *Electrochimica acta, 104*, 308-313.

Yu, C., Jimmy, C. Y., Zhou, W., & Yang, K. (2010). WO_3 coupled P-TiO_2 photocatalysts with mesoporous structure. *Catalysis letters*, *140*(3-4), 172-183.

Zahir, F., Rizwi, S. J., Haq, S. K., & Khan, R. H. (2005). Low dose mercury toxicity and human health. *Environmental toxicology and pharmacology, 20*(2), 351-360.

Zornoza, P., Millán, R., Sierra, M. J., Seco, A., & Esteban, E. (2010). Efficiency of white lupin in the removal of mercury from contaminated soils: Soil and hydroponic experiments. *Journal of Environmental Sciences, 22*(3), 421-427.

LIST OF PUBLICATIONS AND PAPERS PRESENTED

ISI-Cited Publications:

1. **Wai Hong Lee**, Chin Wei Lai, You Sing Lim, Sharifah Bee Abd Hamid (2014). One-dimensional TiO_2 nanotubes arrays: Influence of anodization voltage and Their Photocatalytic Activity Performance. *Materials Research Innovations*, 18(S6), S6-474-S6-476.

2. **Wai Hong Lee**, Chin Wei Lai, Sharifah Bee Abd Hamid (2015). One-Step Formation of WO_3-Loaded TiO_2 Nanotubes Composite Film for High Photocatalytic Performance. *Materials*, 8, 2139-2153.

3. Chin Wei Lai, Sharifah Bee Abd Hamid, Tong Ling Tan, **Wai Hong Lee** (2015). Rapid Formation of 1-D Titanate Nanotubes using Alkaline Hydrothermal Treatment and its Photocatalytic Performance. *Journal of Nanomaterials*, 2015, Article ID: 145360.

4. **Wai Hong Lee**, Chin Wei Lai, Sharifah Bee Abd Hamid (2015). In situ Anodization of WO_3-Decorated TiO_2 Nanotube Arrays for Efficient Mercury Removal. *Materials*, 8, 5702-5714.

Conference Proceedings:

1. **Wai Hong Lee**, Chin Wei Lai, You Sing Lim, Sharifah Bee Abd Hamid (2013). One-dimensional TiO_2 nanotubes arrays: Influence of anodization voltage and Their Photocatalytic Activity Performance. *Proceeding of 1st International Conference on the Science & Engineering of Materials*, 13-14th November 2013, Sunway Putra Hotel, Kuala Lumpur, Malaysia.

2. **Wai Hong Lee**, Chin Wei Lai, Sharifah Bee Abd Hamid (2014). Influence of Fluoride Ion Content on the Growth of Anodic WO_3-TiO_2 Nanotubes Film. *Proceeding of 6th International Conference on Postgraduate Education 2014 (ICPE-6)*, 17-18th December 2014, Main Hall, Universiti Teknikal Malaysia (UTEM), Melaka, Malaysia.